ABSTRACT

Title of dissertation: BIO-INSPIRED INFORMATION
                           EXTRACTION IN 3-D ENVIRONMENTS
                           USING WIDE-FIELD INTEGRATION
                           OF OPTIC FLOW

                           Andrew Maxwell Hyslop,
                           Doctor of Philosophy, 2010

Dissertation directed by: Assistant Professor J. Sean Humbert
                           Department of Aerospace Engineering

A control theoretic framework is introduced to analyze an information extraction approach from patterns of optic flow based on analogues to wide-field motion-sensitive interneurons in the insect visuomotor system. An algebraic model of optic flow is developed, based on a parameterization of simple 3-D environments. It is shown that estimates of proximity and speed, relative to these environments, can be extracted using weighted summations of the instantaneous patterns of optic flow. Small perturbation techniques are utilized to link weighting patterns to outputs, which are applied as feedback to facilitate stability augmentation and perform local obstacle avoidance and terrain following. Weighting patterns that provide direct linear mappings between the sensor array and actuator commands can be derived by casting the problem as a combined static state estimation and linear feedback control problem. Additive noise and environment uncertainties are incorporated into an offline procedure for determination of optimal weighting patterns.

Several applications of the method are provided, with differing spatial measurement domains. Non-linear stability analysis and experimental demonstration is presented for a wheeled robot measuring optic flow in a planar ring. Local stability analysis and simulation is used to show robustness over a range of urban-like environments for a fixed-wing UAV measuring in orthogonal rings and a micro helicopter measuring over the full spherical viewing arena. Finally, the framework is used to analyze insect tangential cells with respect to the information they encode and to demonstrate how cell outputs can be appropriately amplified and combined to generate motor commands to achieve reflexive navigation behavior.

BIO-INSPIRED INFORMATION EXTRACTION IN 3-D ENVIRONMENTS USING WIDE-FIELD INTEGRATION OF OPTIC FLOW

by

Andrew Maxwell Hyslop

Dissertation submitted to the Faculty of the Graduate School of the
University of Maryland, College Park in partial fulfillment
of the requirements for the degree of
Doctor of Philosophy
2010

Advisory Committee:
Assistant Professor J. Sean Humbert, Chair/Advisor
Professor Rama Chellappa
Associate Professor Robert M. Sanner
Associate Professor David Akin
Professor Inderjit Chopra

Acknowledgments

Insects are pretty dumb, but I still required 7.5 years of tertiary education to make a tiny contribution to the exciting new field of transitioning their 'simple-minded' architecture to 'intelligent' man-made robots. Perhaps the day will arrive when Skynet becomes self-aware and dooms us all, but we are certaintly not there yet.

First and foremost, I want to thank my advisor, Dr. Sean Humbert, for providing me with a challenging and inspiring topic, completely outside the realm of my previous experience. Sean invests himself in his students with great enthusiasm and is always full of ideas and new research directions. I would not have been able to complete my PhD in such a short period without his flexibility, understanding and yet firm management style. Thanks also to my lab mates for all their help; Mike and Scott for the ground robot, David and Brian for AVLSim, Imraan for his insect dynamics sys ID, and Joe, Greg and Badri for the quadrotor. Joe, your enthusiasm for the Thirsty Turtle is undying, and I respect that; Greg, your Australian accent still needs a lot of work; and Badri, you are an enigma. The Thirsty Turtle deserves a shout out of their own, for their $1 beer pricing structure and for the mini-skirts that just keep getting shorter.

Thanks to Mrs Fox of Gray St Primary for telling us that if we didn't learn our times tables we'd end up as check-out chicks at Safeway. My education also owes thanks to space tether gurus Michiel Kruijff and Erik van der Heide, my undergrad advisor Dr. Chris Blanksby, Ray 'math is cool' Peck, math-teacher-comedian Julian

Table of Contents

List of Tables

List of Figures

Nomenclature

A	state space dynamics matrix		x	forward offset, m
a	lateral obstacle clearance, m		Y	spherical harmonic function
B	control coefficients matrix		$\mathbf{y}$	WFI outputs, rad/s
$\mathcal{B}$	body frame		y	lateral offset, m
C	observation matrix		z	vertical offset, m
$\mathcal{C}$	camera frame		α	field of view, rad
C	correlation matrix		β	body-referred elevation angle, rad
c	cosine function		γ	body-referred azimuth angle, rad
$C^{\dagger}$	observation inversion matrix		δ	perturbation
d	distance, m		δ_a =	aileron deflection from trim, rad
$\mathbf{F}$	weighting pattern		δ_e =	elevator deflection from trim, rad
$\mathcal{F}$	inertial fixed frame		δ_r =	rudder deflection from trim, rad
F	Fisher information matrix		δ_T =	thrust offset from trim, N
g	front/rear obstacle clearance, m		ε	weighting of model uncertainty term
h	vertical obstacle clearance, m		$\boldsymbol{\eta}$	optic flow measurement noise vector
J	LQR performance index		θ	pitch angle, rad
K	gain matrix		μ	nearness function, 1/m
$\mathcal{K}$	number of measurement points		Λ	normalized actuator input
$\mathcal{L}$	local frame on sphere surface		ξ	lateral flapping angle, rad
M	number of outputs		Φ	Legendre function
N	normalization coefficient		ϕ	roll angle, rad
n	number of states		χ	longitudinal flapping angle, rad
P	state estimate covariance matrix		ψ	heading angle, rad
$\mathcal{P}$	number of actuators		Ω	solid angle, sr
p	roll rate, rad/s		$\boldsymbol{\omega}$	angular rate vector, rad/s
$\dot{\mathbf{Q}}$	optic flow, rad/s			
$\mathbf{q}$	vehicle pose		*Additional Subscripts/Superscripts*	
q	pitch rate, rad/s		a_m	order m sine harmonic
R	noise covariance matrix		b	body frame
$\mathcal{R}$	rotation matrix		b_m	order m cosine harmonic
$\mathbf{r}$	point on imaging surface		c	camera frame
r	yaw rate, rad/s		D	inertial down direction
s	sine function		E	inertial East
$\mathcal{T}$	kinematic transform matrix		H	horizontal
$\mathbf{u}$	control vector (trim perturbation)		L	left brain hemisphere
u	forward velocity, m/s		l	harmonic degree
$\mathbf{v}$	velocity vector, m/s		lat	lateral
v	modal vector		lin	linearized
v	lateral velocity, m/s		lon	longitudinal
W	output weighting matrix		m	harmonic order
$\mathbf{w}$	WFI measurement noise vector		mr	main rotor
w	vertical velocity, m/s		N	inertial North
$\mathbf{x}$	vehicle state vector		nl =	nonlinear

P	=	pitch plane	FPS		Frames Per Second
R	=	roll plane	FOV		Field Of View
R		right brain hemisphere	GPS		Global Positioning System
ref		reference/target trajectory	HS		Horizontal System
S		inertial South	IMU		Inertial Measurement Unit
t		thrust	LS		Least Squares Estimator
U		inertial up direction	LQR		Linear Quadratic Regulator
V		vertical	MAOS		Multiaperture Optical System
W		inertial West	MAV		Micro Air Vehicle
Y	=	yaw plane	MV		Minimum Variance Estimator
~		measured quantity	TC		Tangential Cell
ˆ		estimated quantity	UAV		Uninhabited Air Vehicle
0		nominal	VLSI		Very-Large-Scale Integration
			VS		Vertical System
Abbreviations			WFI		Wide-Field Integration
DOF		Degrees Of Freedom			
EMD		Elementary Motion Detector			

Chapter 1

Introduction

Current uninhabited air vehicles (UAVs) are equipped with sensors that enable the platform to maintain stable flight, track a desired flight trajectory, and perform strategic-level waypoint navigation via GPS (yellow trajectory in Fig. 1.1). However, they do not permit operation around local unmapped obstacles, such as trees and buildings inside a city. Whilst some candidate technologies exist to potentially perform this task, they do not scale down to the stringent payload requirements of micro air vehicles (MAVs), a physically miniature subclass of UAVs. It is the aim of this thesis to help bridge the gap between the the available sensor technologies and the type of missions and navigational capabilities desired for the MAVs. Specifically, the intent is to leverage sensing concepts from the insect visuomotor system to provide the proximity and velocity information required for tactical level navigation (red trajectory in Fig. 1.1).

Interest in micro air vehicle (MAV) platforms has expanded significantly in recent years, primarily due to the requirement for inexpensive surveillance and reconnaissance in potentially inaccessible or dangerous areas. To be truly effective, these platforms will need to be endowed with the capability to operate autonomously in unmapped obstacle-rich environments. Whilst significant investment and progress has been made in the areas of actuation and fabrication technology for micro-scale
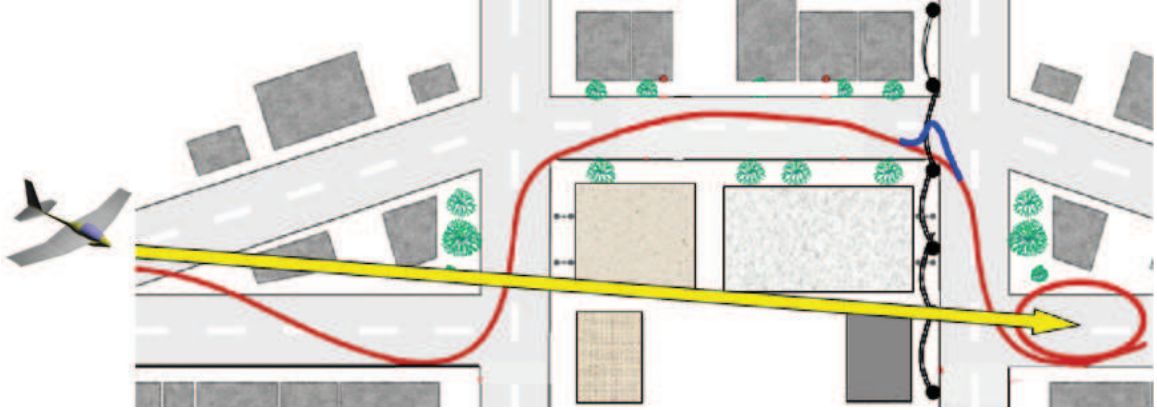
Figure 1.1: Autonomous Guidance, hierarchical breakdown. Yellow - strategic high-level mission goal direction, Red - tactical maneuvering through clutter to target, Blue - reactive obstacle avoidance maneuver that preempts urban or cluttered maneuvering

systems [4, 5, 6, 7], sensors, processing, and feedback control architectures are dramatically behind the curve at these scales.

The fast dynamics of these MAVs call for high bandwidth sensors, and the payload limitations dictate a sensor suite on the order of 1 g, consuming less than 1 mW of power. Existing guidance systems consistent with small payloads (Fig. 1.2) are low bandwidth (5 Hz), weigh on the order of 15-30 g, require 0.75-1 W of power, and do not function indoors due to GPS availability. Miniature laser rangefinders [8] and ultrasonics have the required bandwidth, however implementations are also on the order of 25-40 g, require 400 mW, and have a very limited field of view (FOV). Traditional machine vision approaches [9, 10, 11, 12, 13, 14, 15, 16] that infer proximity and velocity information from camera imagery have been demonstrated, however these algorithms are computationally expensive and require off-board visual processing, even on vehicles with significant payloads [17]. For an aerial microsystem with a requirement of both indoor and outdoor operation, there are currently no

Sensor	Weight (g)	Bandwidth (Hz)	Power (mW)
GPS/IMU (Position, Velocity, Angular Vel, Attitude)	16-28	4 (GPS) 180 (IMU)	770-910
IMU (Attitude, Ang Vel, Mag, Accel)	3	200	250
Laser Rangefinder (distance)	26	250	400
Ultrasonics (distance)	10	20	1000
Analog VLSI Optic Flow Sensor	0.25	500-1000	0.01
Target Payload	1	20-50	100

Figure 1.2: Current micro-size sensor technology.

viable approaches to achieve the required velocity estimation, obstacle localization and avoidance [18, 19]. Hence, novel sensors and sensory processing architectures will need to be explored if autonomous microsystems are to be ultimately successful.

For inspiration, researchers are looking to the millions of examples of flying insects that have developed elegant solutions to the challenges of visual perception and navigation [20]. Insects rely on optic flow [21, 22], the characteristic patterns of visual motion that form on their retinas as they move. These time dependent motion patterns are a rich source of visual cues that are a function of the relative speed and proximity of the insect with respect to objects in the surrounding environment [23]. The insect's visuomotor system performs computations in a very small volume, and manages the rapid convergence of signals from thousands of noisy motion detectors to a small number of muscle commands. The robust flight behaviors that result [24, 25, 26, 27] align well with the capabilities desired for MAVs. To effectively leverage this concept, the relevant information processing techniques must be formalized and linked, via feedback, to the navigational heuristics observed by behavioral biologists.
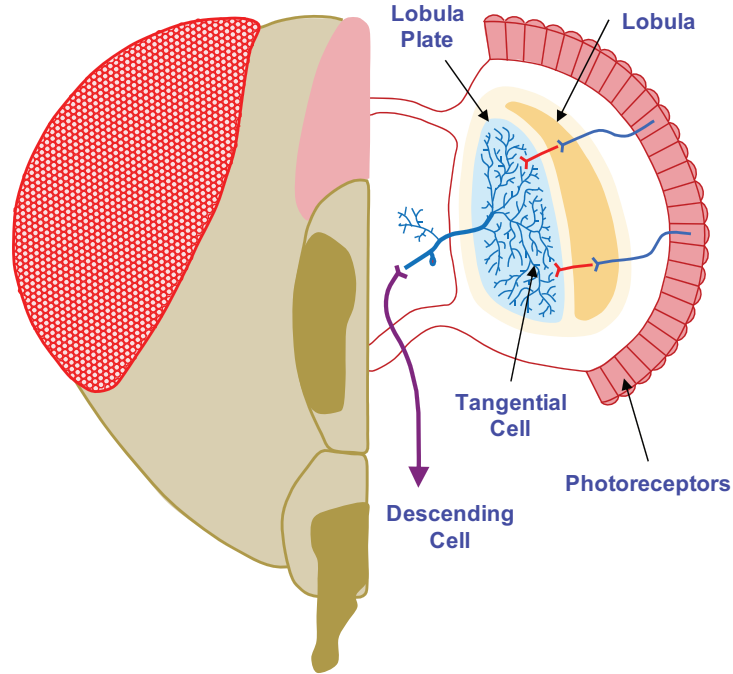
Figure 1.3: Visuomotor system structure. Local motion of luminance patterns is processed by EMDs (not shown) and communicated to the third visual ganglion, where wide-field integrating neurons extract information for control and navigation.

Therefore, the central aim of this thesis is to formulate the fundamental estimation and control principles for transition of this biologically-inspired architecture to 6-DOF engineered systems.

1.1   Visuomotor Feedback in Insects

The insect retina, composed of thousands of individual sub-units, functions to image the incident patterns of luminance from the environment. As an insect moves, the intensity of the image formed at each lens becomes time dependent. The rate and direction of the local image shifts, taken over the entire field of view, form patterns of optic flow. The spatial structure of the patterns of optic flow that the insect experiences is governed primarily by the insect's relative motion and

proximity to objects through motion parallax, a relationship that can be expressed mathematically in closed form [28]. Extraction of visual information contained in optic flow is performed by wide-field sensitive *tangential cells*, which communicate their output through descending neurons to the flight motor to execute changes in wing kinematics [21, 22].

The tangential cells are large, motion-sensitive neurons that reside in the lobula plate portion of the third visual ganglia (Fig. 1.3). They are believed to integrate (pool) the outputs of large numbers of retinotopically distributed elementary motion detectors (EMDs) [29, 30, 2, 21, 22]. Prominent among the tangential cells are the identified neurons that comprise the 'horizontal system' (HS) and 'vertical system' (VS) found in a number of species of flies [31, 32, 33]. As their names suggest, these neurons are sensitive primarily to horizontal and vertical patterns of optic flow, respectively. They respond with graded membrane potentials whose polarity depends on the direction of motion. Their spatial sensitivity to local motion cues has in some cases been mapped out [2], as shown for several cells in Figs. 5.1 and 5.2, and the resemblance of some of these maps to the patterns of optic flow induced by particular modes of egomotion has led to the hypothesis that the corresponding neurons may act as matched filters for these patterns [34, 35]. However, recent work has shown that translational motion cues, which are the source of proximity information, are also present in the outputs of cells that were previously thought to be used only for compensation of rotary motion [36]. This suggests that cell patterns might be structured to extract a combination of relative speed and proximity cues, rather than direct estimates of the velocity state. Hence, while some progress

has been made in understanding structure, arrangement, and synaptic connectivity [21], the exact functional role that the tangential cells hold in the stabilization and navigation system of the fly remains a challenging and open question.

1.2   Optic-flow-based Navigation in Robotics

The idea that insects use optic flow to navigate has inspired a number of studies in the robotics field. This section describes research in closed-loop optic-flow-based navigation and egomotion estimation, and introduces the concept of wide-field integration (WFI), a technique based on the visuomotor principles discussed in Section 1.1.

In most studies that attempt closed-loop obstacle avoidance using optic flow, a feedback signal is generated by comparing single points or uniformly averaged patches of optic flow on the sides or the bottom of a vehicle to generate a control input. Navigational goals included obstacle navigation [37, 38, 39, 40, 41, 42, 43, 44, 45, 46], speed control [47, 48, 49, 50] and terrain following [51, 52, 53]. These efforts provide a path forward, but they generally ignore (in favor of more traditional architectures) the fundamental processing and feedback mechanisms that insects employ to extract information from optic flow and to regulate behavior. Some studies required independent sensing of vehicle rotation rates or nulling of the sensor during rotation maneuvers, and results are predominately presented without formal closed loop stability analysis.

In more academic approaches, algorithms have been applied to generate estimates of egomotion and/or the structure of objects in the surrounding environment

based on optic flow measurements. Past research typically involves fitting a theoretical model of optic flow to measurements at a series of points in a camera image by numerical solution of the least squares problem [54, 55, 56, 57]. With the assumption of forward-dominated motion, it is possible to resolve the direction of a vehicle's velocity vector, its rotation rates and a 3-D depth map [58]. Fast Fourier Transforms can be employed to speed up computations, but the process still requires ~ 1 s on a Pentium processor. One can also simplify the problem by using an initial estimate of egomotion (from IMU/GPS) to extract terrain shape [59] and then, at the next update, extract egomotion using the terrain shape estimate [54, 60] and so on. Noise reduction is often achieved by only measuring optic flow at high contrast image points, which provides more accurate estimates but requires a feature detection step [61, 55, 62, 60]. To further smooth estimates, the dynamics of the vehicle can be incorporated by using extended Kalman filters, with the nonlinear optic flow equations forming the measurement model [63, 62, 10] and with optional fusing of IMU data [64]. Whilst these algorithms may be feasible for implementation on a UAV with a powerful micro-processor, they do not align with the computational constraints of MAVs. Furthermore, the above studies do not address the obstacle avoidance task and often require an accurate model of the vehicle or environment [54, 55, 60].

The potential of the insect visuomotor architecture to provide egomotion estimation at low computation cost was first explored in detail by Franz and Krapp [35]. In this study, a linear algorithm was derived, based on the idea that tangential cells integrate the measured motion field against a pre-stored weighting pattern. By

7

selecting weightings that match the apparent motion induced by particular modes of egomotion, one can filter the measured optic flow field to extract quantities of interest. However, the matched filters required a post-processing stage and there was no attempt to extract proximity cues or close the navigation loop. These shortcomings were addressed by Humbert et al. [65, 66, 67, 68], who developed a mathematical framework to analyze the insect's approach, termed Wide-Field Integration [68]. The concept is based on static feedback which generates compensatory commands to hold simple patterns of optic flow fixed on an imaging surface, such as the typical sine wave pattern induced on a circular sensor by forward motion in a corridor. Weighted summations of optic flow measurements are used to detect spatial imbalances, shifts, and magnitude changes which have interpretations of relative proximity and speed with respect to obstacles. An example of this approach has been observed in the landing behavior of honeybees; a simple feedback loop which holds the ratio of forward speed to height constant while descending toward a surface guarantees an exponentially decaying approach trajectory [69], without the knowledge of absolute speed or distance. Complicated patterns of optic flow can therefore be rapidly decomposed into compensatory motor commands that maneuver the vehicle safely between obstacles.

The primary advantage of WFI is computational simplicity; it does not require direct vehicle state estimation, visual feature detection, extraction, or classification. Useful information for stability augmentation and navigation is obtained by analogues to tangential cell processing, i.e., computing a handful of inner products of optic flow. This is a very efficient process that is extremely robust to noise, and

does not require high resolution visual imagery. It has been recently demonstrated that this approach can be implemented real time in analog VLSI at high bandwidth (5 KHz) using basic Reichardt-type elementary motion detectors (EMDs) for optic flow estimation and a programmable current matrix for computing inner products [70]. These sensors consume power on the order of microwatts, and can be packaged on the order of milligrams. Therefore, WFI offers orders of magnitude improvement in bandwidth, power consumption, and payload weight over implementations of traditional methodologies described above, which are constrained to operate on digital processors.

In summary, the motivation for the research is to develop sensing concepts that will allow MAVs to obtain the proximity and velocity information they need to operate around local unmapped obstacles. Active sensing technologies do not fit the MAVs payload constraints, therefore researchers are looking to passive techniques, such as vision. Unfortunately, state-of-the-art vision algorithms to compute egomotion and/or obstacle maps are too computationally intensive for an MAV micro processor. However, optic flow sensing, combined with wide-field integration (inspired by the insect visuomotor system) to extract navigational quantities, can be implemented on analog VLSI chips, providing a feasible solution. The primary research gap which this thesis seeks to fill is the lack of a robust formal method for designing WFI weighting patterns, which map data from a spatially distributed sensor array to actuator commands that stabilize the vehicle and allow navigation of obstacles.

1.3 Thesis Contributions and Organization

Though the tangential cell analogue (WFI) is well defined and has been simulated for simple planar platforms using 1-D optic flow measurements [65, 66, 67], maturation of the concept requires development in several areas. In this thesis, experimental demonstrations are performed and previous stability analysis is expanded to include non-linear dynamics and measurements. WFI theory is extended to 2-D optic flow measurements in order to control 6-DOF vehicles in 3-D environments. Robustness aspects are addressed by examining stability in the face of an uncertain environment structure and by incorporating this uncertainty and measurement noise properties in the design of optimal WFI weighting patterns. Finally, a control theoretic framework is used to analyze the weighting patterns ingrained in insect tangential cells with respect to the information they encode, and to show how they can be used to achieve the impressive closed-loop behaviors observed by biologists.

Chapter 2 introduces an optic flow model and a tangential cell analogue, which is used to extract navigationally relevant information from spatial patterns of the optic flow. It is further shown how the choice of WFI weighting pattern links to information content. Chapter 3 addresses feedback design and describes how the problem of selecting an optimal weighting pattern can be cast as a combined static state estimation and linear feedback control problem. The derived methodology is applied to robotic platforms in Chapter 4, with experimental demonstrations and simulations, and is used to analyze insect tangential cells in Chapter 5. Chapter 6 summarizes the WFI algorithm and provides a step-by-step method for real-time

implementation. Conclusions, limitations and areas for future work are discussed in

Chapter 7.

Chapter 2

Wide-Field Integration of Optic Flow

This chapter seeks to mathematically formalize the concept of WFI (the information extraction technique derived from the insect visuomotor system) in 3-D environments. Previous efforts have either been limited to simplified planar environments or have applied WFI without supporting analysis.

The central idea is that if one can model how navigationally relevant information is encoded in patterns of optic flow, then one can design appropriate WFI weighting patterns to decode the measurements. To achieve this goal, an inner product model for tangential cell analogues is presented and a framework is introduced to characterize the information that can be extracted from patterns of optic flow on various measurement domains. An algebraic model of optic flow is developed by parameterizing a family of typical 3-D environments. Offline WFI with the optic flow model, combined with small perturbation techniques, provides linkages between measurement weighting patterns and WFI outputs, which are functions of relative proximity and velocity with respect to the parameterized environments.

2.1 Optic Flow Model

2.1.1 What is Optic Flow?

Optic flow is the apparent visual motion that one experiences when they move through an environment. It can be thought of as the local rate and direction of movement in an image. It is typically computed by comparing two successive frames from a camera image sequence (e.g., Fig. 2.1) and applying an optic flow estimation algorithm.

2.1.2 How is it Modeled?

The (true) optic flow is the vector field of relative velocities of material points in the environment projected into the tangent space of the imaging surface (e.g., Fig. 2.2). It is a combination of the observer's rotational and translational motion, along with the relative proximity to surrounding objects. For a given angular velocity $\boldsymbol{\omega}$ and translational velocity $\mathbf{v}$ of the vantage point, along with the nearness function μ which represents the distribution of objects in the surrounding environment, the optic flow pattern $\dot{\mathbf{Q}}$ on a spherical imaging surface S^2 for an arbitrary distribution of obstacles can be expressed [28] as

$$\dot{\mathbf{Q}} = -\boldsymbol{\omega} \times \mathbf{r} - \mu \left[\mathbf{v} - \langle \mathbf{v}, \mathbf{r} \rangle \mathbf{r} \right]. \tag{2.1}$$

The quantity $\dot{\mathbf{Q}} = \dot{Q}^\gamma \, \hat{\mathbf{e}}_\gamma + \dot{Q}^\beta \, \hat{\mathbf{e}}_\beta$ has components in the azimuth $\gamma \in (0, 2\pi)$ and elevation $\beta \in (0, \pi)$ directions (Fig. 2.2A), and lives in the vector-valued space of

Frame 1
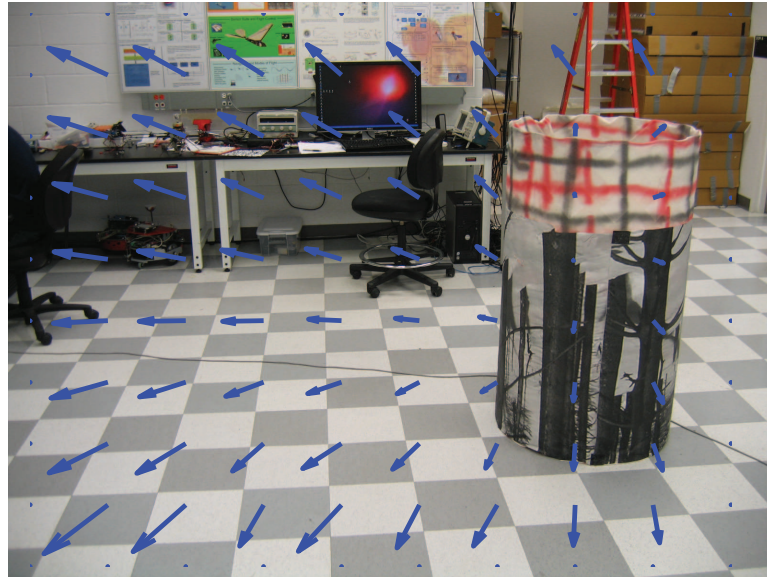
Frame 2

Figure 2.1: Optic flow vector field superimposed on camera image. Each optic flow vector denotes the local movement in the image between Frame 1 and Frame 2.

square integrable functions on the sphere

$$L^2(S^2, \mathbb{R}^2) = \left\{ \mathbf{f} = \begin{pmatrix} f_1(\mathbf{r}) \\ f_2(\mathbf{r}) \end{pmatrix} : \mathbf{r} \in S^2, f_k(\mathbf{r}) \in L^2(S^2), k = 1, 2 \right\}. \quad (2.2)$$

The nearness μ is equal to $1/d(\gamma, \beta, \mathbf{q})$, where $d \in (0, \infty)$ is the distance from the imaging surface to the nearest object in the environment along the direction $\hat{\mathbf{e}}_r$ (Fig. 2.3C) through a point on the imaging surface $\mathbf{r}(\gamma, \beta)$. If one expresses the velocity $\mathbf{v} = (u, v, w)$ and angular velocity $\boldsymbol{\omega} = (p, q, r)$ in coordinates of the body frame $\mathcal{B} = \{\hat{\mathbf{e}}_{x_b}, \hat{\mathbf{e}}_{y_b}, \hat{\mathbf{e}}_{z_b}\}$, the expressions for the azimuthal and elevation components of optic flow are given by

$$\dot{Q}^\gamma = p \cos \beta \cos \gamma + q \cos \beta \sin \gamma - r \sin \beta + \mu(u \sin \gamma - v \cos \gamma)$$

$$\dot{Q}^\beta = p \sin \gamma - q \cos \gamma + \mu(-u \cos \beta \cos \gamma - v \cos \beta \sin \gamma + w \sin \beta). \quad (2.3)$$

The complete surface of the sphere represents the maximum measurement domain possible, but navigational quantities of interest can also be decoded from optic flow sampled over much smaller domains. One such example, that simplifies (2.3), comprises measurement of tangential and normal (off-axis) components of optic flow in three orthogonal and concentric circular rings (Fig. 2.2B) aligned, for convenience, with the body-fixed axes of the 6-DOF vehicle, i.e., the roll plane R ($\gamma = \pi/2$), pitch plane P ($\gamma = 0$), and yaw plane Y ($\beta = \pi/2$). In this case, (2.3)

15
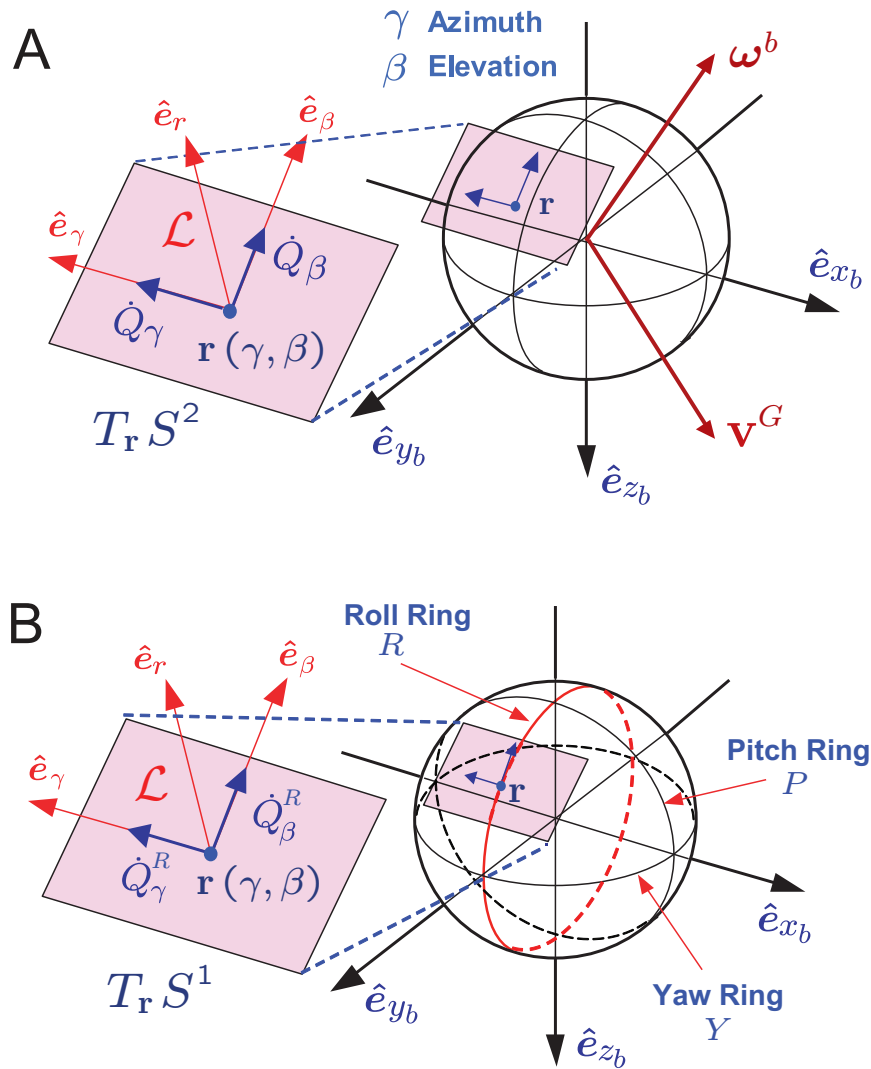
Figure 2.2: Geometry of imaging surface. Optic flow is the projected relative velocities of objects in the environment into the tangent space $T_{\mathbf{r}}$ of the imaging surface - e.g., (A) a sphere S^2 or (B) circular S^1 rings.

simplifies to the ring-specific equations

$$\text{Roll } (R)$$

$$\dot{Q}_R^\beta \;=\; p + \mu_R(-v\cos\beta + w\sin\beta)$$

$$\dot{Q}_R^\gamma \;=\; q\cos\beta - r\sin\beta + \mu_R u$$

$$\text{Pitch } (P)$$

$$\dot{Q}_P^\beta \;=\; -q + \mu_P(-u\cos\beta + w\sin\beta)$$

$$\dot{Q}_P^\gamma \;=\; p\cos\beta - r\sin\beta - \mu_P v \qquad\qquad (2.4)$$

$$\text{Yaw } (Y)$$

$$\dot{Q}_Y^\beta \;=\; p\sin\gamma - q\cos\gamma + \mu_Y w$$

$$\dot{Q}_Y^\gamma \;=\; -r + \mu_Y(u\sin\gamma - v\cos\gamma),$$

where $\beta \in (0, 2\pi)$ and μ_k represents the nearness function constrained to plane k. The ring-constrained optic flow lives in the vector-valued space of square integrable functions on the circle

$$L^2(S^1, \mathbb{R}^2) \;=\; \left\{ \mathbf{f} = \begin{pmatrix} f_1(\mathbf{r}) \\ f_2(\mathbf{r}) \end{pmatrix} : \mathbf{r} \in S^1,\, f_k(\mathbf{r}) \in L^2(S^1),\, k = 1, 2 \right\}. \qquad (2.5)$$

2.2 Parameterization of the Environment

In order to completely specify the optic flow pattern (2.3) in closed form, simplifying assumptions are required on the shape of the nearness function $\mu(\gamma, \beta, \mathbf{q}) \in L^2(S^2)$. The nearness encodes the vehicle's relative pose $\mathbf{q} = (x, y, z, \phi, \theta, \psi)$ with

respect to the environment, where (x, y, z) are the coordinates of the vantage point with respect to an inertial frame $\mathcal{F} = \{\hat{\mathbf{e}}_x, \hat{\mathbf{e}}_y, \hat{\mathbf{e}}_z\}$ located at the equilibrium position, and (ψ, θ, ϕ) are the 3-2-1 Euler angles representing the relative attitude of the body frame $\mathcal{B}$ with respect to $\mathcal{F}$.

Two baseline world types will be modelled, and the built-in parameters of each environment can be altered to obtain a variety of other navigationally relevant scenarios.

1. **Flat-surface World.** Consider the general scenario of a vehicle surrounded by flat surfaces positioned North, East, South, West, up and down relative to the inertial vehicle frame. The desired position of the vehicle is some nominal location within the enclosed room. When the vehicle deviates from its nominal position (Fig. 2.3A), the deviation is captured by the orthogonal quantities (x, y, z). The objective is to find a model for the distance to obstacles in this general environment.

   Expressed as a vector quantity, the distance to a surface along direction $\hat{\mathbf{e}}_r$ from a point $\mathbf{r}$ on the sphere is $\mathbf{d} = d(\gamma, \beta, \mathbf{q})\ \hat{\mathbf{e}}_r$, assuming that $\|r\| \ll \|d(\gamma, \beta)\|$. For the surface below the vehicle (Fig. 2.3B), the altitude is denoted as $h_D - z$. The component of $\mathbf{d}$ along the direction of the fixed frame $\mathcal{F}$ vertical $\hat{\mathbf{e}}_z$ is therefore given by

$$\langle \mathbf{d}, \hat{\mathbf{e}}_z \rangle \;=\; h_D - z. \tag{2.6}$$

   To derive the general expression for $\mu(\gamma, \beta, \mathbf{q}) = 1/d(\gamma, \beta, \mathbf{q})$, the vector $\mathbf{d}$
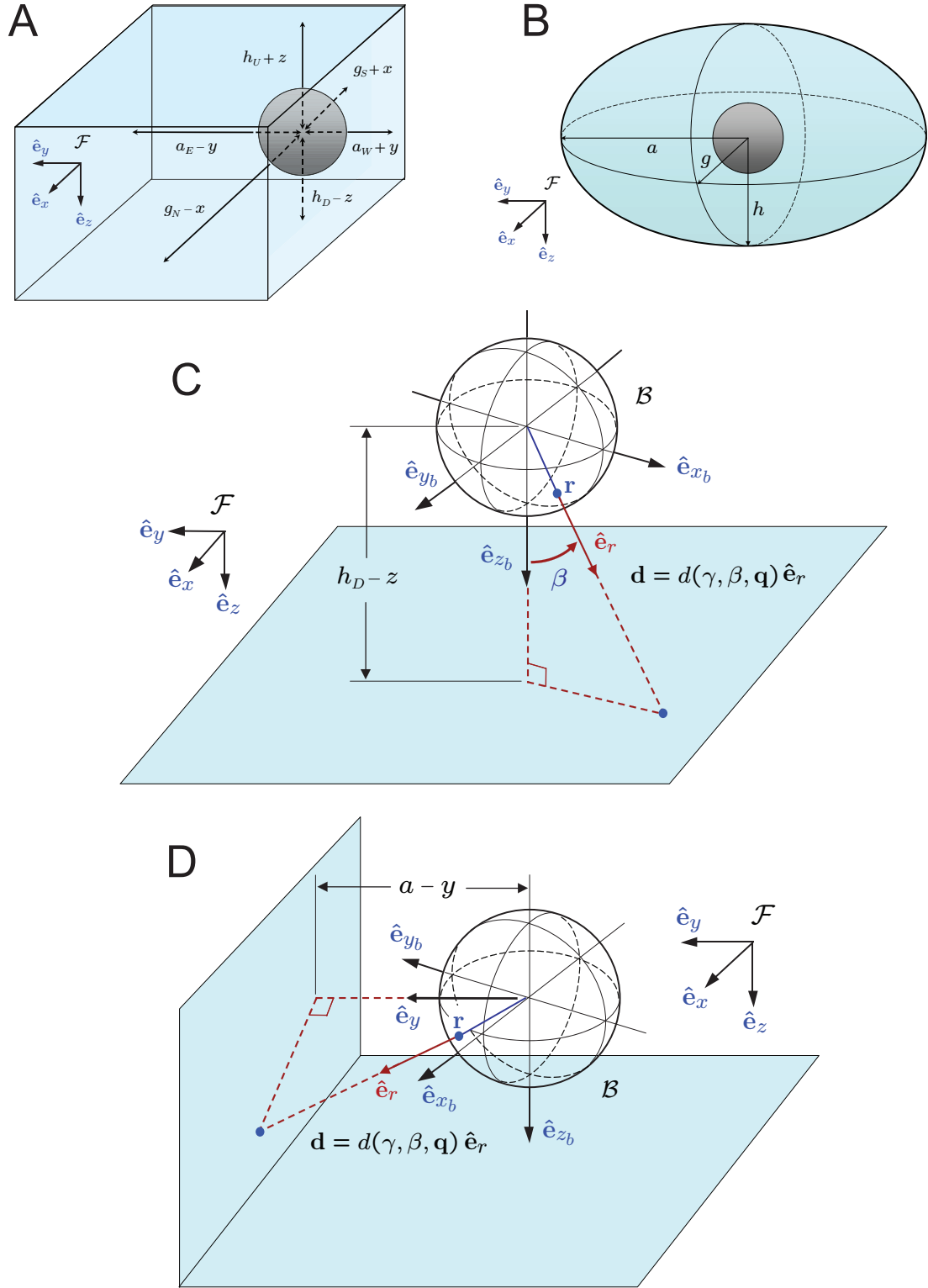
Figure 2.3: Environment models for nearness function approximation: (A) flat-surface world with translational perturbations, (B) ellipsoid world with centered vehicle, (C) outdoor obstacle-free flight (and definition of the distance function $d(\gamma, \beta, \mathbf{q})$), (D) outdoor flight with east-side obstacle

needs to be expressed in $\mathcal{F}$ coordinates for a general orientation to facilitate the extraction of the $\hat{\mathbf{e}}_z$ component. Consider the spherical coordinate unit vector $\hat{\mathbf{e}}_r$ (Fig. 2.2) expressed in $\mathcal{B}$ frame coordinates

$$[\hat{\mathbf{e}}_r]_\mathcal{B} \;=\; \begin{pmatrix} \sin\beta\cos\gamma \\ \sin\beta\sin\gamma \\ \cos\beta \end{pmatrix}. \tag{2.7}$$

For an arbitrary orientation of the body frame $\mathcal{B}$, the components of $\hat{\mathbf{e}}_r$ expressed in $\mathcal{F}$ coordinates are given by $[\hat{\mathbf{e}}_r]_\mathcal{F} = \mathcal{R}_{\mathcal{B}\mathcal{F}}^{-1}\,[\hat{\mathbf{e}}_r]_\mathcal{B}$:

$$[\hat{\mathbf{e}}_r]_\mathcal{F} \;=\; \begin{pmatrix} c\theta c\psi & c\theta s\psi & -s\theta \\ s\phi s\theta c\psi - c\phi s\psi & s\phi s\theta s\psi + c\phi c\psi & s\phi c\theta \\ c\phi s\theta c\psi + s\phi s\psi & c\phi s\theta s\psi - s\phi c\psi & c\phi c\theta \end{pmatrix}^{-1} \begin{pmatrix} s\beta c\gamma \\ s\beta s\gamma \\ c\beta \end{pmatrix}. \tag{2.8}$$

Hence the $\hat{\mathbf{e}}_z$ component of $\mathbf{d}$ can be expressed as

$$\langle \mathbf{d}, \hat{\mathbf{e}}_z \rangle \;=\; d\,\langle\,[\hat{\mathbf{e}}_r]_\mathcal{F}\,, \hat{\mathbf{e}}_z\,\rangle \;=\; d\left[s\beta(s\phi c\theta s\gamma - s\theta c\gamma) + c\beta c\phi c\theta\right], \tag{2.9}$$

which (combining with (2.6) and $\mu = 1/d$) yields the lower-surface nearness function for a general pose $\mathbf{q}$ of the vehicle via $\mu(\gamma,\beta) = \frac{\langle\,[\hat{\mathbf{e}}_r]_\mathcal{F}, \hat{\mathbf{e}}_z\,\rangle}{h_D - z}$.

This concept can easily be extended to a surface above the vehicle by taking $\mu(\gamma,\beta) = \frac{\langle\,[\hat{\mathbf{e}}_r]_\mathcal{F}, -\hat{\mathbf{e}}_z\,\rangle}{h_U + z}$. For a wall to the east of the vehicle, $\mu(\gamma,\beta) = \frac{\langle\,[\hat{\mathbf{e}}_r]_\mathcal{F}, \hat{\mathbf{e}}_y\,\rangle}{a_E - y}$. Repeating this method for west, north and south walls, the individual μ-

functions can be combined to obtain a piece-wise function that describes the nearness to surfaces when the vehicle is inside an enclosed rectangular-prism;

$$
\mu \;=\; \begin{cases}
\dfrac{\text{s}\beta(\text{c}\psi\text{c}\theta\text{c}\gamma + \text{s}\gamma(\text{s}\phi\text{s}\theta - \text{c}\phi\text{s}\psi\text{c}\theta)) + \text{c}\beta(\text{s}\phi\text{s}\psi\text{c}\theta + \text{c}\phi\text{s}\theta)}{g_N - x} & \text{front wall} \\[2.2ex]
-\dfrac{\text{s}\beta(\text{c}\psi\text{c}\theta\text{c}\gamma + \text{s}\gamma(\text{s}\phi\text{s}\theta - \text{c}\phi\text{s}\psi\text{c}\theta)) + \text{c}\beta(\text{s}\phi\text{s}\psi\text{c}\theta + \text{c}\phi\text{s}\theta)}{g_S + x} & \text{rear wall} \\[2.2ex]
\dfrac{\text{s}\beta(\text{c}\gamma\text{c}\theta\text{s}\psi + \text{s}\gamma(\text{s}\phi\text{s}\theta\text{s}\psi + \text{c}\phi\text{c}\psi)) + \text{c}\beta(\text{c}\phi\text{s}\theta\text{s}\psi - \text{s}\phi\text{c}\psi)}{a_E - y} & \text{right wall} \\[2.2ex]
-\dfrac{\text{s}\beta(\text{c}\gamma\text{c}\theta\text{s}\psi + \text{s}\gamma(\text{s}\phi\text{s}\theta\text{s}\psi + \text{c}\phi\text{c}\psi)) + \text{c}\beta(\text{c}\phi\text{s}\theta\text{s}\psi - \text{s}\phi\text{c}\psi)}{a_W + y} & \text{left wall} \\[2.2ex]
\dfrac{\text{s}\beta(\text{s}\phi\text{c}\theta\text{s}\gamma - \text{s}\theta\text{c}\gamma) + \text{c}\beta\text{c}\phi\text{c}\theta}{h_D - z} & \text{ground} \\[2.2ex]
-\dfrac{\text{s}\beta(\text{s}\phi\text{c}\theta\text{s}\gamma - \text{s}\theta\text{c}\gamma) + \text{c}\beta\text{c}\phi\text{c}\theta}{h_U + z} & \text{ceiling}
\end{cases}
\tag{2.10}
$$

Parameters $\{g_N, g_S, a_E, a_W, h_D, h_U\}$ represent the desired distance from the walls at the equilibrium position. The bounds for the validity ranges of each μ sub-function specify where the surfaces intersect, but due to their complexity they can only be computed numerically.

2. **Ellipsoid World.** Consider the scenario of a vehicle inside an ellipsoid. Define an intermediary body frame $\mathcal{B}'$ attached to the vehicle but aligned with the inertial frame $\mathcal{F}$, which is offset from the vehicle by (x, y, z). The conventional body frame $\mathcal{B}$ is aligned with the geometric axes of the vehicle. The kinematic

transforms between the frames are:

$$\mathcal{T}_{\mathcal{F}\mathcal{B}'} = \begin{pmatrix} 1 & 0 & 0 & x \\ 0 & 1 & 0 & y \\ 0 & 0 & 1 & z \\ 0 & 0 & 0 & 1 \end{pmatrix} \qquad \mathcal{T}_{\mathcal{B}'\mathcal{B}} = \begin{pmatrix} \mathcal{R}_{\mathcal{B}\mathcal{F}}^{-1} & \mathbf{0}_{3\times 1} \\ \mathbf{0}_{1\times 3} & 1 \end{pmatrix}. \tag{2.11}$$

where $\mathcal{R}_{\mathcal{B}\mathcal{F}}^{-1}$ is given in (2.8). If the ellipse is aligned with the inertial frame, a vector $\mathbf{d}_{\mathcal{F}}$ from the ellipsoid center to a point on the surface can be written as

$$\mathbf{d}_{\mathcal{F}} = \begin{pmatrix} b\cos\gamma_{\mathcal{F}}\sin\beta_{\mathcal{F}} \\ a\sin\gamma_{\mathcal{F}}\sin\beta_{\mathcal{F}} \\ h\cos\beta_{\mathcal{F}} \end{pmatrix}, \tag{2.12}$$

where $(2b, 2a, 2h)$ define the ellipsoid dimensions and $(\gamma_{\mathcal{F}}, \beta_{\mathcal{F}})$ are inertial-frame referred azimuth and elevation angles. If transported to the $\mathcal{B}'$ frame, the vector from the vehicle center to a point on the surface is obtained from

$$\begin{pmatrix} \mathbf{d}_{\mathcal{B}'} \\ 1 \end{pmatrix} = \mathcal{T}_{\mathcal{F}\mathcal{B}'}^{-1} \begin{pmatrix} \mathbf{d}_{\mathcal{F}} \\ 1 \end{pmatrix} \tag{2.13}$$

then the nearness μ is $1/d = 1/\|\mathbf{d}_{\mathcal{B}'}\|$, resulting in (2.15). Because (2.12) is dependent on $(\gamma_{\mathcal{F}}, \beta_{\mathcal{F}})$, expressions for these must be found. The additional information comes from taking the body-frame vector to an arbitrary point

$d\,[\hat{\mathbf{e}}_r]_{\mathcal{B}}$, Eq. (2.7), and transporting into the inertial frame.

$$\begin{pmatrix} \mathbf{d}_{\mathcal{F}} \\ 1 \end{pmatrix} = \mathcal{T}_{\mathcal{F}\mathcal{B}'}\,\mathcal{T}_{\mathcal{B}'\mathcal{B}} \begin{pmatrix} d\,[\hat{\mathbf{e}}_r]_{\mathcal{B}} \\ 1 \end{pmatrix}. \tag{2.14}$$

Equating (2.14) with (2.12), allows solution for $(\gamma_{\mathcal{F}}, \beta_{\mathcal{F}})$ (see (2.16)). This last step is used to solve directly for d in the flat-surface world case, because the z-component of $\mathbf{d}_{\mathcal{F}}$ does not depend on viewing angle.

For the ellipsoid, the nearness is a continuous function of the viewing angle. However, a closed form expression is not possible, therefore the nearness is found by solving a non-linear equation in d (note $\mu = 1/d$),

$$d = \sqrt{(\mathrm{c}(\gamma_{\mathcal{F}})\mathrm{s}(\beta_{\mathcal{F}})g - x)^2 + (\mathrm{s}(\gamma_{\mathcal{F}})\mathrm{s}(\beta_{\mathcal{F}})a - y)^2 + (\mathrm{c}(\beta_{\mathcal{F}})h - z)^2} \tag{2.15}$$

$$\gamma_{\mathcal{F}} = \tan^{-1}\left(\frac{b}{a} \cdot \frac{(\mathrm{c}\theta\mathrm{s}\psi\mathrm{c}\gamma + (\mathrm{s}\phi\mathrm{s}\theta\mathrm{s}\psi + \mathrm{c}\phi\mathrm{c}\psi)\mathrm{s}\gamma)\mathrm{s}\beta + (\mathrm{c}\phi\mathrm{s}\theta\mathrm{s}\psi - \mathrm{s}\phi\mathrm{c}\psi)\mathrm{c}\beta + \frac{y}{d}}{(\mathrm{c}\theta\mathrm{c}\psi\mathrm{c}\gamma + (\mathrm{s}\phi\mathrm{s}\theta\mathrm{c}\psi - \mathrm{c}\phi\mathrm{s}\psi)\mathrm{s}\gamma)\mathrm{s}\beta + (\mathrm{c}\phi\mathrm{s}\theta\mathrm{c}\psi + \mathrm{s}\phi\mathrm{s}\psi)\mathrm{c}\beta + \frac{x}{d}}\right)$$

$$\beta_{\mathcal{F}} = \cos^{-1}\left(\frac{d}{h}\left(\mathrm{s}\phi\mathrm{c}\theta\mathrm{s}\gamma\mathrm{s}\beta - \mathrm{s}\theta\mathrm{c}\gamma\mathrm{s}\beta + \mathrm{c}\phi\mathrm{c}\theta\mathrm{c}\beta + \frac{z}{d}\right)\right). \tag{2.16}$$

The indoor-like environments described by (2.10) and (2.15) can be simplified to environments useful for outdoor navigation. Flight above a flat surface with no obstacles is modeled by the case where $\{g_N, g_S, a_E, a_W, h_U\} \rightarrow \infty$ (Fig. 2.3C). If there is an east-side obstacle then $\{g_N, g_S, a_W, h_U\} \rightarrow \infty$ (Fig. 2.3D), and Fig. 2.4B shows the expected optic flow pattern for straight-and-level-flight. For a west-side obstacle $\{g_N, g_S, a_E, h_U\} \rightarrow \infty$, and for the case where there are obstacles on both sides of the vehicle $\{g_N, g_S, h_U\} \rightarrow \infty$ and $a_E = a_W$ (Fig. 2.4A). The ellipsoid world

23

can also be separated into 8 ellipsoid segments if multi-axis asymmetries are desired.

For the case where measurements are confined to three orthogonal rings (Fig. 2.2B), the nearness functions for the outdoor flat-surface worlds simplify to those given in Tables 2.1.

Table 2.1: Outdoor flat-surface world with no front/rear surfaces; 1-D nearness sub-functions in the roll, pitch and yaw planes

	Floor	Right-side Wall with Floor	Tunnel with Floor
$\mu_{R,1}$	$\frac{c(\beta-\phi)c\theta}{h-z}$	$\frac{c(\beta-\phi)c\theta}{h-z}$	$\frac{c(\beta-\phi)c\theta}{h-z}$
$\mu_{R,2}$	0	$\frac{c(\beta-\phi)s\theta s\psi+s(\beta-\phi)c\psi}{a-y}$	$\frac{c(\beta-\phi)s\theta s\psi+s(\beta-\phi)c\psi}{a-y}$
$\mu_{R,3}$	0	0	$-\frac{c(\beta-\phi)s\theta s\psi+s(\beta-\phi)c\psi}{a+y}$
$\mu_{P,1}$	$\frac{-s\theta s\beta+c\theta c\phi c\beta}{h-z}$	$\frac{-s\theta s\beta+c\theta c\phi c\beta}{h-z}$	$\frac{-s\theta s\beta+c\theta c\phi c\beta}{h-z}$
$\mu_{P,2}$	0	0	0
$\mu_{Y,1}$	0	$\frac{c\theta s\psi c\gamma+s\gamma(s\phi s\theta s\psi+c\phi c\psi)}{a-y}$	$\frac{c\theta s\psi c\gamma+s\gamma(s\phi s\theta s\psi+c\phi c\psi)}{a-y}$
$\mu_{Y,2}$	0	0	$-\frac{c\theta s\psi c\gamma+s\gamma(s\phi s\theta s\psi+c\phi c\psi)}{a+y}$

2.3   Tangential Cell Analogues

Insect tangential cells are believed to pool the outputs of large numbers of local optic flow estimates and respond with graded membrane potentials whose magnitude is both spatially and directionally selective [30, 2, 21, 22]. Essentially, the integrated output is a comparison between the cell's ingrained spatial directional template (e.g., Fig. 5.1) and that of the visual stimulus (e.g., Fig. 2.4). Mathematically, this comparison can be modeled as an inner product $\langle \mathbf{a}, \mathbf{b} \rangle$, analogous to the dot product between vectors, which is an abstraction of the angle between objects $\mathbf{a}$ and $\mathbf{b}$. Tangential cell analogues for spherical imaging surfaces are defined here as

an inner product on the function space $L^2(S^2, \mathbb{R}^2)$ between the instantaneous optic flow $\dot{\mathbf{Q}}$ and any square-integrable weighting function $\mathbf{F} = F^\gamma \, \hat{\mathbf{e}}_\gamma + F^\beta \, \hat{\mathbf{e}}_\beta$,

$$y = \langle \dot{\mathbf{Q}}, \mathbf{F} \rangle \quad = \int_{S^2} \dot{\mathbf{Q}} \cdot \mathbf{F} \, d\Omega, \qquad (2.17)$$

where '$\cdot$' denotes the dot product in $\mathbb{R}^2$ and $d\Omega = \sin\beta \, d\beta \, d\gamma$ is the solid angle of the sphere. This can also be thought of as a projection of $\dot{\mathbf{Q}}$ on to $\mathbf{F}$, with the objective of decoding information about the vehicle's relative pose $\mathbf{q}$ and velocity $\dot{\mathbf{q}} = (u, v, w, p, q, r)$ with respect to the environment. Note that the integration domain of this inner product may be a potentially disconnected subset of the full sphere surface.

The objective from a controls stance is to select weighting patterns $\mathbf{F}$ that extract relevant information from the measured optic flow patterns to aid navigation. One possible starting point would be the set of tangential cell directional templates used by insects (Figs. 5.1 and 5.2). A less constrained approach involves trying many different patterns by taking elements from an infinite basis, such as the set of real spherical harmonics, which are orthogonal functions on $L^2(S^2)$. These functions take the form

$$Y_{l,m}(\beta, \gamma) \quad = \quad N_l^m \Phi_l^m(\cos\beta) \begin{cases} \cos m\gamma & m \geq 0 \\ \\ \sin |m|\gamma & m < 0 \end{cases}, \qquad (2.18)$$

where $\Phi_l^m(\cos\beta)$ is the associated Legendre function, $\{l, m\} \in \mathbb{Z}$, $l \geq 0$, $|m| \leq l$, and the factor N_l^m is a normalization coefficient. The resulting wide-field integrated

outputs for component weighting functions $\mathbf{F}_{l,m}^k = Y_{l,m}^k \, \hat{\mathbf{e}}_k$, for $k \in \{\gamma, \beta\}$ are then given by

$$y_{l,m}^k(\mathbf{x}) \;=\; \langle \dot{\mathbf{Q}}, \mathbf{F}_{l,m}^k \rangle \;=\; \int_0^{2\pi} \int_0^{\pi} \dot{Q}^k(\mathbf{x}) \, Y_{l,m}^k \sin \beta \; d\beta \; d\gamma. \qquad (2.19)$$

2.4   Interpreting WFI Outputs

The objective is to characterize the relationship between weighting functions $\mathbf{F}$ and the relative state $\mathbf{x} = (x, y, z, \phi, \theta, \psi, u, v, w, p, q, r) \in \mathbb{R}^n$ encoded by WFI outputs. This is achieved by linearizing the outputs about a nominal optic flow pattern, which corresponds to a nominal state $\mathbf{x}_0$. A desired (equilibrium) optic flow pattern is specified by a pre-defined amount of longitudinal and lateral asymmetry. The pattern in Fig. 2.4A, for example, corresponds physically with flight centered between obstacles and at some desired altitude above ground. This is expressed mathematically by the nominal trajectory $\mathbf{x}_0 = (0, 0, 0, 0, 0, 0, u_{\text{ref}}, 0, 0, 0, 0, 0)$, where u_{ref} is the target forward speed.

To provide an intuitive illustration of the linkages between outputs and weighting patterns, consider a tunnel environment with infinitely high walls, $\{g_N, g_S, h_U, h_D\} \to \infty$ and $a_E = a_W$ (Fig. 2.4C). Several spherical harmonic projections (2.19) using this optic flow model are presented in Fig. 2.5. For example, $y_{0,0}^{\beta}$ provides a measure of the heave velocity when the signal is linearized about $\mathbf{x}_0$. It quantifies the goodness of match between the actual optic flow field and a purely longitudinal template pattern defined by the harmonic $Y_{0,0}^{\beta}$, which has constant magnitude for all points on the sphere. A climbing vehicle experiences longitudinal optic flow on both sides
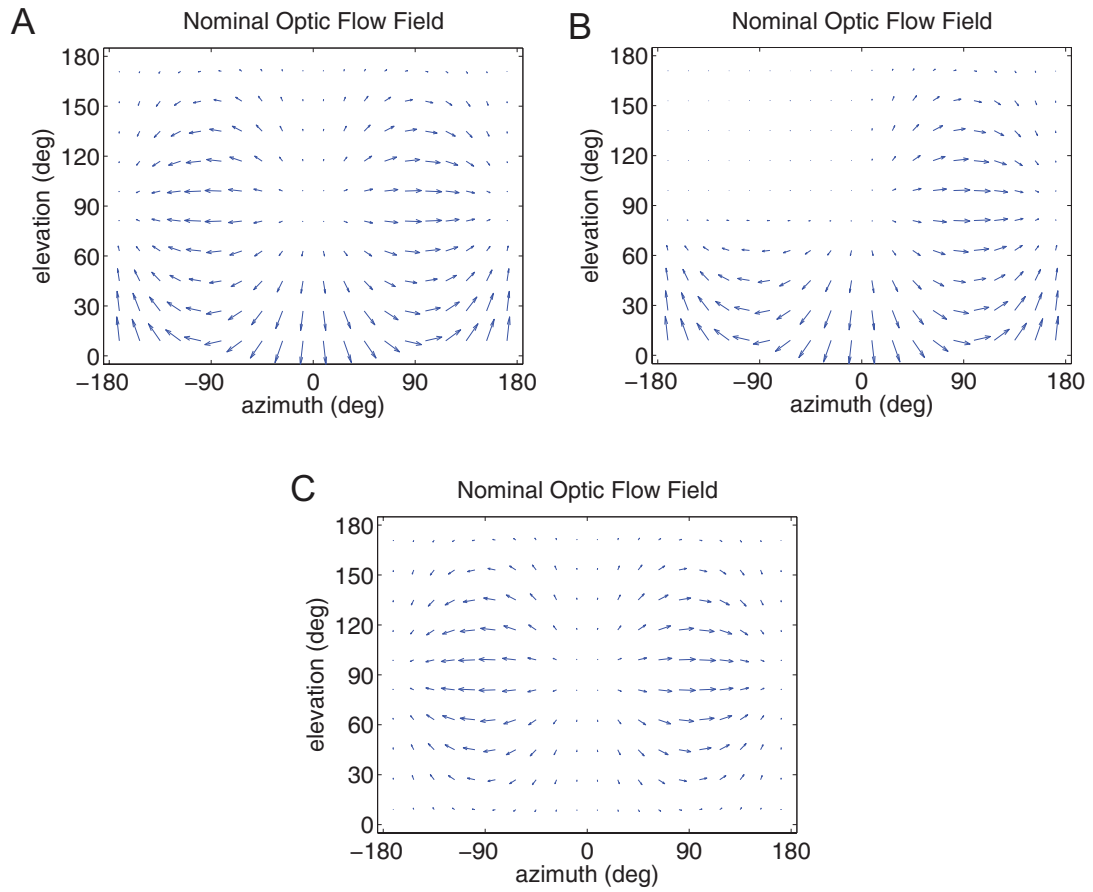
Figure 2.4: Nominal optic flow patterns; (A) tunnel with floor, (B) right-side wall with floor, (C) tunnel

of the vehicle and this deviation from the nominal pattern is captured by the WFI output $y_{0,0}^{\beta}$. The $Y_{1,1}^{\beta}$ harmonic weights the front and rear of the vehicle strongly but with opposite signs, thus capturing any forward-aft optic flow asymmetry (induced by pitch-axis rotation) in the projection. The lateral offset from the tunnel center is captured by the $y_{2,2}^{\gamma}$ output, which places large negative azimuthal-flow weights on both sides of the vehicle. If the vehicle is nearer the right-side wall the optic flow will be larger on that side (where azimuthal flow is positive) thus the WFI output will be negative. If the left-side wall is nearer then the negative-direction azimuthal optic flow will be stronger and the output will be positive. The positive weighting of the optic flow at the front and rear of the vehicle acts to filter out yaw rotation motion from the projection.

Optic Flow, $\dot{\mathbf{Q}}$ Weighting Pattern, $\mathbf{F_i}$

Sinking

Right Hemisphere   *Left Hemisphere*

$$\langle\, \dot{\mathbf{Q}}\,,\, Y_{0,0}^{\beta}\,\rangle \;\propto\; w\left(\frac{1}{a}\right)$$

Pitching Downward

$$\langle\, \dot{\mathbf{Q}}\,,\, Y_{1,1}^{\beta}\,\rangle \;\propto\; -q$$

Lateral Weightings   *Fore/aft weightings filter out yaw-rotation component*

Off-Center

$$\langle\, \dot{\mathbf{Q}}\,,\, Y_{2,2}^{\gamma}\,\rangle \;\propto\; -y\left(\frac{u_0}{a}\right)$$
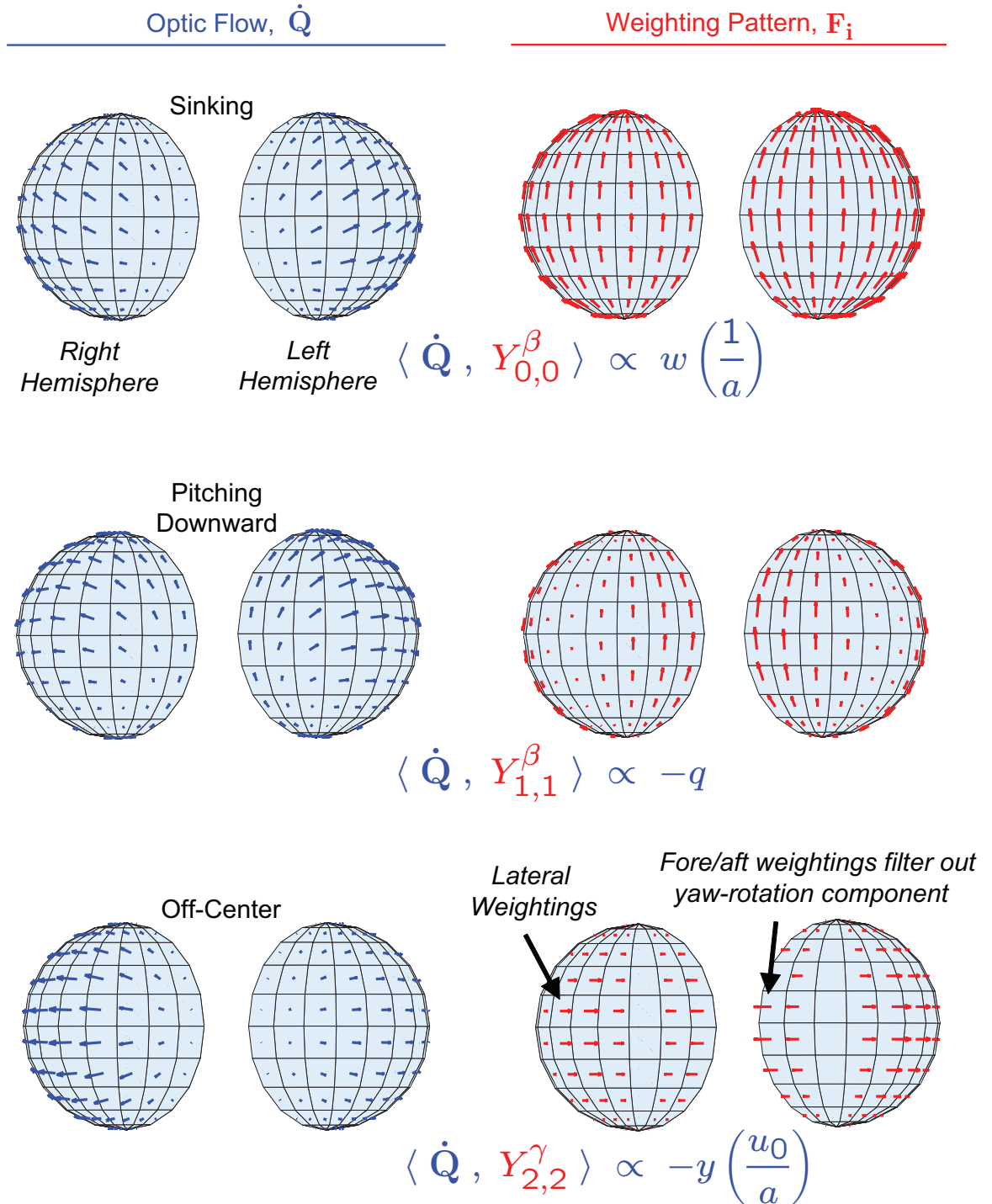
Figure 2.5: WFI of optic flow in an infinite tunnel. The optic flow field is measured (represented here using 'bug eyes') then integrated over the sphere against a weighting pattern to produce a scalar output. Spherical harmonics up to 2nd degree are sufficient to obtain relative measurements of all navigational and stability states in this simple environment. Undesired asymmetries in the optic flow pattern can be eliminated by applying these quantities as feedback to appropriate actuators, thus forcing the vehicle to track a symmetric pattern (Fig. 2.4C).

29

Chapter 3

Closed-Loop Architecture

Given the WFI operation developed in Chapter 2, the control task is to synthesize a control loop that stabilizes the vehicle about a desired optic flow pattern (or trajectory). In this chapter, a linear feedback architecture is proposed and traditional engineering tools are applied to incorporate WFI into the feedback loop in a way that minimizes computations, encompasses feedback gain optimality, and robustness to measurement noise and environment uncertainty.

Many previous studies, using real robotic platforms, use the WFI concept to close the navigation loop with on-board measurements of optic flow [37, 38, 39, 42, 43, 44, 45, 48, 49, 50, 52, 53]; which is generally motivated by computational constraints of the on-board processor. The weighting patterns employed in these experiments almost always consist of a concatenation of uniformly weighted patches on the sphere. For example, basic obstacle navigation can be achieved by generating a lateral steering command from a comparison of optic flow averaged over a left-pointing camera against optic flow averaged over a right-pointing camera (e.g., Fig. 7.1A). Some studies generate a climb rate command by regulating averaged optic flow on a down-pointing camera to a desired reference level for terrain following. Whilst these architectures are consistent with that proposed in this thesis (Fig. 3.1), the utilized weighting patterns are designed by trial and error and often require

removal of rotation motion from the optic flow field. There is scope for optimization of these patterns by considering the signal information content generated by the WFI operations, and this chapter seeks to exploit that.

3.1 Feedback Control Design

This section states the general form of the control law that will be utilized throughout the thesis, and introduces equivalent expanded versions that aid the design process. To maintain simplicity, and to fit with the low computations paradigm, only linear static compensators shall be considered. The most computationally efficient feedback methodology (Fig. 3.1A) would involve a single WFI operation per actuator, such that the WFI output is an actuator input command u_k;

$$u_k = \langle \dot{\mathbf{Q}}, \mathbf{F}_{u_k} \rangle + u_{k,\text{ref}} + \sum_s \bar{K}_{k,y_s} y_s. \tag{3.1}$$

Additional terms are included to account for intended deviation from the trim point $\mathbf{x}_0$ (via control $u_{k,\text{ref}}$) and feedback of non-WFI-based sensor outputs y_s. Note that $\mathbf{u}$ already represents the perturbation from trim input.

Choosing sensor-to-actuator weightings $\mathbf{F}_{u_k}$ that stabilize the vehicle is nontrivial, but the problem can be simplified by beginning with fixed weightings $\mathbf{F}_{y_j}$ (e.g., tangential cell patterns or spherical harmonics) and then applying static linear feedback to the WFI outputs y_j (Fig. 3.1B);

$$u_k = \sum_j \bar{K}_{k,y_j} \langle \dot{\mathbf{Q}}, \mathbf{F}_{y_j} \rangle + u_{k,\text{ref}} + \sum_s \bar{K}_{k,y_s} \tilde{y}_s. \tag{3.2}$$

31
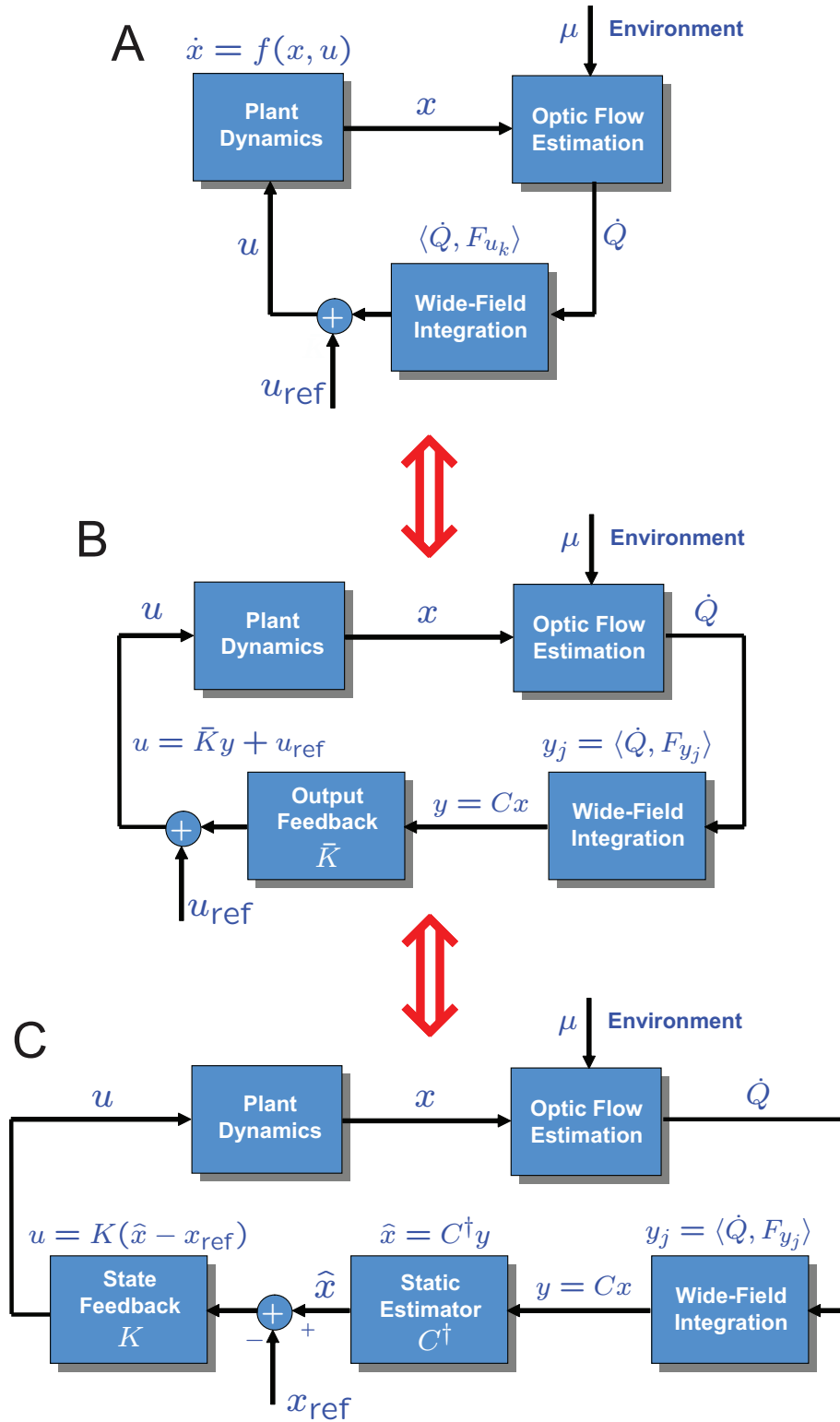
Figure 3.1: Equivalent closed-loop architectures; (A) direct feedback of carefully selected WFI outputs, (B) gained feedback of arbitrary WFI outputs, (C) state extraction from arbitrary WFI outputs and state feedback

32

The gain matrix $\bar{K}$ can be designed using existing tools such as output LQR and then the computationally efficient control law (3.1) can be recovered by setting

$$\mathbf{F}_{u_k} \;\; = \;\; \sum_j \bar{K}_{k,y_j} \mathbf{F}_{y_j}, \tag{3.3}$$

due to linearity of the WFI operator. Here, $\mathbf{F}_{y_j}$ has entries of zeroes for non-WFI-based outputs.

If there are more WFI measurements than states then the system is overdetermined, permitting further optimization by preferential weighting of measurements. Such optimization can reduce noise throughput in the sensor to actuator mapping and increase robustness to uncertainty in the environment structure. However, output LQR [71], for example, does not readily incorporate preferential measurement weighting. Therefore, we introduce an additional step in the control design process; the WFI outputs are first converged to static estimates of state $\hat{x}_i$ via a weighted least squares inversion, then any state feedback matrix design tool can be used to map the state estimates to actuator commands. The fixed-perturbation from trim, which determines the desired behavior of the vehicle, can also be more intuitively specified as a state vector, $\mathbf{x}_{\text{ref}}$. Assuming additionally that the non-WFI-based sensors provide direct measurements of states, the revised control law is (Fig. 3.1C):

$$u_k \;\; = \;\; \sum_i K_{k,x_i} \left(\sum_j \left(C_{i,j}^{\dagger} \langle \dot{\mathbf{Q}}, \mathbf{F}_{y_j} \rangle \right) - x_{i,\text{ref}} \right) + \sum_s K_{k,x_s} (\hat{x}_s - x_{s,\text{ref}}). \tag{3.4}$$

This is equivalent to (3.1) with the weighting pattern choice

$$\mathbf{F}_{u_k} \;=\; \sum_i K_{k,x_i} \sum_j C_{i,j}^\dagger \mathbf{F}_{y_j} \tag{3.5}$$

and the fixed-perturbation from trim $u_{k,\mathrm{ref}} = -\sum_i K_{k,x_i} x_{i,\mathrm{ref}}$.

The above method addresses the problem of designing $\mathbf{F}_{u_k}$ by separating it into tractable engineering problems for which solutions are already available. Fig. 3.1A illustrates the architecture intended for real-time implementation, whilst architectures B and C are equivalent forms that allow the application of traditional tools; non-WFI sensor feedback was omitted to avoid clutter of the diagrams. Note that architecture 3.1B could also be implemented in real-time if the weighting patterns were fixed (e.g., as is the case for an insect). Equivalence between architectures is true if the following relations hold:

$$
\begin{aligned}
F_{\mathbf{u}} &= \bar{K} F_{\mathbf{y}} \\
\bar{K} &= K C^\dagger \\
\mathbf{u}_{\mathrm{ref}} &= -K \mathbf{x}_{\mathrm{ref}} \;,
\end{aligned}
\tag{3.6}
$$

where $F_{\mathbf{u}}$ is a matrix of actuator weighting patterns and $F_{\mathbf{y}}$ is a matrix of arbitrary weighting patterns used to begin the control synthesis process. Optimality of the designed actuator weighting patterns is partly dependent on $F_{\mathbf{y}}$, but this will be explored in Section 3.2.2.3.

3.2   Stage 1: Optimal Static Estimation of Relative States

Optic flow cannot be measured directly, it must be inferred from the spatiotemporal patterns of luminance incident on an imaging surface. Therefore, the optic flow estimation process introduces error in the measurements, which is compounded by sensor noise and contrast/texture variations occurring in the environment. Additional uncertainty associated with the nearness function is present due to variation in the obstacle distributions from the baseline environments assumed in Section 2.2. In this section an offline procedure for designing a static estimator $C^\dagger$ that accounts for these uncertainties in the optic flow model (2.3) and environment, e.g., (2.10), is developed. This is the first step in the synthesis of (3.4), which is an intermediary for constructing the computationally efficient control law (3.1).

3.2.1   Measurement Model

Given $M \geq n$ linearly independent weighting functions $F_{\mathbf{y}} = \{\mathbf{F}_{y_j}, \; j = 1, \ldots, M\}$, WFI outputs (2.17) using the optic flow model (2.3) can be linearized for small perturbations about $\mathbf{x}_0$, which will yield linear output equations of the form $\mathbf{y} = C\mathbf{x}$. Accounting for environment uncertainty and measurement noise, the observation equation becomes

$$\tilde{\mathbf{y}} = C\mathbf{x} + \mathbf{w} \tag{3.7}$$

$$C = C_0 + \delta C,$$

where $\tilde{\mathbf{y}} \in \mathbb{R}^M$ are the measured outputs, the noise $\mathbf{w}$ is zero mean $E\{\mathbf{w}\} = 0$ with covariance $E\{\mathbf{w}\mathbf{w}^T\} = R_{\mathbf{w}}$. The quantity δC is assumed to be a zero-mean random perturbation $E\{\delta C\} = 0$ which captures the variation in the nearness function $\mu(\gamma, \beta, \mathbf{q})$ from the mean - used in C_0. It is further assumed that $E\{\mathbf{w}\delta C^T\} = 0$. Without a priori knowledge of the statistical distribution of environments that the vehicle will encounter, C_0 ca be approximated with an unweighted average of several limit-case environments from Section 2.2. For example, if one ignores front and rear surfaces $(g \to \infty)$,

$$C_0 \;=\; \frac{1}{4}\Big(C\big(a_E=a_W=\infty\big) + C\big(a_E=1,a_W=\infty\big) + C\big(a_E=\infty,a_W=1\big) + C\big(a_E=a_W=1\big)\Big), (3.8)$$

where $a = 1$ m defines a practical minimum for the nominal wall clearance or the half-width of any gaps between obstacles an MAV might encounter.

3.2.2 Weighted Least Squares Inversions

The problem is now posed in the form of a standard static linear estimation problem, where one seeks the solution of an overdetermined, inconsistent set of linear equations given by (3.7). The optimal choice that minimizes the weighted $(W > 0)$ sum square of the residual errors $J = \frac{1}{2}(\tilde{\mathbf{y}} - C\hat{\mathbf{x}})^T W (\tilde{\mathbf{y}} - C\hat{\mathbf{x}})$ is given by $\hat{\mathbf{x}} = C^{\dagger}\tilde{\mathbf{y}}$, where

$$C^{\dagger} \;=\; \left(C_0^T W C_0\right)^{-1} C_0^T W. \tag{3.9}$$

The choice for the weighting matrix that acts to penalize high measurement noise and environmental model uncertainty is $W = (R_{\mathbf{w}} + R_{\delta C})^{-1}$.

3.2.2.1   Noise Covariance Matrix

To obtain an expression for $R_{\mathbf{w}}$, it is first assumed that optic flow measurements taken at discrete locations on the sphere are affected by two-dimensional additive noise $\boldsymbol{\eta}(\gamma, \beta)$ with variance σ_η^2. Additive measurement noise propagates through the WFI operator as follows:

$$y_i = \langle \dot{\mathbf{Q}} + \boldsymbol{\eta}, \mathbf{F}_{y_i} \rangle = \langle \dot{\mathbf{Q}}, \mathbf{F}_{y_i} \rangle + \langle \boldsymbol{\eta}, \mathbf{F}_{y_i} \rangle. \tag{3.10}$$

Assuming the noise is zero mean, the noise at the WFI output level $w_i = \langle \boldsymbol{\eta}, \mathbf{F}_{y_i} \rangle$ is also zero mean. The noise covariance between two WFI outputs then becomes

$$R_{\mathbf{w}, ij} = E\{w_i w_j\} = E\{\langle \boldsymbol{\eta}, \mathbf{F}_{y_i} \rangle \langle \boldsymbol{\eta}, \mathbf{F}_{y_j} \rangle\}. \tag{3.11}$$

In real applications, optic flow is sampled discretely at a series of $\mathcal{K}$ measurement nodes. The expansion of w_i is therefore

$$w_i \;=\; \Delta\beta\,\Delta\gamma \sum_{k=1}^{\mathcal{K}} \sin\beta_k \left(\eta_\gamma(\gamma_k, \beta_k) F_{y_i}^\gamma(\gamma_k, \beta_k) + \eta_\beta(\gamma_k, \beta_k) F_{y_i}^\beta(\gamma_k, \beta_k)\right). \tag{3.12}$$

To simplify the cross-multiplication of all the terms in $E\{w_i w_j\}$, the following vectors are defined:

$$\mathcal{X}_\gamma = \{F_{y_i}^\gamma(\gamma_k, \beta_k)\sin\beta_k, k = 1, \ldots, \mathcal{K}\} \qquad \mathcal{X}_\beta = \{F_{y_i}^\beta(\gamma_k, \beta_k)\sin\beta_k, k = 1, \ldots, \mathcal{K}\}$$

$$\mathcal{Y}_\gamma = \{F_{y_j}^\gamma(\gamma_k, \beta_k)\sin\beta_k, k = 1, \ldots, \mathcal{K}\} \qquad \mathcal{Y}_\beta = \{F_{y_j}^\beta(\gamma_k, \beta_k)\sin\beta_k, k = 1, \ldots, \mathcal{K}\}$$

$$\mathcal{Z}_\gamma = \{\eta_\gamma(\gamma_k, \beta_k), k = 1, \ldots, \mathcal{K}\} \qquad \mathcal{Z}_\beta = \{\eta_\beta(\gamma_k, \beta_k), k = 1, \ldots, \mathcal{K}\}.$$

The output noise covariance can now be written as

$$R_{\mathbf{w},ij} = (\Delta\beta\,\Delta\gamma)^2(\mathcal{X}_\gamma E\{\mathcal{Z}_\gamma \mathcal{Z}_\gamma^T\}\mathcal{Y}_\gamma^T + \mathcal{X}_\beta E\{\mathcal{Z}_\beta \mathcal{Z}_\gamma^T\}\mathcal{Y}_\gamma^T$$

$$+ \mathcal{X}_\gamma E\{\mathcal{Z}_\gamma \mathcal{Z}_\beta^T\}\mathcal{Y}_\beta^T + \mathcal{X}_\beta E\{\mathcal{Z}_\beta \mathcal{Z}_\beta^T\}\mathcal{Y}_\beta^T). \tag{3.13}$$

The $E\{\mathcal{Z}\mathcal{Z}^T\}$ matrices can be determined experimentally. The matrix elements may be a function of angular separation of nodes and the nominal optic flow magnitude at each node - indirectly specified as part of the controller (e.g. Fig. 2.4, which derives from $\mathbf{x}_{\text{ref}}$). This information was obtained in [72] for several optic flow algorithms.

To reduce dependency of the controller on the type of optic flow algorithm used, it is further assumed that the noise covariance is identical at each measurement node and in both directions $E\{\mathcal{Z}_\gamma \mathcal{Z}_\gamma^T\} = E\{\mathcal{Z}_\beta \mathcal{Z}_\beta^T\}$, and that noise is uncorrelated between directions $E\{\mathcal{Z}_\gamma \mathcal{Z}_\beta^T\} = 0$ and between measurement nodes $E\{\mathcal{Z}_\gamma \mathcal{Z}_\gamma^T\} = \sigma_\eta^2 I_{\mathcal{K}\times\mathcal{K}}$. Therefore,

$$R_{\mathbf{w},ij} = \sigma_\eta^2(\Delta\beta\,\Delta\gamma)^2(\mathcal{X}_\gamma \mathcal{Y}_\gamma^T + \mathcal{X}_\beta \mathcal{Y}_\beta^T), \tag{3.14}$$

38

which is an inner product between the two weighting patterns. The final form is given by (3.15).

$$R_{\mathbf{w},ij} = \Delta\beta \, \Delta\gamma \, \sigma_\eta^2 \, \langle \mathbf{F}_{y_i}, \mathbf{F}_{y_j} \rangle, \tag{3.15}$$

where $\Delta\beta$ and $\Delta\gamma$ define the angular spacing between adjacent nodes. Note that the measurement noise at the level of the WFI outputs approaches zero as the number of measurement nodes approaches infinity, providing significant improvement in signal to noise ratio - an attractive property of the WFI processing approach.

3.2.2.2 Model Uncertainty Penalty Matrix

To obtain an expression for $R_{\delta C}$ we assume $E\{\delta C\} = 0$, hence the covariance of the noise associated with modeling uncertainty is $R_{\delta C} = E\{\delta C x x^T \delta C^T\}$. The elements of $R_{\delta C}$ are the covariances between the modeling uncertainty terms of two WFI outputs:

$$\begin{aligned}
R_{\delta C,ij} &= \mathrm{Cov}(\sum_{k=1}^{n} \delta C_{ik} x_k, \sum_{l=1}^{n} \delta C_{jl} x_l) \\
&= \sum_{k=1}^{n} \sum_{l=1}^{n} \mathrm{Cov}(\delta C_{ik} x_k, \delta C_{jl} x_l).
\end{aligned} \tag{3.16}$$

With no prior knowledge of state, we set equal weightings ε of states with no cross-state weightings/correlations; i.e. $E\{xx^T\} = \varepsilon I$. It is also assumed that states are uncorrelated with environment perturbations. These assumptions set $k \neq l$ terms

39

in $R_{\delta C, ij}$ to zero and result in the final form given in (3.17).

$$R_{\delta C, ij} = \varepsilon \sum_{k=1}^{n} \mathrm{Cov}(\delta C_{ik}, \delta C_{jk}), \qquad (3.17)$$

where ε is a weighting constant that can be adjusted to specify the relative importance between the measurement noise $\mathbf{w}$ and the model uncertainty δC in the estimator. To compute $R_{\delta C}$ based on the assumed environment model, e.g., (2.10) or (2.15), the covariance terms are conservatively approximated using a list of δC matrices obtained from the limit-case environments as in (3.8). In the limit as $\varepsilon \to 0$, we recover the well known minimum variance Gauss-Markov estimator; the best estimator under a Gaussian noise assumption and the best linear estimator under any noise distribution. However, state estimates become more sensitive to changes in the environment. The purpose of $R_{\delta C, ij}$ is to take advantage of the notion that some structure in the modeled world is consistent across environments (e.g., the ground below the vehicle) and therefore concentrate WFI weightings on these areas. Setting $\varepsilon \gg \sigma_\eta^2$ tends to result in estimates that are not robust to noise. Tuning in a closed-loop simulation environment (Section 4.2.2.3) resulted in selection of $\varepsilon = \sigma_\eta^2$. The absolute magnitude of these terms does not affect the estimator; only relative magnitude is important.

3.2.2.3 Fisher Information

The Cramer-Rao bound states that any inversion of the observation equation will result in a state estimate covariance matrix $P = E\{(\hat{\mathbf{x}} - \mathbf{x})(\hat{\mathbf{x}} - \mathbf{x})^T\}$ that is

bounded below by the inverse of the Fisher information matrix F, i.e.

$$P \geq \mathsf{F}^{-1} = (C^T R_{\mathbf{w}}^{-1} C)^{-1}. \tag{3.18}$$

It is realized with equality under (3.9) if $\delta C = 0$, thus the norm of F provides a metric for examining how the field of view or initial choice of weighting function set affects the relative noise throughput (mapping from $\|\boldsymbol{\eta}\|$ to $\|\mathbf{w}\|$). Generally, discrepancy between the true environment and the assumed model manifests as bias in the C matrix ($\delta C \neq 0$) and hence bias in the state estimates. The numerical effect of such bias on the Cramer-Rao bound can be evaluated by applying the methods derived in [73]. However, this is not investigated here, as we are only interested in general trends in state estimate covariance such as those mentioned above.

Optimality of the inversion (3.9) is only with respect to the span of the weighting function set $F_{\mathbf{y}}$, which defines the search space. Fisher information is maximized by setting the span of $F_{\mathbf{y}}$ to $L^2(S^2, \mathbb{R}^2)$. In practice, inclusion of spherical harmonics up to $\sim$10th degree, constituting $M = 242$ independent weighting functions, provides sufficient span to achieve reasonable convergence to the global $L^2(S^2, \mathbb{R}^2)$ optimum. The only requirements imposed by (3.9) on the selection of the initial weighting set $F_{\mathbf{y}}$ are that it include $M \geq n$ linearly independent weighting patterns such that C is full rank. More patterns, especially orthogonal patterns, increase the span of the set, such that the static estimator is closer to the global optimum.

The reader is reminded that this is just the first stage in an offline process to determine optimal direct WFI mappings between sensors and actuators, $F_{\mathbf{u}}$ - a set

with just one weighting pattern per actuator, which can be implemented efficiently in real-time.

3.2.3 State Extraction Weighting Functions

If a more conventional architecture with explicit state feedback is desired, perhaps for the purpose of real-time gain modification, one can create a set of n weighting patterns that map optic flow to state estimates via n WFI operations. Consider relative state estimates $\hat{\mathbf{x}} = C^\dagger \tilde{\mathbf{y}}$, where $\tilde{\mathbf{y}} = \langle \dot{\mathbf{Q}}, \mathbf{F_y} \rangle$. If the inversion is pushed through the inner product, one obtains

$$\hat{x}_i = \left\langle \dot{\mathbf{Q}}, \sum_{j=1}^{M} C_{ij}^\dagger \mathbf{F}_{y_j} \right\rangle, \tag{3.19}$$

where the second argument in the inner product can be interpreted as the optimal extraction pattern for the ith state, $\mathbf{F}_{\hat{x}_i} = \sum_{j=1}^{M} C_{ij}^\dagger \mathbf{F}_{y_j}$. Hence, the optimal state extraction patterns (e.g., Fig. 4.16), are given by

$$F_{\hat{\mathbf{x}}} = C^\dagger F_{\mathbf{y}}, \tag{3.20}$$

and the WFI-based static state estimates can then be obtained via

$$\hat{x}_i = \langle \dot{\mathbf{Q}}, \mathbf{F}_{\hat{x}_i} \rangle. \tag{3.21}$$
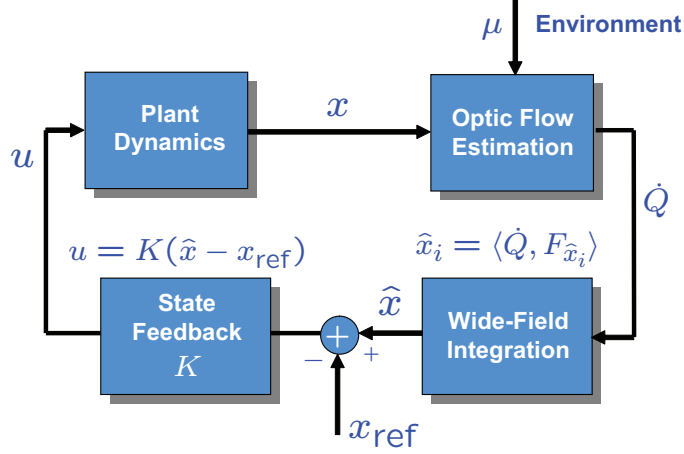
Figure 3.2: Equivalent closed-loop architecture with explicit state estimation; gained feedback of carefully selected WFI outputs

With state feedback $\mathbf{u} = K(\hat{\mathbf{x}} - \mathbf{x}_{\text{ref}})$ this revised architecture (Fig. 3.2) is still equivalent to the original control loops presented in Fig. 3.1.

3.3 Stage 2: Optimal Feedback Gains

If estimates of all states are available and intended for feedback, infinite horizon LQR [74] can be used (contingent on several conditions) to design a K that is optimal with respect to a state penalty matrix $J_{\mathbf{x}}$ and control penalty matrix $J_{\mathbf{u}}$. If this is not true, but the system is still stabilizable using measurable states, then output LQR techniques [71] can usually be employed. Optimality of state estimates (Stage 1) and feedback gains (Stage 2) are incorporated into the proposed real-time control law (3.1) by choice of WFI pattern set

$$F_{\mathbf{u}} = KC^{\dagger}F_{\mathbf{y}}. \tag{3.22}$$

This provides a robust, mathematically justified method for WFI weighting pattern design.

Chapter 4

Robotic Applications

In this chapter, planar-constrained WFI concepts proposed in [65, 67] are experimentally validated and stability is proven for large perturbations using nonlinear analysis. Subsequently, the WFI-based control architecture and weighting pattern design techniques from Chapter 3 are applied to demonstrate robust obstacle avoidance and terrain following on 6-DOF platforms.

4.1 1-D WFI Demonstrations

The original definition of the WFI framework [67] involved restriction of the measurement domain to a single ring of 1-D optic flow. This section describes the first experimental demonstrations of this using on-board optic flow measurements. For more detail on the controller derivation and description of hardware see [68] and [75].

4.1.1 Ground Robot using Ring-constrained WFI

4.1.1.1 WFI-Based Controller

The measurement domain is defined as a ring of azimuthal measurements in the yaw plane, therefore optic flow is modelled by the last expression in (2.4). In
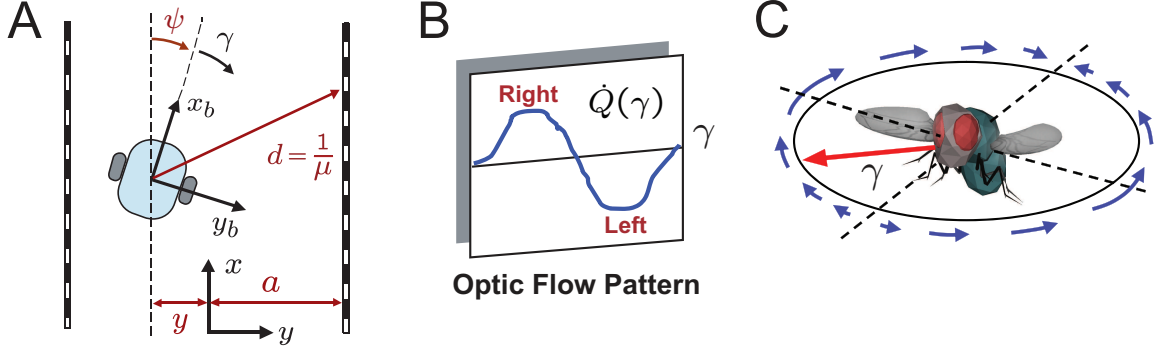
Figure 4.1: (A) Environment approximation with planar vehicle, (B) nominal 1D optic flow as function of viewing angle, (C) nominal equatorial optic flow field around insect in an infinite tunnel.

this case, the general WFI operator (2.17) simplifies to an inner product on

$$L_2[0, 2\pi] = \left\{ f : [0, 2\pi] \to \mathbb{R} : \int_0^{2\pi} |f(\gamma)|^2 \, d\gamma < \infty \right\} \tag{4.1}$$

with the weighting pattern also confined to the 1-D ring; i.e.

$$y_j = \langle \dot{Q}_Y^\gamma, F_{y_j,Y}^\gamma \rangle = \int_0^{2\pi} \dot{Q}_Y^\gamma \, F_{y_j} \, d\gamma. \tag{4.2}$$

With the assumption of $g \to \infty$ and $\theta = \phi = 0$, the generic environment model (2.10) simplifies to a planar tunnel (Fig. 4.1A) with yaw-plane nearness function given in Table 2.1. This is a local approximation of a vehicle navigating between two large obstacles. Fourier harmonics, orthogonal on $L_2[0, 2\pi]$, were selected for the trial set of weighting functions. WFI is performed offline using the closed-form optic flow model and the outputs are linearized about the nominal optic flow pattern, which corresponds to travel along the centerline. Inspection of the observation matrix C resulted in the choice of just three weighting functions for synthesizing

the feedback loop; $F_{a_1} = N \cos \gamma$ to extract relative orientation $\psi \frac{u_0}{a}$, $F_{a_2} = N \cos 2\gamma$ to extract lateral offset $y \frac{u_0}{a^2}$, and $F_{b_1} = N \sin \gamma$ to extract forward speed u/a. The term $N = \frac{1}{\pi}$ normalizes the weighting function such that an exact match to the observed optic flow results in unity output. Output feedback gains were applied to produce the control laws

$$
\begin{aligned}
u_r &= \langle \dot{Q}_Y^\gamma, F_{u_r,Y}^\gamma \rangle + u_{r,\text{ref}} \ d\gamma = \langle \dot{Q}_Y^\gamma, (K_1 \frac{1}{\pi} \cos \gamma + K_2 \frac{1}{\pi} \cos 2\gamma) \rangle \qquad (4.3) \\
u_{\dot{u}} &= \langle \dot{Q}_Y^\gamma, F_{u_{\dot{u}},Y}^\gamma \rangle + u_{\dot{u},\text{ref}} \ d\gamma = \langle \dot{Q}_Y^\gamma, K_3 \frac{1}{\pi} \sin \gamma \rangle - K_3 N u_{\text{ref}}.
\end{aligned}
$$

where $u_r = \dot{\psi}$ (commanded rotation rate), $u_{\dot{u}} = \dot{u}$ (commanded forward acceleration) and $N u_{\text{ref}}$ is the desired global optic flow rate for speed control. Note that this compensator does not apply the optimal weighting function design techniques of Chapter 3.

4.1.1.2   Nonlinear Stability Analysis

In [76], the feedback control law (4.3) was shown to provide local exponential stability of the centering response. It is now shown that it asymptotically stabilizes the equilibrium point $(y = 0, \psi = 0)$ of the nonlinear system over a large range of initial conditions.

Assuming a constant forward speed u_0 the nonlinear form of the measured WFI outputs are combined with the dynamics and control law to produce the following

closed loop nonlinear system:

$$\dot{y} = u_0 \sin \psi$$

$$\dot{\psi} = \langle \dot{Q}_Y^\gamma, F_{u_r,Y}^\gamma \rangle = K_1 \frac{4au_0 \sin \psi \cos \psi}{3\pi(a^2 - y^2)} - K_2 \frac{u_0 y \cos \psi}{2(a^2 - y^2)}, \tag{4.4}$$

which can be simplified by making the coordinate transform $z_1 = y/a$, $z_2 = \sin \psi$;

$$\dot{z}_1 = \frac{u_0}{a} z_2$$

$$\dot{z}_2 = K_1 \frac{4u_0(1 - z_2^2)}{3\pi a(1 - z_1^2)} z_2 - K_2 \frac{u_0(1 - z_2^2)}{2a(1 - z_1^2)} z_1. \tag{4.5}$$

The following candidate Lyapunov function

$$V(z_1, z_2) = \frac{1}{2u_0} z_2^2 - \frac{K_2}{4u_0} \ln (1 - z_1^2) \tag{4.6}$$

is chosen to evaluate the asymptotic stability of (4.5) on the domain $E : \{(z_1, z_2)| $ $z_2 \in (-1, 1), z_1 \in (-1, 1)\}$, which corresponds to the range of initial conditions $-a < y < a$ and $-\pi/2 < \psi < \pi/2$. $V(z_1, z_2)$ is positive definite if $K_2 > 0$.

The derivative along trajectories is given by

$$\dot{V} = \frac{(8K_1 - 8K_1 z_2^2 + 3\pi K_2 z_1 z_2)}{6\pi a(1 - z_1^2)} z_2^2, \tag{4.7}$$

which is zero for $z_2 = 0$ (defined as region R_1) or $z_1 = g(z_2)$, where $g(z_2) = \frac{8K_1(z_2^2 - 1)}{3\pi K_2 z_2}$. The expression $z_1 = g(z_2)$ defines a curve that partitions the domain E into several regions, as shown in Fig. 4.2A. Define the distance δ from this curve in E such that

48

$z_1 + \delta = g(z_2)$. Substituting $z_1 = g(z_2) - \delta$ in (4.7) yields

$$\dot{V} = -\frac{K_2 \delta}{2a(1 - z_1^2)} z_2^3. \tag{4.8}$$

Note that the quantity $(1 - z_1^2) > 0$ for all $(z_2, z_1) \in E$.

For an arbitrary point (z_2, z_1) in the region $R_2 = \{(z_2, z_1) \mid 0 < z_2 < 1, \ -1 < z_1 < \min(1, g(z_2))\}$, we have $\delta > 0$ (if $K_1 < 0$) and $z_2^3 > 0$, therefore $\dot{V} < 0$. Similarly for the region $R_3 = \{(z_2, z_1) \mid -1 < z_2 < 0, \ \max(-1, g(z_2)) < z_1 < 1\}$, we have $\delta < 0$ (if $K_1 < 0$) and $z_2^3 < 0$, therefore $\dot{V} < 0$ for arbitrary $(z_2, z_1) \in R_3$. Hence, $\dot{V} \leq 0$ on domain $D = R_1 \cup R_2 \cup R_3$.

Consider the region of D defined by $D' = \{(z_2, z_1) \mid V(z_1, z_2) < c\}$ where $c = \inf\{V(z_1, z_2) \mid z_1 = g(z_2)\}$. Within this subset, $\dot{V} = 0$ iff $z_2 = 0$, which implies $\dot{z}_1 = 0$, hence $z_1 = 0$ for all time. Therefore the largest invariant set is the origin and by Lasalle's principle the closed loop nonlinear system is asymptotically stable on D' if $K_1 < 0$ and $K_2 > 0$. Fig. 4.2 shows contour plots of V and $\dot{V}$ and illustrates how domain D' approaches E as K_2 becomes small and $|\frac{K_1}{K_2}|$ becomes large. The system is not necessarily unstable for initial conditions outside of D', but no Lyapunov function was found to prove asymptotic stability over the entire tunnel.

The limitation of this analysis is that it assumes a specific environment that is unchanging with time. In reality, this assumption will not hold, therefore Lasalle's principal will fail. However, experimental demonstrations in Section 4.1.1.3 show that centering stability is in fact maintained in time-varying environments.
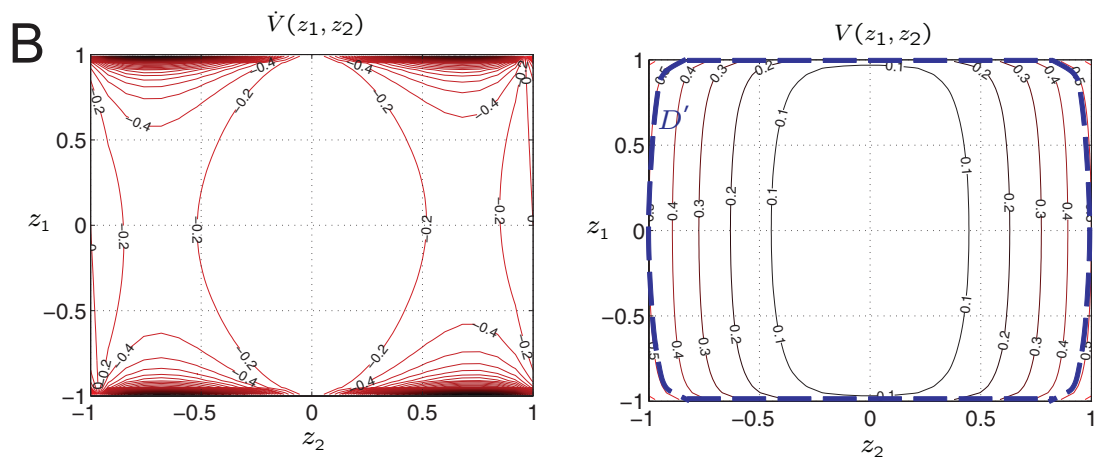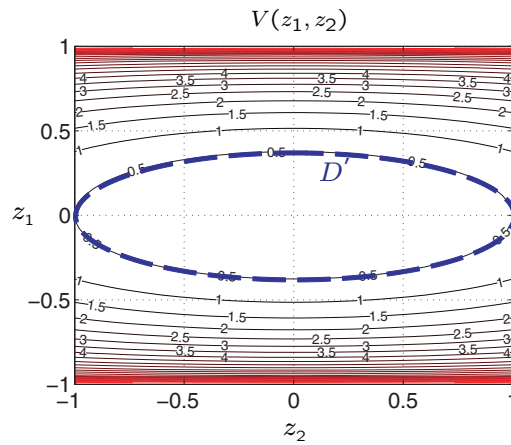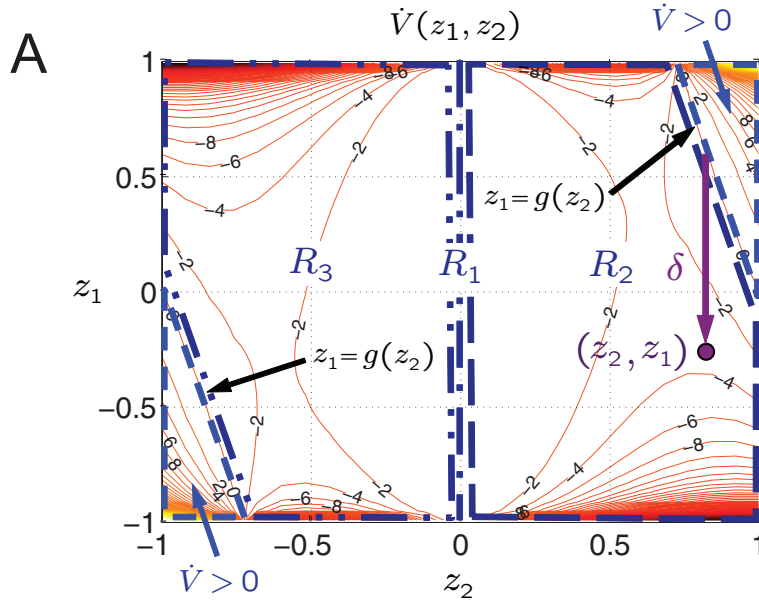
Figure 4.2: Contour plots of V and $\dot{V}$ and the regions $D = R_1 \cup R_2 \cup R_3$ (where $\dot{V} < 0$) and D' (for which asymptotic stability is guaranteed); (A) $K_1 = -24$, $K_2 = 13$ (gains used in 4.1.1.3), (B) $K_1 = -2.4$, $K_2 = 0.13$.
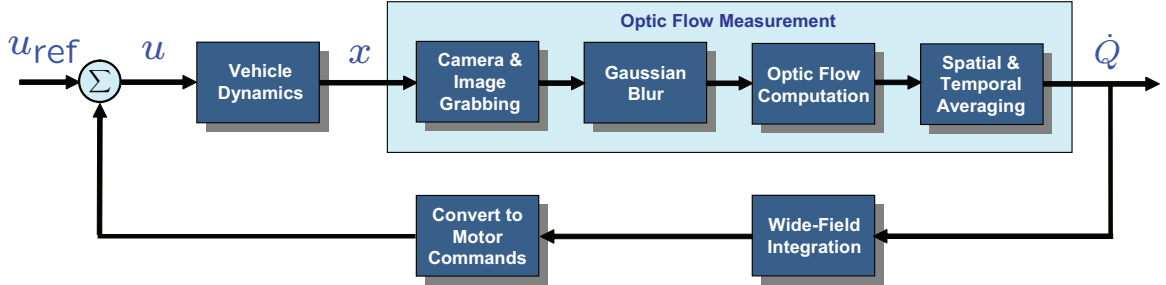
Figure 4.3: Information flow diagram for ground vehicle; $\mathbf{x} = (u, y, \psi)$, $\mathbf{u} = \{u_r, u_{\dot{u}}\}$, and $\mathbf{u}_{\text{ref}} = \{K_3 N u_{\text{ref}}, 0\}$.

4.1.1.3 Experimental Validation

To test the performance of the WFI-feedback concept on a real platform with real-time sampling of optic flow, a wheeled vehicle was constructed. A modified Dr. Robot X80 provided the chassis, wheel motors and motor control (Fig. 4.4A). A Biostar computer with VIA motherboard and AMD CPU (1.3 GHz) interfaces with the camera (FireFly MV, Point Grey Research), processes the imagery and sends motor commands at 20 Hz over the serial port. A 360° field of view is obtained from a parabolic mirror (0-360.com Panoramic Optic) installed above the robot, with the FireWire camera pointing upward toward the mirror (Fig. 4.4B). The author gratefully acknowledges Mike Chinn for design and assembly of the hardware. The walls of the corridor (Fig. 4.5A and 4.6A) are composed of the imagery shown in Fig. 4.4C.

Optic Flow Sensing and Computation

Fig. 4.3 illustrates the closed-loop process whereby the optic flow is measured by the vehicle and used to control its motion. As the robot travels forward through the tunnel, the camera is repeatedly accessed (240×240 resolution, 55 fps) by the on-board C++ routine. To reduce high frequency spatial noise, the image extracted
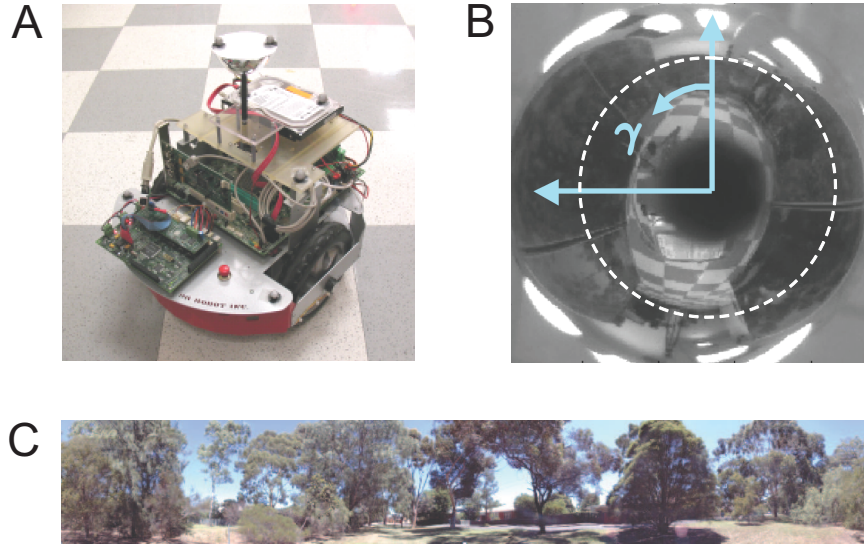
Figure 4.4: (A) Ground vehicle configuration, (B) Camera view with an example ring used for 1D optic flow extraction, and (C) Tunnel wall texture.

from the camera is first run through a low-pass spatial filter using an *OpenCV* Gaussian blurring function.

For each frame, the embedded software captures a greyscale image. Using two successive frames, optic flow is computed to determine the motion field around the azimuth of the vehicle. An *OpenCV* implementation of the Lucas-Kanade pyramid iterative algorithm [77] is used to compute the optic flow. This is a gradient-based method using a maximum of 20 iterations at each pyramid level (3 levels used here), and an initial guess of zero. The 'pyramid' scheme refers to the fact that optic flow is first computed for lower resolution versions of the images (to increase the maximum detectable shift), then this estimate is fed as an initial guess to the optic flow computation for a higher resolution version, and so forth, until the maximum resolution version is reached. Outlier solutions with high final cost function error, or estimated shift components larger than a given search space size, are disregarded.

To compute the azimuthal optic flow efficiently, the movement of a set of 800 target pixels is tracked, all located in one of four concentric rings of pixels at fixed radii from the mirror center (e.g., Fig. 4.4B). Each ring will capture a different line of approximately constant height on the corridor wall. Four rings, rather than one, are used to increase the number of measurements in the WFI thereby reducing noise throughput to the actuators. The optic flow computation is 2-D, but only the component of the shift tangent to the ring is used in the controller. By taking the dot product of the shift vector with the ring tangent vector, an estimate is obtained of the 1-D optic flow at 20 discrete angles around the vehicle. Each discrete measurement is the average of 40 adjacent raw measurements across four rings, with outlier measurements rejected. The optic flow for each frame combination can be further smoothed by taking the block average over a time interval (assuming constant optic flow during this period). The desired vehicle turn rate is computed via (4.3), then the wheel speeds are calculated and sent to the motor controller board.

Results

The vehicle's trajectory was tracked using a Vicon tracking system, which uses 8 cameras to triangulate the position of reflective markers attached to the vehicle. It updates at 350 Hz and is accurate to less than 1 mm.

The centering response behavior is tested in a fixed-width 1.2 m corridor with a 90° bend (Fig. 4.5A). The commanded forward speed is held constant for this experiment at 0.43 m/s using local feedback from the motor speed controllers. Input parameters include a turn saturation limit of 1 rad/s, and gains of $K_1 = -24$, $K_2 = 13$. These gains were manually optimized to achieve rapid centering but with
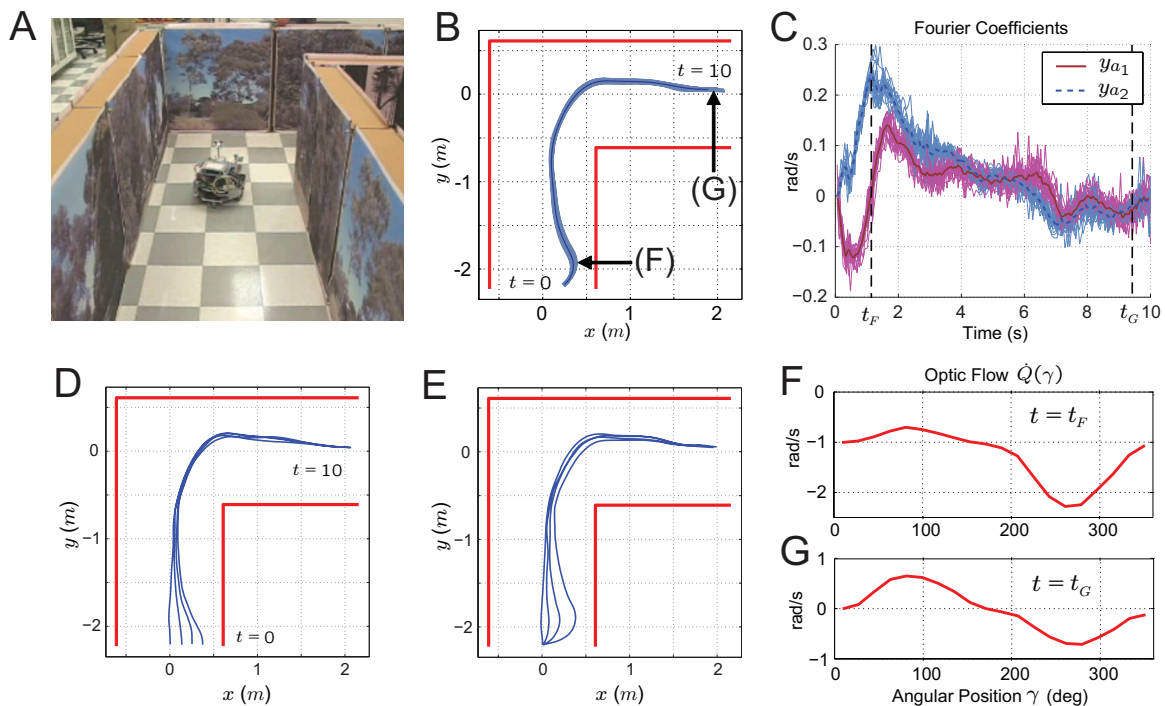
Figure 4.5: Centering response in a 90° corridor for a fixed forward speed; (A) ground vehicle and wall textures, (B) trajectories (and mean) for 20 trials with a combined 0.25 m lateral and 45° orientation offset, (C) first y_{a_1} and second y_{a_2} cosine harmonics (WFI outputs), and means, for the 20 trials, (D) trajectories for different initial lateral offsets (0, 5, 10, 15 in.) and (E) orientation offsets (0°, 30°, 60°, 80°), (F) optic flow pattern $\dot{Q}(\gamma)$ measured at time $t = t_F$ and (G) at $t = t_G$.

minimal overshoot and noise response. The turn saturation limit is imposed to avoid undesirably large responses to noise in the y_{a_1} and y_{a_2} signals.

Examples of measured optic flow are shown in Fig. 4.5G, for a near-centered path of travel, and Fig. 4.5F, where there is clear asymmetry in the signal due to the lateral offset and a DC component due to the high turn rate of the vehicle. The optic flow has surprisingly little noise, even in the presence of local areas of poor contrast in the wall textures and in the front and back of the vehicle where there is no visual texture. Additional irregularities in the sinusoid shape arise due to distortions in the mapping of straight lines to concentric rings on the mirror, vibrations in the robot chassis, reflections on the Plexiglas mirror mounting window, and camera noise. The resulting variance in the trajectories in the figure shows that the approach can robustly handle such non-idealities.

The initial lateral and orientation perturbations are evident in the y_{a_1} and y_{a_2} plots (Fig. 4.5C) and the controller is able to effectively regulate these to zero plus or minus a finite tolerance due to measurement noise. The robustness of the method is illustrated in Fig. 4.5B, which shows consistent trajectories (max standard deviation 2.0 cm) for 20 trials, and Fig. 4.5D-E, which partially validate the findings of 4.1.1.2 by demonstrating stability for large initial perturbations.

The clutter and centering responses were tested simultaneously using a converging-diverging tunnel with a 0.76 m throat. Forward speed control is implemented by a discrete-time controller which adds $K_3(Nu_{\text{ref}} - y_{b_1})$ to the previous speed at every control update. The maximum turn rate is scaled linearly downward from 1 rad/s at 0.43 m/s (max speed) to 0.26 rad/s at 0.22 m/s (min speed) to avoid over-active
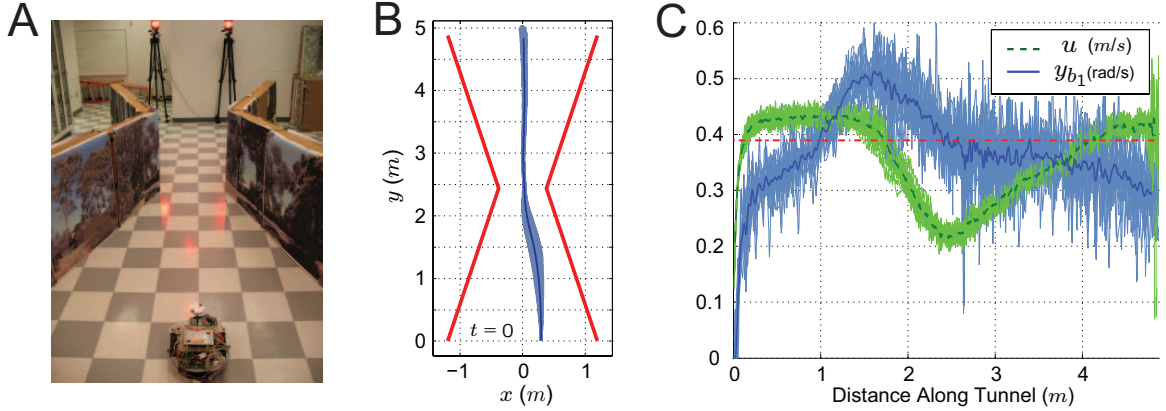
Figure 4.6: Clutter response for 20 trials; (A) converging-diverging tunnel environment, (B) trajectories and mean, (C) forward speed u and first sine harmonic y_{b_1} (WFI output) as a function of tunnel position for the 20 trials along with the mean.

control in the low bandwidth regime. This is also the reason for using lower gains here ($K_1 = -2.4$, $K_2 = 1.3$ and $K_3 = 3.8$), compared with the constant speed trials.

Fig. 4.6 shows that the centerline of the corridor is tracked well and the speed is regulated to keep the first sine harmonic y_{b_1} of optic flow roughly constant at $Nu_{\text{ref}} = 0.39$. The orientation offset during recovery to the centerline causes a deceptively low y_{b_1} value due to nonlinearities in the y_{b_1} expression (see [68]). When the orientation offset is corrected, y_{b_1} shoots up and the controller acts to control the forward speed. The proportionality between velocity and corridor width is evident in the latter half of the trajectory where the robot remains centered. These results emulate the behavior seen in experiments with honeybees [26].

4.1.1.4 Optimal Weighting Functions for Planar Vehicles with a Nonholonomic Sideslip Constraint

In [68], weighting functions that delivered static state estimates via a planar WFI operation were found by trying Fourier harmonics and selecting appropriate

harmonics by inspection of the observation matrix C. Here, the method of Section 3.2.3 will be employed to obtain optimal weighting functions.

The infinite tunnel model is again assumed, and because parametric environment uncertainty (in the tunnel width) changes only the scaling of the 2-D environment, not the relative structure (as typically occurs in 3-D), the uncertainty in C is neglected. The minimum variance estimator then results from filling the initial weighting set $\mathbf{F_y}$ with all the elements of an infinite basis for $L_2[0, 2\pi]$, determining C using the algebraic optic flow model, and applying (3.9) and (3.20). A close approximation is obtained by including Fourier harmonics in $\mathbf{F_y}$ up to $\sim$20th order, but the exact optimum can also be obtained in a more efficient manner. If the optic flow model is linearized about a desired pattern and the resulting state coefficients are used as weighting functions $\mathbf{F_y}$, then the Fisher information is maximized with respect to the model and (3.9) and (3.20) deliver the optimum (minimum variance) state extraction weighting functions. In more detail:

1. Linearize $\dot{Q}$ (sideslip neglected) about the nominal trajectory:

$$
\dot{Q}_{\text{lin}} = \begin{cases} y\frac{v_0 \sin^2\gamma}{a^2} + \psi\frac{v_0 \sin 2\gamma}{2a} + u\frac{\sin^2\gamma}{a} - \dot{\psi}, & 0 \le \gamma + \psi < \pi \\[2mm] y\frac{v_0 \sin^2\gamma}{a^2} - \psi\frac{v_0 \sin 2\gamma}{2a} - u\frac{\sin^2\gamma}{a} - \dot{\psi}, & \pi \le \gamma + \psi < 2\pi \end{cases} \tag{4.9}
$$

2. Set $F_{y_i} = \frac{\partial \dot{Q}_{\text{lin}}}{\partial x_i}$ and perform WFI of $\dot{Q}_{lin}$. Note that this gives the same result as using the non-linear $\dot{Q}$ and linearizing the WFI outputs (see Section A.1).

$$
y_i = \int_0^{2\pi} \dot{Q}_{\text{lin}} \frac{\partial \dot{Q}_{\text{lin}}}{\partial x_i} \, d\gamma. \tag{4.10}
$$

57

3. Collate results into an observation matrix C:

$$
\begin{pmatrix} y_1 \\ y_2 \\ y_3 \\ y_4 \end{pmatrix} = \begin{pmatrix} \frac{3\pi v_0^2}{4a^4} & 0 & 0 & -\frac{\pi v_0}{a^2} \\ 0 & \frac{\pi v_0^2}{4a^2} & 0 & 0 \\ 0 & 0 & \frac{3\pi}{4a^2} & 0 \\ -\frac{\pi v_0}{a^2} & 0 & 0 & 2\pi \end{pmatrix} \begin{pmatrix} y \\ \psi \\ u \\ \dot{\psi} \end{pmatrix}.
\tag{4.11}
$$

4. Since $m = n$, the system is exactly determined and the optimum weighting functions for static state extraction are defined by the vector of functions $\mathbf{F_x} = C^{-1}\mathbf{F_y}$. The function $\frac{\partial \dot{Q}_{\text{lin}}}{\partial x_i}$ represents a perturbation pattern that is imposed on the nominal flow pattern when state x_i becomes non-zero. Since these are not necessarily orthogonal, the inversion step (3.20) is required to isolate the effect of each state.

$$
\begin{aligned}
F_y &= -\frac{2a^2}{\pi v_0}\cos 2\gamma \\[2mm]
F_\psi &= \begin{cases} \frac{2a}{\pi v_0}\sin 2\gamma, & 0 \le \gamma < \pi \\[2mm] -\frac{2a}{\pi v_0}\sin 2\gamma, & \pi \le \gamma < 2\pi \end{cases} \\[2mm]
F_u &= \begin{cases} \frac{4a}{3\pi}\sin^2\gamma, & 0 \le \gamma < \pi \\[2mm] -\frac{4a}{3\pi}\sin^2\gamma, & \pi \le \gamma < 2\pi \end{cases} \\[2mm]
F_{\dot{\psi}} &= -\frac{1}{2\pi}\left(1 + 2\cos 2\gamma\right).
\end{aligned}
\tag{4.12}
$$

The choice of $\mathbf{F_y}$ as the Jacobian of the optic flow model results in the same Fisher information as an $\mathbf{F_y}$ that fully spans $L_2[0, 2\pi]$ because the span of $\mathbf{F_y}$ here is iden-

tical to the span of the optic flow model. Therefore, the observation set delivers as much information as possible about the model. Any additional observations (weighting functions) are redundant and therefore do not increase the Fisher information. Compared with the Fourier set $\mathbf{F_y} = \{F_{a_0}, F_{a_1}, F_{a_2}, F_{b_1}\}$ employed in past WFI studies [65, 67], the optimum functions in (4.12) will provide state estimates with a modest 3% reduction in variance; hence the Fourier choice was close to optimum.

4.1.2 Quadrotor using Ring-constrained WFI

This section summarizes the outcome of a WFI experiment using a micro quadrotor (Fig. 4.7), the short comings of which provide motivation for the 2-D WFI techniques described in Section 4.2. To demonstrate WFI-based navigation on a 6-DOF platform, the 1-D sensing methodology of 4.1.1 was utilized, along with sonar-based altitude regulation to maintain near-planar flight. The quadrotor vehicle was fully autonomous, with all vision hardware onboard. A panoramic mirror and camera were used for y and ψ estimation and a downward pointing Centeye sensor provided estimates of u and v, after subtracting off rotation components q and p using gyro data. The author gratefully acknowledges Joe Conroy and Greg Gremillion for the hardware design, assembly and test, and Badri Ranganathan for integration of my floating point WFI software on to the fixed point processor. The reader is referred to [75] for vehicle details and experimental results.

The experiment successfully demonstrated simple corridor navigation, but significant trajectory variance occurred due to errors in the estimation of forward speed and sideslip from the downward-pointing optic flow sensor, which exhibited extreme
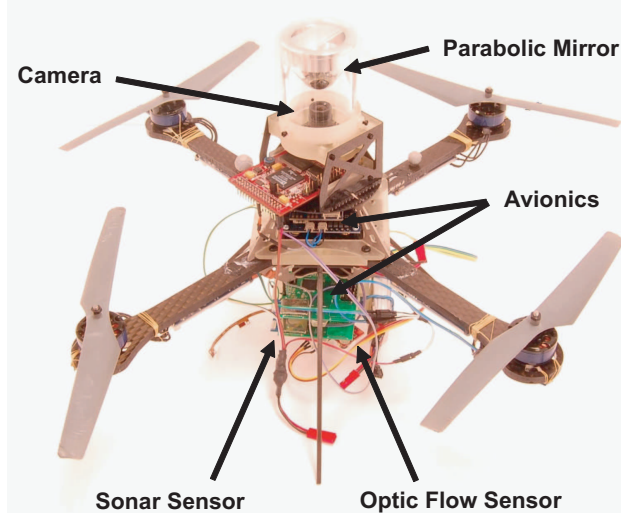
Figure 4.7: Schematic diagram of quadrotor components.

texture dependence. Differing frequency response characteristics between the Centeye sensor and the gyros further compounded u and v measurement anomalies. This motivates the need for spherical WFI of optic flow over a larger field of view, with optimal weighting patterns. Such a scheme should deliver more reliable state estimates, without the need to fuse-in gyro data.

The derivation of the optimal WFI weighting functions (4.1.1.4) used in this experiment required that sideslip be neglected to maintain a full rank C matrix. When optic flow is measured only in an equatorial ring, the perturbation pattern induced by an orientation offset ψ is exactly opposite to that induced by sideslip v, hence these quantities cannot be distinguished from one another (e.g., Eq. (5.1)). The differing signs also imply that stabilizing feedback of $\hat{\psi}$ (obtained from equatorial ring WFI) will destabilize the v dynamics. Although this is countered somewhat by sideslip regulation from the Centeye sensor, the limited bandwidth of this feedback loop prevent the use of large feedback gains on the $\hat{\psi}$ signal. This constrains

60
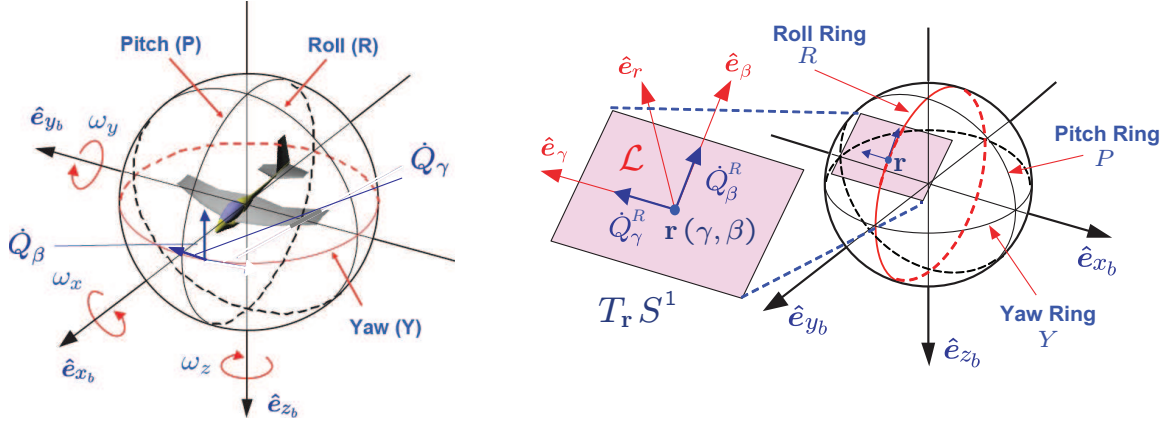
Figure 4.8: Fixed-wing UAV with ring-constrained optic flow sensing.

the performance of the system, preventing it from navigating the tight bends demonstrated in 4.1.1.3. Spherical WFI over a wider field of view would allow the coupled quantities to be separated (as is demonstrated in 4.2.2), thus removing the gain limitation.

4.2   2-D WFI Demonstrations

4.2.1   Fixed-Wing UAV using Ring-constrained WFI

In this section, the gap between planar 1-D WFI and full spherical 2-D WFI is bridged by considering 2-D optic flow measured in three orthogonal planes (Fig. 4.8). This allows extraction of all relevant navigational and motion states for a 6-DOF vehicle with vision sensing required over a relatively small percentage of the sphere. This estimation methodology will be applied to the task of fixed-wing UAV navigation in a simplified urban environment.

4.2.1.1 WFI-Based Controller

With the optic flow measurements constrained to three orthogonal planes (yaw, pitch, roll), see (2.4), the general WFI operation (2.17) simplifies to

$$
\begin{aligned}
y_{i,j}^{k}(\mathbf{x}) &= \langle \dot{Q}_{j}^{k}, F_i \rangle = \int_{0}^{2\pi} \dot{Q}_{j}^{k}(\beta, \mathbf{x})\, F_i(\beta)\, d\beta \quad \text{(for } R \text{ and } P \text{ planes)}, \\
y_{i,j}^{Y}(\mathbf{x}) &= \langle \dot{Q}_{j}^{Y}, F_i \rangle = \int_{0}^{2\pi} \dot{Q}_{j}^{Y}(\gamma, \mathbf{x})\, F_i(\gamma)\, d\gamma \quad \text{(for } Y \text{ plane)}, \quad (4.13)
\end{aligned}
$$

where i is the output number, j is the is the plane of interest and k is the direction of flow under scrutiny - either the β or γ direction.

In each plane, Fourier harmonics up to 2nd order were used for the initial weighting function set $\mathbf{F_y}$, and the flat surface world (2.10) was assumed for the optic flow model, with no roof ($h_U \to \infty$) and no front/rear surfaces ($g \to \infty$); see Table 2.1 for the planar distance functions. The resulting C matrices for the limiting cases of the parameterized environment are presented in Table 4.1, and are cropped to display just n outputs, considered to provide the most consistent measurements of each state given the environment uncertainty. Note that pitch ring optic flow provides the most reliable measurements in this respect because all the uncertainty is in the lateral obstacle environment and not the longitudinal.

To account for the uncertainty in C, an inversion matrix $C^{\dagger}$ was manually designed; presented in Table 4.3 (2nd column) in condensed form. In its construction, a harmonic was used to decouple another harmonic (that encoded multiple states) only if the states encoded by the first harmonic were consistent across the environ-

62

Table 4.1: Linearized 3-Ring optic flow decomposition for baseline environments

WFI Output	Floor	Right-side Wall with Floor	Tunnel with Floor
$y_{b_1,R}^{\beta}$	$\frac{2}{3\pi h}w$	$\frac{1}{3\pi f_1}v + \frac{2hf_1+2h^2+af_1+a^2}{3\pi haf_1}w$	$\frac{2(a^2+2hf_1+2h^2)}{3\pi haf_1}w$
$y_{b_2,R}^{\gamma}$	$\frac{4u_{\text{ref}}}{3\pi h}\phi$	$-\frac{2}{3\pi f_1}u - f_2\phi - \frac{2hu_{\text{ref}}}{3\pi f_1^2 f_1}z - \frac{2au_{\text{ref}}}{3\pi f_1^2 f_1}y$	$-f_3\phi - \frac{4u_{\text{ref}}a}{3\pi f_1^2 f_1}y$
$y_{a_1,P}^{\beta}$	$-\frac{4u_{\text{ref}}}{3\pi h^2}z - \frac{4}{3\pi h}u$	$-\frac{4u_{\text{ref}}}{3\pi h^2}z - \frac{4}{3\pi h}u$	$-\frac{4u_{\text{ref}}}{3\pi h^2}z - \frac{4}{3\pi h}u$
$y_{b_1,P}^{\beta}$	$\frac{2u_{\text{ref}}}{3\pi h}\theta + \frac{2}{3\pi h}w$	$\frac{2u_{\text{ref}}}{3\pi h}\theta + \frac{2}{3\pi h}w$	$\frac{2u_{\text{ref}}}{3\pi h}\theta + \frac{2}{3\pi h}w$
$y_{a_0,P}^{\gamma}$	$-\frac{\sqrt{2}}{\pi h}v$	$-\frac{\sqrt{2}}{\pi h}v$	$-\frac{\sqrt{2}}{\pi h}v$
$y_{a_1,P}^{\gamma}$	$-\frac{1}{2h}v + p$	$-\frac{1}{2h}v + p$	$-\frac{1}{2h}v + p$
$y_{b_1,P}^{\gamma}$	$-r$	$-r$	$-r$
$y_{a_1,Y}^{\beta}$	$-q$	$-q$	$-q$
$y_{a_1,Y}^{\gamma}$	0	$\frac{2u_{\text{ref}}}{3\pi a}\psi - \frac{2}{3\pi a}v$	$\frac{4u_{\text{ref}}}{3\pi a}\psi - \frac{4}{3\pi a}v$
$y_{a_2,Y}^{\gamma}$	0	$-\frac{u_{\text{ref}}}{4a^2}y - \frac{1}{4a}u$	$-\frac{u_{\text{ref}}}{2a^2}y$
$y_{b_1,Y}^{\gamma}$	0	$\frac{4u_{\text{ref}}}{3\pi a^2}y + \frac{4}{3\pi a}u$	$\frac{8}{3\pi a}u$
note:	$f_1 = \sqrt{h^2 + a^2}$	$f_2 = \frac{2(h^2+hf_1-af_1-a^2)u_{\text{ref}}}{3\pi haf_1}$	$f_3 = \frac{4(h^2+hf_1-a^2)u_{\text{ref}}}{3\pi ahf_1}$

ment extremes and the decoupling did not depend on knowledge of environment parameter a. For these reasons, it was assumed that independent measurements of u and ϕ are available. Note that this assumption could be avoided through use of the more rigorous methods of Section 3.2, which will be demonstrated in 4.2.2.

The dynamics of the vehicle (4.14) are taken from a low-speed fixed wing UAV; the 4.5 kg *Gap 65* [78] with 1.8 m wingspan. Aerodynamic and gravity forces are linearized about the steady, wings-level flight condition with a forward speed of u_0=12.5 m/s. For simulation, the linearized forces are implemented in a non-linear

dynamics and kinematics engine.

$$\dot{u} = -g\theta + \frac{X_u}{m}(u - u_0) + \frac{X_w}{m}w + \frac{1}{m}\delta_T - qw + rv$$

$$\dot{v} = g\phi + \frac{Y_v}{m}v + \frac{Y_p}{m}p + \frac{Y_r}{m}r + \frac{Y_{\delta_a}}{m}\delta_a + \frac{Y_{\delta_r}}{m}\delta_r - ru + pw$$

$$\dot{w} = \frac{Z_u}{m}(u - u_0) + \frac{Z_w}{m}w + \frac{Z_q}{m}q + \frac{Z_{\delta_e}}{m}\delta_e - pv + qu$$

$$\dot{p} = \left(\frac{L_v}{I_{xx}} + \frac{N_v}{f_4}\right)v + \left(\frac{L_p}{I_{xx}} + \frac{N_p}{f_4}\right)p + \left(\frac{L_r}{I_{xx}} + \frac{N_r}{f_4}\right)r + \left(\frac{L_{\delta_a}}{I_{xx}} + \frac{N_{\delta_a}}{f_4}\right)\delta_a$$
$$\quad + \left(\frac{L_{\delta_r}}{I_{xx}} + \frac{N_{\delta_r}}{f_4}\right)\delta_r + \dot{p}_{nl}$$

$$\dot{q} = \frac{M_w}{I_{yy}}w + \frac{M_q}{I_{yy}}q + \frac{M_{\delta_e}}{I_{yy}}\delta_e + \dot{q}_{nl} \tag{4.14}$$

$$\dot{r} = \left(\frac{N_v}{I_{zz}} + \frac{L_v}{f_4}\right)v + \left(\frac{N_p}{I_{zz}} + \frac{L_p}{f_4}\right)p + \left(\frac{N_r}{I_{zz}} + \frac{L_r}{f_4}\right)r + \left(\frac{N_{\delta_a}}{I_{zz}} + \frac{L_{\delta_a}}{f_4}\right)\delta_a$$
$$\quad + \left(\frac{N_{\delta_r}}{I_{zz}} + \frac{L_{\delta_r}}{f_4}\right)\delta_r + \dot{r}_{nl}$$

$$f_4 = \frac{I_{xx}I_{zz} - I_{xz}^2}{I_{xz}}$$

$$\begin{bmatrix} \dot{p}_{nl} \\ \dot{q}_{nl} \\ \dot{r}_{nl} \end{bmatrix} = [I]^{-1}\left(\begin{bmatrix} p \\ q \\ r \end{bmatrix} \times [I]\begin{bmatrix} p \\ q \\ r \end{bmatrix}\right).$$

Actuator saturation limits are: $|\delta_r| \leq 0.5$ rad, $|\delta_T| \leq \pm 5.3$ N, $|\delta_e| \leq 0.35$ rad and $|\delta_a| \leq 0.35$ rad. Characteristic stability quantities are defined in Table 4.2 with SI units and all symbols having their usual meaning.

The control strategy consists of an inner tracking loop $\mathbf{u} = K(\hat{\mathbf{x}} - \mathbf{x}_{ref})$ and an outer trajectory generation loop for lateral steering $\phi_{ref} = K_{\phi_{ref},y}(\hat{y} - y_{ref}) + K_{\phi_{ref},\psi}\hat{\psi}$, turn coordination and altitude measurement correction at high bank. The dynamic reference trajectory is presented in Table 4.3. Environment parameters are set to

Table 4.2: Fixed-wing UAV stability characteristics

Physical Parameters	Longitudinal Derivatives	Lateral Derivatives
$m = 4.50$	$X_u = -0.84$	$Y_v = -3.87$
$g = 9.81$	$X_w = 0.20$	$Y_p = 0.51$
$I_{xx} = 0.16$	$Z_u = -0.94$	$Y_r = 1.39$
$I_{yy} = 0.60$	$Z_w = -22.66$	$Y_{\delta_a} = -1.16$
$I_{zz} = 0.66$	$Z_q = -7.80$	$Y_{\delta_r} = 7.96$
$I_{xz} = 0.01$	$Z_{\delta_e} = -29.61$	$L_v = -0.40$
	$M_w = -0.94$	$L_p = -2.99$
	$M_q = -3.26$	$L_r = 0.66$
	$M_{\delta_e} = -21.89$	$L_{\delta_a} = 26.90$
		$L_{\delta_r} = 0.52$
		$N_v = 1.24$
		$N_p = -0.32$
		$N_r = -1.15$
		$N_{\delta_a} = 1.76$
		$N_{\delta_r} = -6.77$

$h = 10$ m and $\hat{a} = 8$. The latter is a rough pre-flight estimate of the tunnel half-width or lateral distance to an obstacle, which acts only to scale the y and ψ navigational gains.

The elevator and aileron control laws can therefore be written as

$$
\begin{aligned}
\delta_e &= K_{\delta_e,u}(u - u_{\text{ref}}) + K_{\delta_e,w}\left(\frac{3\pi h}{2}y^\beta_{b_1,R}\right) + K_{\delta_e,q}(-y^\beta_{a_1,Y} - q_{\text{ref}}) + K_{\delta_e,\theta}\left(\frac{3\pi h}{2u_{\text{ref}}}y^\beta_{b_1,P}\right) \\
&\quad + K_{\delta_e,z}\left(-\frac{h}{4u_{\text{ref}}}(3\pi h y^\beta_{a_1,P} + 4u) - z_{\text{ref}}\right) \\
\delta_a &= K_{\delta_a,v}\left(-\frac{\pi h}{\sqrt{2}}y^\gamma_{a_0,P}\right) + K_{\delta_a,p}\left(y^\gamma_{a_1,P} - \frac{\pi\sqrt{2}}{4}y^\gamma_{a_0,P}\right) + K_{\delta_a,r}(-y^\gamma_{b_1,P} - r_{\text{ref}}) \\
&\quad + K_{\delta_a,\phi}(\phi - \phi_{\text{ref}}).
\end{aligned}
\tag{4.15}
$$

The feedback for the engine thrust and rudder control are the same as above,

Table 4.3: Inversion of Fourier outputs (to obtain static state estimates) and desired trajectory

State	Estimation Law	Desired (Reference) State Value
y	$-\frac{2\hat{a}^2}{u_{\text{ref}}}y^\gamma_{a_2,Y}$	0
z	$-\frac{h}{4u_{\text{ref}}}(3\pi h y^\beta_{a_1,P}+4u)$	$h(\cos\phi-1)$
ϕ	ϕ	$K_{\phi_{\text{ref}},y}\left(-\frac{2\hat{a}^2}{u_{\text{ref}}}y^\gamma_{a_2,Y}-y_{\text{ref}}\right)+K_{\phi_{\text{ref}},\psi}\left(\frac{3\pi\hat{a}}{4u_{\text{ref}}}y^\gamma_{a_1,Y}-\psi_{\text{ref}}\right)$
θ	$\frac{3\pi h}{2u_{\text{ref}}}y^\beta_{b_1,P}$	0
ψ	$\frac{3\pi\hat{a}}{4u_{\text{ref}}}y^\gamma_{a_1,Y}$	0
u	u	u_0
v	$-\frac{\pi h}{\sqrt{2}}y^\gamma_{a_0,P}$	0
w	$\frac{3\pi h}{2}y^\beta_{b_1,R}$	0
p	$y^\gamma_{a_1,P}-\frac{\pi\sqrt{2}}{4}y^\gamma_{a_0,P}$	0
q	$-y^\beta_{a_1,Y}$	$\frac{9.81}{u}\sin\phi\tan\phi$
r	$-y^\gamma_{b_1,P}$	$\frac{9.81}{u}\sin\phi$

with subscripts adjusted. State-feedback LQR is employed to obtain a set of optimal feedback gains. After iteration with the simulator, the LQR control penalty matrix was set to $J_{\mathbf{u}}=\text{diag}(300,10^{-2},60,180)$ and the state penalty matrix to $J_{\mathbf{x}}=\text{diag}(10^{-20},20,120,1,\ 10^{-20},2,25,1,1,180,60)$. Outer-loop gains were determined via manual tuning. Table 4.4 lists the final gains.

Table 4.4: Fixed-wing UAV feedback gains

Elevator	Thrust	Aileron	Rudder	Roll Angle
$K_{\delta_e,z}=-0.26$	$K_{\delta_T,z}=5.07$	$K_{\delta_a,\phi}=-1.74$	$K_{\delta_r,\phi}=-0.27$	$K_{\phi_{\text{ref}},y}=-0.10$
$K_{\delta_e,\theta}=2.94$	$K_{\delta_T,\theta}=-16.03$	$K_{\delta_a,v}=-0.19$	$K_{\delta_r,v}=-0.18$	$K_{\phi_{\text{ref}},\psi}=-1.80$
$K_{\delta_e,u}=0.00$	$K_{\delta_T,u}=-13.46$	$K_{\delta_a,p}=-0.12$	$K_{\delta_r,p}=-0.03$	
$K_{\delta_e,w}=-0.08$	$K_{\delta_T,w}=1.97$	$K_{\delta_a,r}=0.28$	$K_{\delta_r,r}=0.64$	
$K_{\delta_e,q}=0.71$	$K_{\delta_T,q}=-0.23$			

4.2.1.2 Stability and Robustness Analysis

To evaluate robustness with respect to environment, we seek to determine if the closed-loop system is small-perturbation stable over all possible environments covered by the flat-surface world model. For this purpose, an observation equation is formed describing the linearized information contained in the state estimates $\hat{\mathbf{x}} = C_{\hat{\mathbf{x}}}\mathbf{x} = C^{\dagger}C\mathbf{x}$, where $C_{\hat{\mathbf{x}}} \neq I$. The linearized closed loop system can be written as

$$
\begin{aligned}
\dot{\mathbf{x}} &= A(\mathbf{x} - \mathbf{x}_0) + BK(\hat{\mathbf{x}} - \mathbf{x}_{\text{ref}}) \qquad\qquad (4.16)\\
&= (A + BK(C_{\hat{\mathbf{x}}} + K_{\mathbf{x}_{\text{ref}}}C_{\hat{\mathbf{x}}}))\mathbf{x} - (A + BK)\mathbf{x}_0,
\end{aligned}
$$

where $K_{\mathbf{x}_{\text{ref}}}$ is the linearized feedback gain matrix that links the current state measurements to the desired reference trajectory $\mathbf{x}_{\text{ref}} = K_{\mathbf{x}_{\text{ref}}}\hat{\mathbf{x}} + \mathbf{x}_0$. Closed-loop stability is determined by ensuring that the eigenvalues of $A + BK(C_{\hat{\mathbf{x}}} + K_{\mathbf{x}_{\text{ref}}}C_{\hat{\mathbf{x}}})$ lie in the open left half plane. From numerical eigenvalue analysis (see Fig. 4.9) it is found that the linearized system is indeed closed-loop stable for the entire environment parameter range (i.e., single obstacle close-by through to obstacles on both sides through to no obstacles). The system becomes unstable in narrow tunnels ($a < 4$ m) but this could be easily solved by reducing the lateral orientation gain relative to the side slip gain, with a damping-reduction penalty in more sparse environments.
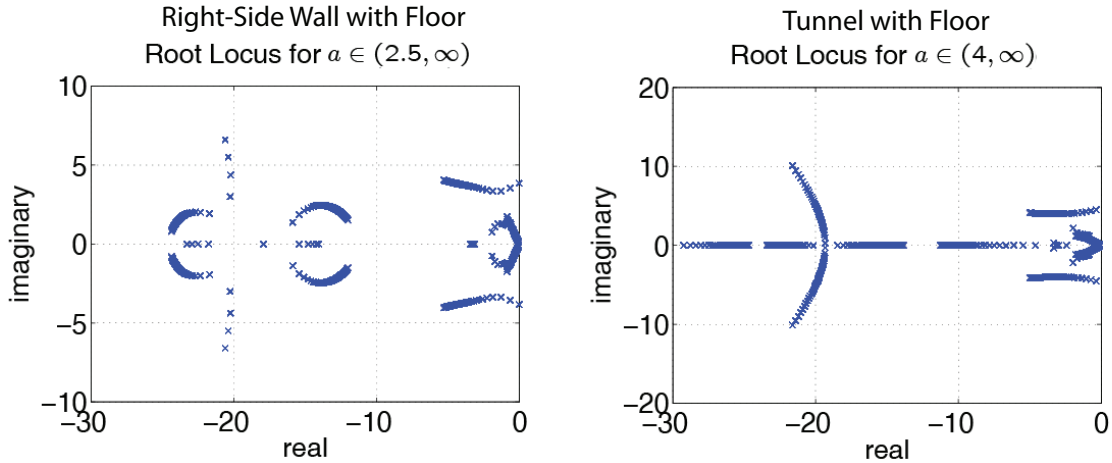
Figure 4.9: Root locus diagrams for range of environments and obstacle spacings. Closed-loop eigenvalues computed for a up to 1000 m ($\sim \infty$) in steps of 0.5 m. A 'no obstacles' environment is obtained when $a \to \infty$.

4.2.1.3 Simulation

The WFI-based state estimates provide adequate information to stabilize and navigate with the linearized vehicle model, but we must verify performance in the face of measurement noise, nonlinearities (Eq. (4.14)) and differences between the true environment and its mathematical approximation. For this purpose, a virtual UAV was simulated in two different environments using an in-house simulation engine (AVLSim). Environment A (Fig. 4.10A) simulates the 'right side-wall with floor' scenario, whilst environment B (Fig. 4.10B) simulates a 'tunnel with floor' world and has the additional challenges of a 20° terrain ramp and a 30° bend in the 16 m wide tunnel.

Optic Flow Sensing and Computation

AVLSim provides visualization capabilities as well as the ability to compute optic flow from simulated cameras. The virtual UAV is installed with six cameras,
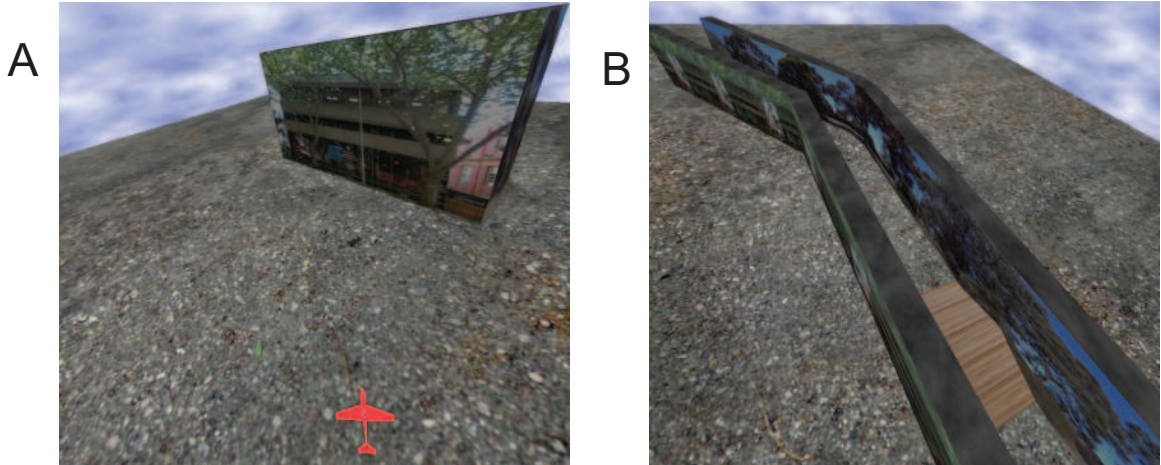
Figure 4.10: 3-D simulation environments; (A) single wall, (B) tunnel with 20° ramp and 30° bend.

each with a 90° × 90° field-of-view and a resolution of 128 × 128 pixels. The cameras cover the six sides of a cube such that the three orthogonal measurement rings are fully imaged. The imagery is first passed through a Gaussian blurring function to reduce high frequency spatial noise. Images are combined to form a 360° panorama for each ring, and optic flow is computed with a resolution-iterative implementation of the Lucas-Kanade algorithm at 30 fps for 1600 image points per panorama. The environment surfaces and sky are textured with imagery of sufficient visual contrast so that optic flow can be computed.

The optic flow measurement nodes are located in one of four rows, around the mid-line of the panoramic image, with a vertical separation of 4 pixels (i.e., max out-of-plane angle = 5°). The measurement points (Fig. 4.11) have equal azimuthal spacing and are assigned to pixel coordinates by projecting points on a circle to a flat camera surface. Shift estimate magnitude is also corrected for flat-camera distortion. Measurements are averaged horizontally to converge 400 data points to
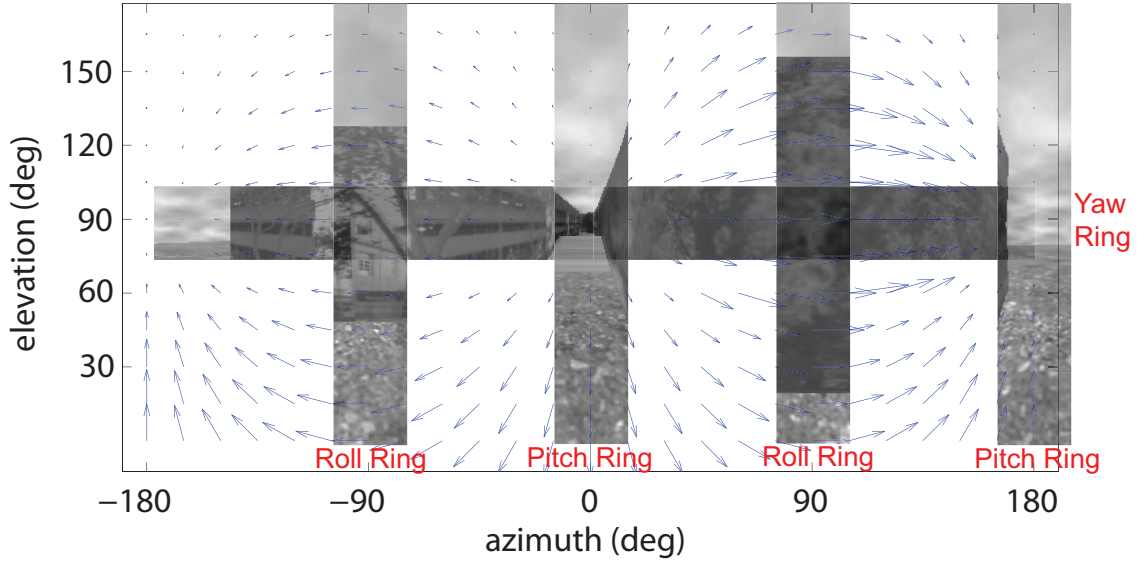
Figure 4.11: Optic flow sampling regions. Cameras form panoramas in 3 orthogonal planes, but optic flow is only measured in the mid-line regions of the panoramas.

just 20, then averaged vertically among the four rows of measurements. In both these steps outlier measurements with high final cost function or infeasibly large shift estimates are ignored in order to improve the signal to noise ratio. In the wide-field integration, the six spatial optic flow functions (for flow tangential and normal to each ring) are decomposed into their Fourier harmonics up to 2nd order. These are low-pass filtered in the temporal domain with a cut-off frequency of 30 rad/s to further reduce noise. The filtered values are then scaled and combined in the manner according to (4.15) to obtain the UAV actuator inputs. To avoid the ground being perceived as a lateral obstacle, the bank angle is constrained by shutting off lateral actuators when $|\phi| > 30°$. The simulation process is illustrated in Fig. 4.12.
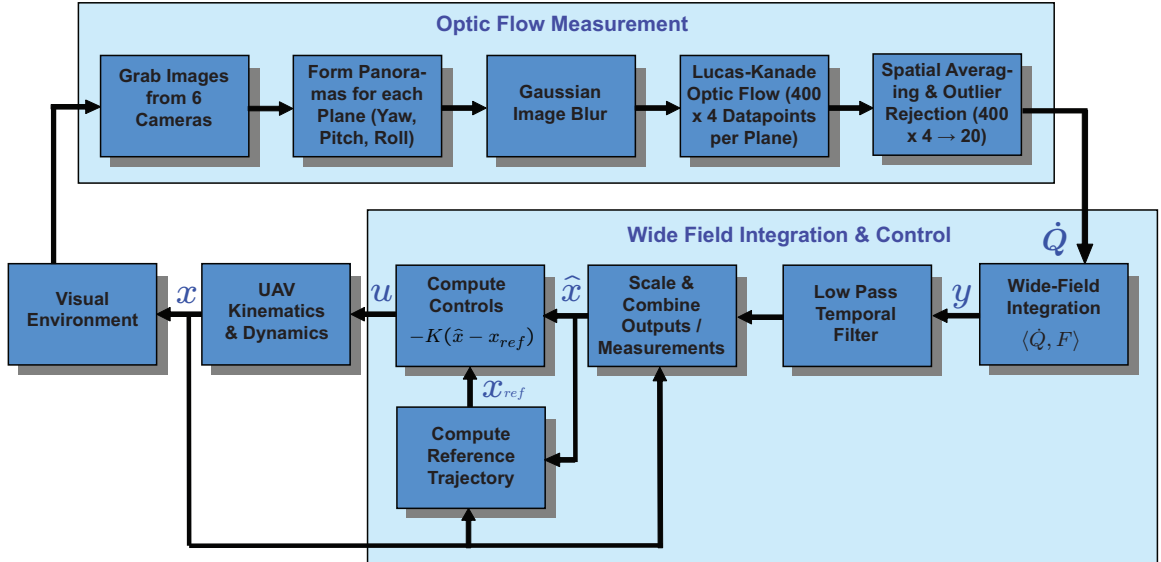
Figure 4.12: Ring-constrained WFI simulation process diagram.

Results

To demonstrate robustness with respect to initial conditions, several cases were simulated in each environment. Fig. 4.13 shows that the aircraft is able to successfully avoid the obstacles while maintaining a target height of $\sim$10 m above the ground in both environments. The initial lateral and vertical offsets in the tunnel do not affect the downrange trajectory. However, the different orientation offsets in the single-wall environment (Fig. 4.13A) lead to different final trajectories due to the finite length of the wall. When the aircraft flies beyond the wall there is a tendency to turn back toward the wall edge to balance obstacle orientation.

The plots of motion states (Fig. 4.14) for the Fig. 4.13B tunnel case indicate impressive accuracy in the measurement of side slip and angular rates. This is due to the fact that these quantities do not scale with a, unlike the w measurement, which appears poorly scaled because of its sensitivity to the presence of lateral obstacles. A pure scaling discrepancy is roughly equivalent to scaling the applicable
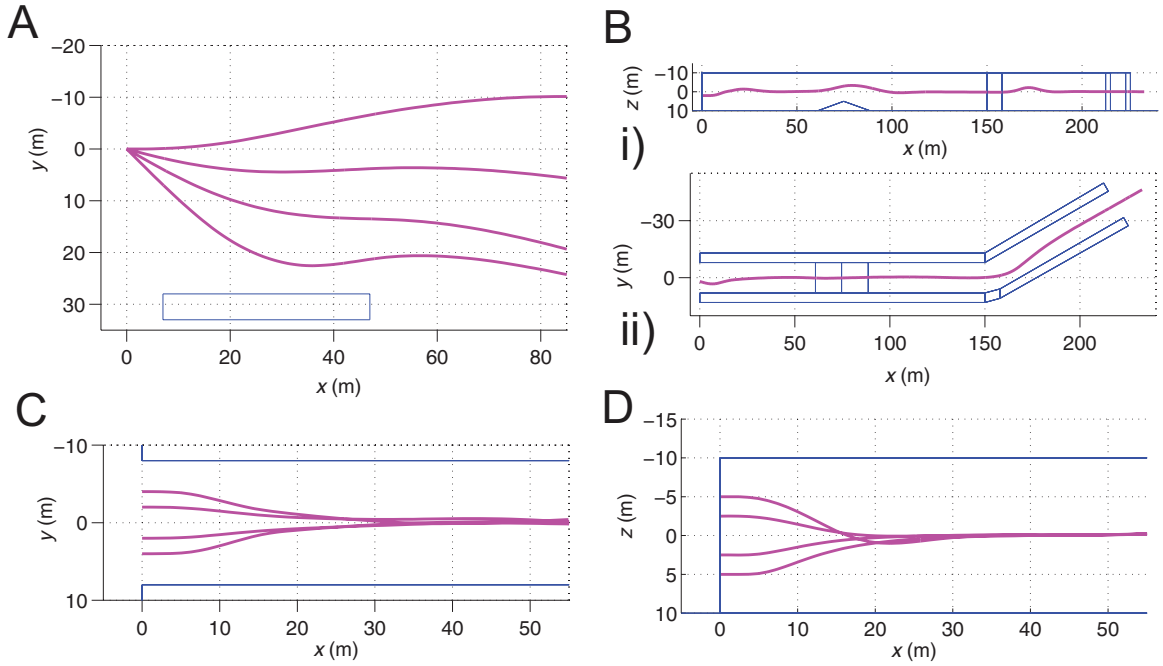
Figure 4.13: Simulation results - trajectories. (A) Single wall (initial $\psi = 0°, 15°, 30°, 45°$): plan view; (B) tunnel with 20° ramp and 30° bend (initial $y = 2, z = 2$ m, $\psi = 15°$): i) side view, ii) plan view. (C) tunnel (initial $y = -4, -2, 2, 4$ m): plan view; (D) tunnel (initial $z = -5, -2.5, 2.5, 5$ m): side view.
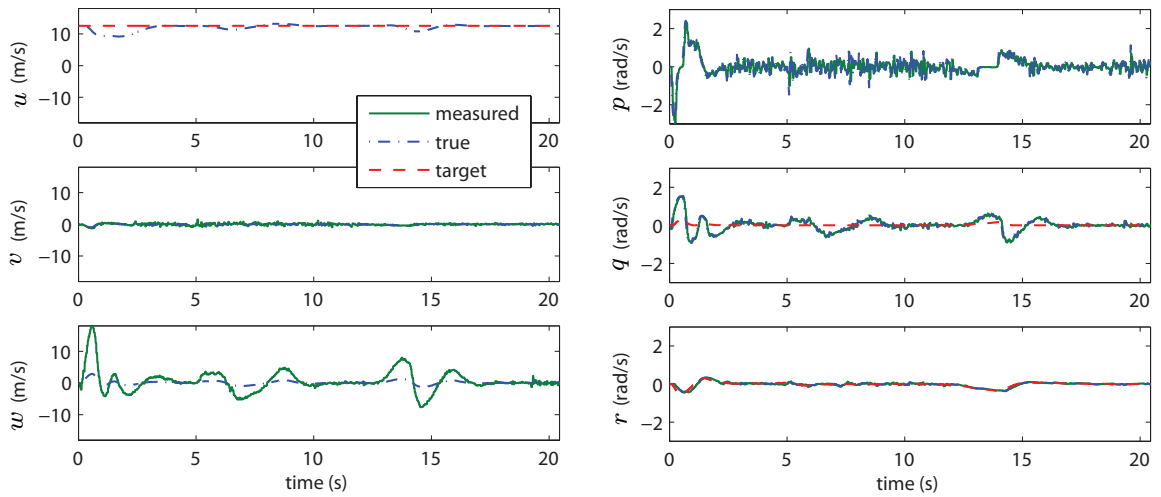
Figure 4.14: Simulation results for tunnel environment (initial $y = 2, z = 2$ m, $\psi = 15°$): speeds, rates and optic-flow-extracted measurements.
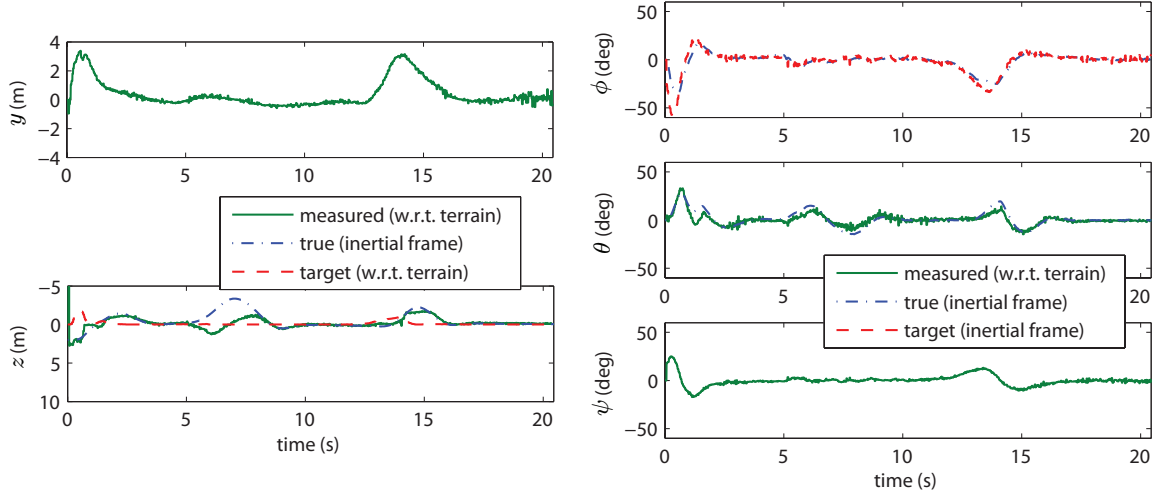
Figure 4.15: Simulation results for tunnel environment (initial $y = 2, z = 2$ m, $\psi = 15°$): configuration states and optic-flow-extracted measurements. Note: 'w.r.t.' denotes 'with respect to'.

feedback gain. Coordinated turn tracking is generally successful, but q_{ref} tracking is overshadowed by terrain following efforts.

The y and ψ plots spike at the beginning of the simulation (Fig. 4.15) due to the initial lateral offset and then again at the tunnel bend, which leads to subsequent banking and successful navigation of the anomaly. When the ramp appears under the aircraft the z and θ measurements become large and the UAV reacts by climbing. The target altitude is tracked satisfactorally, but this is hindered somewhat by engine saturation limits. Note that in the z and θ plots the 'true' curve illustrates the quantities with respect to the inertial frame, whilst the measured quantity is relative to the local terrain. The difference in reference frames explains their apparent discrepancies.

4.2.2 Micro Helicopter using Spherical WFI

In this section, the rigorous methods developed in Chapter 3 are applied to design weighting patterns that converge optic flow measured over the full sphere to actuator commands that stabilize a micro helicopter and permit navigation of a cluttered environment.

4.2.2.1 WFI-Based Controller

The vehicle selected for simulation is the 390 g E-sky Hobby Helicopter, with a 50.5 cm main rotor diameter and a 14.5 cm tail rotor. A linearized flight dynamics model was obtained in a prior study [79] via system identification with the US Army's CIFER software package. The kinematics and dynamics (4.17) are linearized about the forward flight condition, with u_{ref}=1 m/s. For simulation, the full non-

linear kinematic equations are used.

$$\dot{u} = -g\theta + X_u u$$

$$\dot{v} = g\phi + Y_v v - u_{\text{ref}} r$$

$$\dot{w} = Z_w w + Z_{\Omega_{\text{mr}}} \Omega_{\text{mr}} + u_{\text{ref}} q$$

$$\dot{p} = L_v v + L_\xi \xi$$

$$\dot{q} = M_u u + M_\chi \chi \tag{4.17}$$

$$\dot{r} = N_r r + N_{\Lambda_{\text{yaw}}} \Lambda_{\text{yaw}}$$

$$\dot{\xi} = -p - \frac{1}{\tau_f}\xi + \frac{\xi_\chi}{\tau_f}\chi + \frac{\xi_{\text{lat}}}{\tau_f}\Lambda_{\text{lat}} + \frac{\xi_{\text{lon}}}{\tau_f}\Lambda_{\text{lon}}$$

$$\dot{\chi} = -q + \frac{\chi_\xi}{\tau_f}\xi - \frac{1}{\tau_f}\chi + \frac{\chi_{\text{lat}}}{\tau_f}\Lambda_{\text{lat}} + \frac{\chi_{\text{lon}}}{\tau_f}\Lambda_{\text{lon}}$$

$$\dot{\Omega}_{\text{mr}} = T_{\Omega_{\text{mr}}} \Omega_{\text{mr}} + T_{\Lambda_t} \Lambda_t .$$

The actuator saturation limits are: $|\Lambda_{\text{lat}}| \le 1$, $|\Lambda_{\text{lon}}| \le 1$, $|\Lambda_t| \le 0.5$ and $|\Lambda_{\text{yaw}}| \le 1$.

Characteristic stability quantities are defined in Table 4.5 with SI units.

Table 4.5: Micro helicopter stability characteristics

$X_u = -0.5214$	$\tau_f = 0.15$
$Y_v = -0.4799$	$\xi_\chi = 1.55$
$Z_w = -0.6802$	$\xi_{\text{lat}} = 0.245$
$Z_{\Omega_{\text{mr}}} = 0.170$	$\xi_{\text{lon}} = 0.043$
$L_v = -8.246$	$\chi_\xi = -2.82$
$L_\xi = 1273$	$\chi_{\text{lat}} = 0.044$
$M_u = 3.599$	$\chi_{\text{lon}} = -0.202$
$M_\chi = 341.6$	$T_{\Omega_{\text{mr}}} = -6.182$
$N_r = -0.8786$	$T_{\Lambda_t} = 1449$
$N_{\Lambda_y} = 39.06$	$g = 9.81$

The feedback control objective is to regulate the relative state estimates provided by WFI to specified reference values, thereby generating stable obstacle avoidance and terrain following behaviors. The proposed methodology assumes that an altitude measurement $\tilde{z}$ is available for feedback, along with the actuator states $\{\xi, \chi, \Omega_{\mathrm{mr}}\}$. The independent altitude measurement is required to remove target altitude dependence on obstacle distribution in the environment (see Section 7.5). The estimates for the remaining 10 relative states are generated using the optimal weighting functions from (3.20),

$$\hat{x}_i \;=\; \langle \dot{\mathbf{Q}}, \mathbf{F}_{\hat{x}_i} \rangle + C^{\dagger}_{i,M+1}\tilde{z}, \tag{4.18}$$

where $M + 1$ is the column of $C^{\dagger}$ corresponding to the independent attitude measurement $\tilde{z}$. The initial weighting pattern set $F_{\mathbf{y}}$ is chosen to be spherical harmonics up to 10th degree. Construction of the C matrix can only be done numerically given the complexity of the distance function (2.10) (flat surface world assumed, without front and rear surfaces, as in (3.8)), and it is too large to present here. With the angular spacing of measurement nodes set to $9°$ for real-time implementation, the weighted-least squares inversion (3.9) results in the state extraction functions presented in Fig. 4.16. Note that the u-estimator pattern extracts forward speed from the ground-induced optic flow rather than from lateral obstacles. This is a direct consequence including the term $R_{\delta C}$ in the design of $C^{\dagger}$, which penalizes the uncertain spacing of lateral objects compared with the relatively well known proximity of the ground.
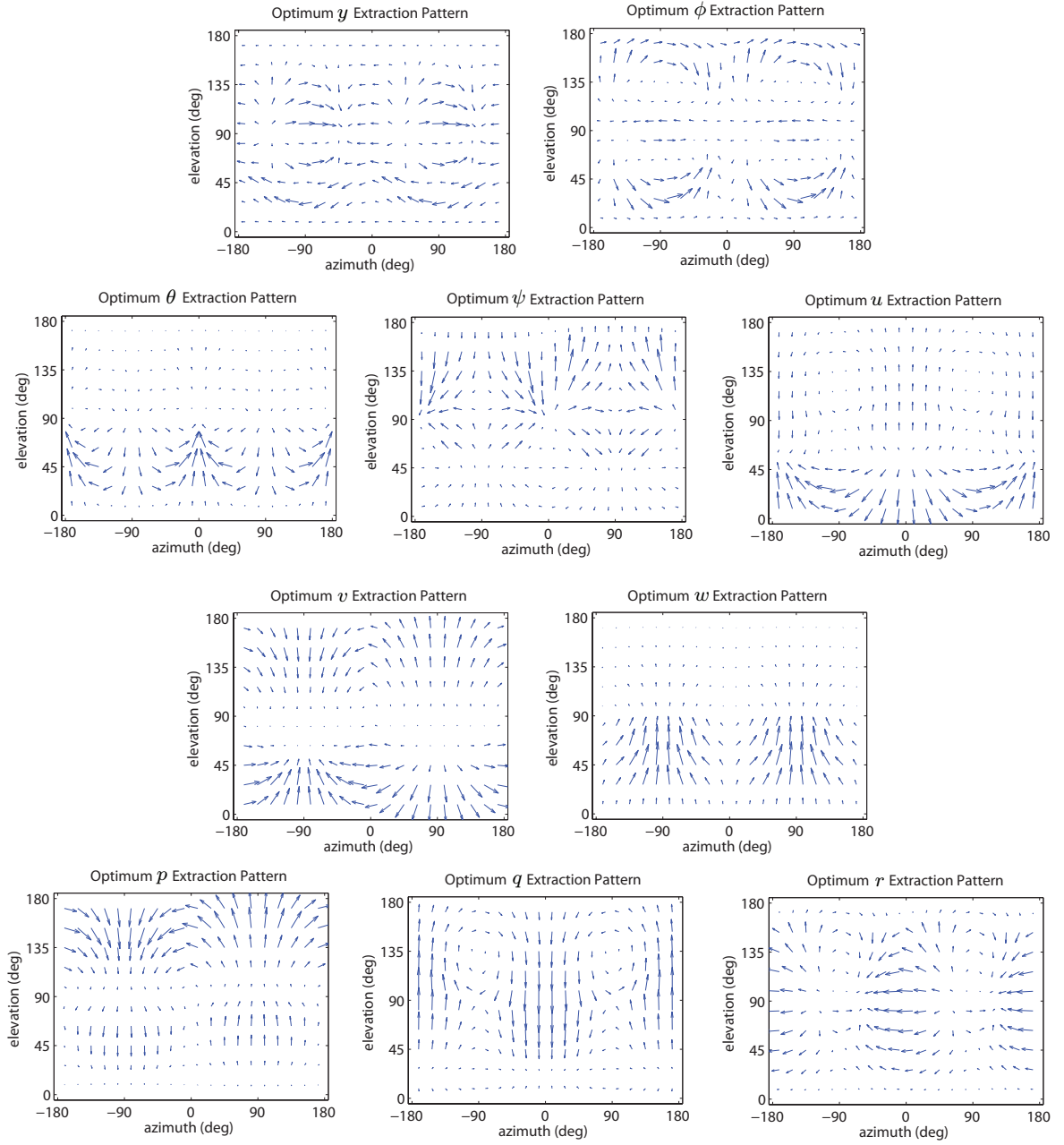
Figure 4.16: Optimum weighting patterns to recover environment-scaled states from optic flow field.

It has been assumed that the vehicle can measure optic flow over the entire spherical viewing arena, but this may create hardware design complications and possible optic flow computation issues if the sky is uniformly blue or overcast. A rotating vehicle will not induce a perceptable optic field with a zero-contrast background, thus all WFI-based relative states will be distorted, leading to potential instability. It is therefore beneficial for robustness to measure optic flow below the horizon only - where the existence of suitable image contrast is more probable. The measurement domain can theoretically be arbitrarily small and still permit relative state estimates via WFI, however Fisher information theory shows that the estimates will become less robust to noise as the field of view decreases. Using (3.8) and (3.15), it can be shown that the noise throughput (3.18) roughly triples by restricting the field-of-view to below the horizon only. This is deemed an acceptable price for the ability to operate in conditions where the sky has no visual contrast. The optimum weighting patterns with a lower hemisphere measurement grid are presented in Fig. 4.17. The default design will still use the full spherical weightings, but a performance comparison (Fig. 4.24C-D) will be made with the alternative half-sphere configuration.

The desired reference for the state vector $\mathbf{x} = (y, z, \phi, \theta, \psi, u, v, w, p, q, r, \xi, \chi, \Omega_{\mathrm{mr}})$, which accounts for the pitch and rotor speed variation from hover required to reach 1 m/s, is taken as

$$\mathbf{x}_{\mathrm{ref}} = (0, K_{z,\theta}(\hat{\theta} - \tilde{\theta}), 0, -0.05, 0, 1.00, 0, -0.05, 0, 0, 0, 0, 0, 0.21). \qquad (4.19)$$
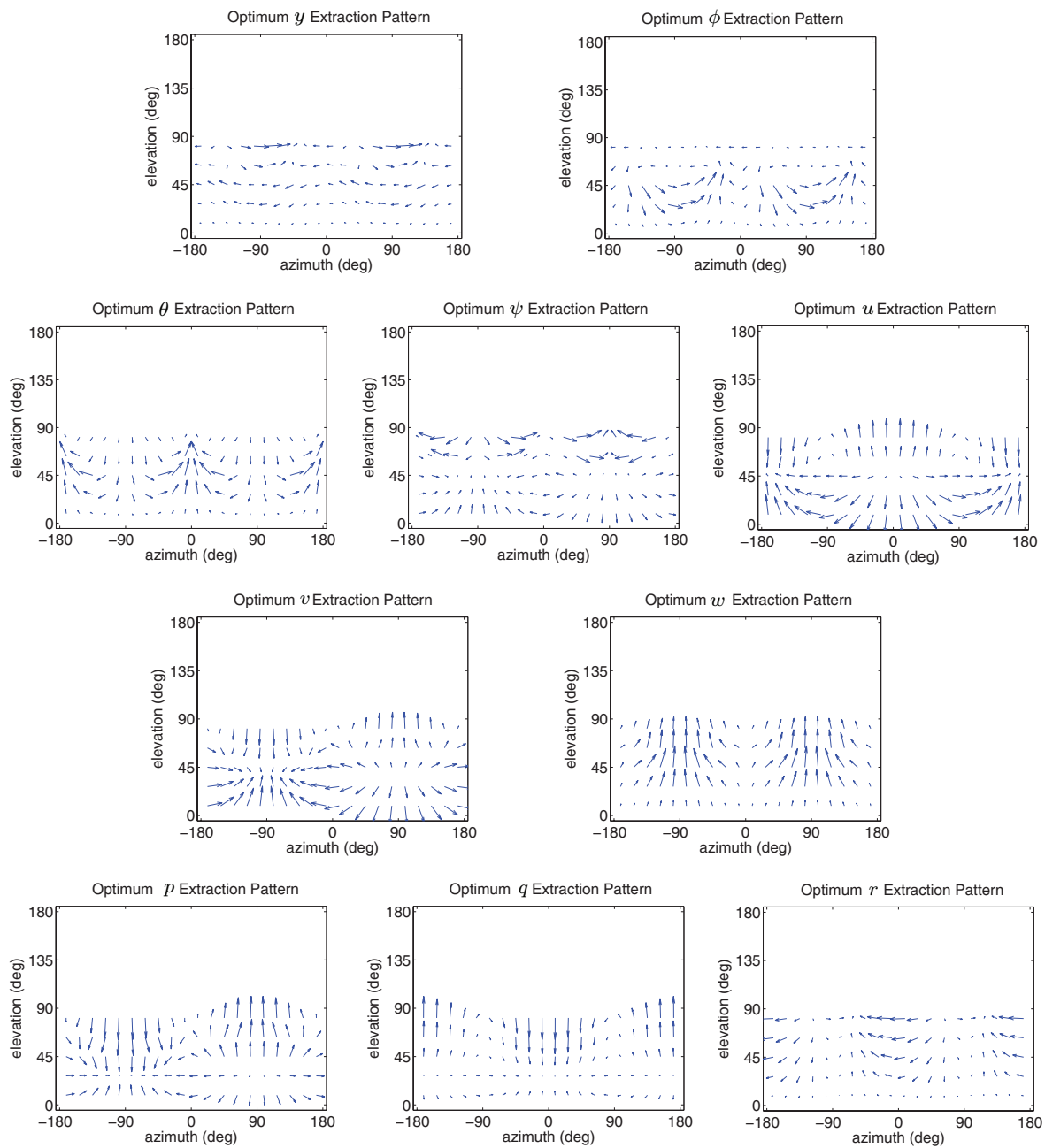
Figure 4.17: Optimum weighting patterns to recover environment-scaled states from optic flow field, restricted to lower hemisphere measurements.

Note the target altitude offset $z_{\text{ref}} = K_{z,\theta}(\hat{\theta} - \tilde{\theta})$ is a function of the pitch angle measurement relative to the gravity vector $\tilde{\theta}$ (assumed to be provided by an additional sensor) and the WFI estimate $\hat{\theta}$ from (4.18), which provides an indication of upcoming terrain. This form of the reference is chosen in order to avoid unacceptable speed loss during climbs over steep terrain. To prevent excessive or unnecessary vertical velocities, z_{ref} is intentionally restricted to be zero except when in the range (-1,0). Furthermore, the pitch angle estimate $\tilde{\theta}$ is subtracted from the WFI-based estimate $\hat{\theta}$ to preclude superfluous climb commands arising from the nominal specified value of $\hat{\theta} = -0.05$. It is important to note that different behaviors can be rapidly realized during flight by adjusting the target state (4.19) - which essentially specifies desired optic flow asymmetry. Setting a non-zero y_{ref}, for example, will cause the vehicle to track a non-centered path or, in the extreme, hug a wall.

Assuming a linear tracking controller, the structure of the feedback law can be written as:

$$ u_k \;=\; \sum_i K_{k,x_i}\!\left(\langle \dot{\mathbf{Q}}, \mathbf{F}_{\hat{x}_i} \rangle + C^{\dagger}_{i,M+1}\tilde{z} - x_{i,\text{ref}} \right) + \sum_j K_{k,x_j}(\hat{x}_j - x_{j,ref}), \quad (4.20) $$

where $k = \{\Lambda_{\text{lat}}, \Lambda_{\text{lon}}, \Lambda_{\text{t}}, \Lambda_{\text{yaw}}\}$ denotes the actuator input, $i = \{y, \phi, \psi, u, v, w, p, q, r\}$ is the set of WFI-based state measurements and $j = \{z, \theta, \xi, \chi, \Omega_{\text{mr}}\}$ is the set of states measured with alternate sensors. LQR is employed to obtain a set of optimal feedback gains. After iteration with the simulator, the LQR state penalty matrix was set to $J_{\mathbf{x}} = \text{diag}(25, 1, 1, 1, 5, 100, 20, 5, 1, 1, 1, 10^{-15}, 10^{-15}, 10^{-15})$ and the control penalty matrix to $J_{\mathbf{u}} = \text{diag}(1, 1, 1, 1)$. Table 4.6 lists the final gains.

Table 4.6: Micro helicopter feedback gains

Cyclic Lat.	Cyclic Lon.	Main Rotor	Tail	Reference
$K_{\Lambda_{\text{lat}},y} = -4.70$	$K_{\Lambda_{\text{lon}},y} = -0.12$	$K_{\Lambda_t,y} = 0.01$	$K_{\Lambda_{\text{yaw}},y} = -1.70$	$K_{z,\theta} = 3.50$
$K_{\Lambda_{\text{lat}},z} = 0.00$	$K_{\Lambda_{\text{lon}},z} = 0.01$	$K_{\Lambda_t,z} = 1.00$	$K_{\Lambda_{\text{yaw}},z} = 0.00$	
$K_{\Lambda_{\text{lat}},\phi} = -11.05$	$K_{\Lambda_{\text{lon}},\phi} = -0.17$	$K_{\Lambda_t,\phi} = 0.03$	$K_{\Lambda_{\text{yaw}},\phi} = 1.78$	
$K_{\Lambda_{\text{lat}},\theta} = -0.73$	$K_{\Lambda_{\text{lon}},\theta} = 19.02$	$K_{\Lambda_t,\theta} = -0.63$	$K_{\Lambda_{\text{yaw}},\theta} = 0.03$	
$K_{\Lambda_{\text{lat}},\psi} = -3.42$	$K_{\Lambda_{\text{lon}},\psi} = -0.07$	$K_{\Lambda_t,\psi} = 0.01$	$K_{\Lambda_{\text{yaw}},\psi} = -2.60$	
$K_{\Lambda_{\text{lat}},u} = 0.22$	$K_{\Lambda_{\text{lon}},u} = -8.70$	$K_{\Lambda_t,u} = 0.18$	$K_{\Lambda_{\text{yaw}},u} = -0.01$	
$K_{\Lambda_{\text{lat}},v} = -4.35$	$K_{\Lambda_{\text{lon}},v} = -0.17$	$K_{\Lambda_t,v} = 0.01$	$K_{\Lambda_{\text{yaw}},v} = 2.01$	
$K_{\Lambda_{\text{lat}},w} = 0.00$	$K_{\Lambda_{\text{lon}},w} = 0.06$	$K_{\Lambda_t,w} = 2.20$	$K_{\Lambda_{\text{yaw}},w} = 0.00$	
$K_{\Lambda_{\text{lat}},p} = -0.81$	$K_{\Lambda_{\text{lon}},p} = 0.13$	$K_{\Lambda_t,p} = 0.00$	$K_{\Lambda_{\text{yaw}},p} = 0.03$	
$K_{\Lambda_{\text{lat}},q} = 0.05$	$K_{\Lambda_{\text{lon}},q} = 1.32$	$K_{\Lambda_t,q} = 0.07$	$K_{\Lambda_{\text{yaw}},q} = 0.00$	
$K_{\Lambda_{\text{lat}},r} = 0.03$	$K_{\Lambda_{\text{lon}},r} = 0.00$	$K_{\Lambda_t,r} = 0.00$	$K_{\Lambda_{\text{yaw}},r} = -1.09$	
$K_{\Lambda_{\text{lat}},\xi} = -29.70$	$K_{\Lambda_{\text{lon}},\xi} = -4.35$	$K_{\Lambda_t,\xi} = -0.10$	$K_{\Lambda_{\text{yaw}},\xi} = 0.64$	
$K_{\Lambda_{\text{lat}},\chi} = -5.49$	$K_{\Lambda_{\text{lon}},\chi} = 20.43$	$K_{\Lambda_t,\chi} = 0.48$	$K_{\Lambda_{\text{yaw}},\chi} = 0.09$	
$K_{\Lambda_{\text{lat}},\Omega_{\text{mr}}} = 0.00$	$K_{\Lambda_{\text{lon}},\Omega_{\text{mr}}} = 0.00$	$K_{\Lambda_t,\Omega_{\text{mr}}} = -0.02$	$K_{\Lambda_{\text{yaw}},\Omega_{\text{mr}}} = 0.00$	

As described in Chapter 3, the control law can be rewritten in a more computationally efficient form that requires only one WFI operation per actuator;

$$u_k = \langle \dot{\mathbf{Q}}, \mathbf{F}_{u_k} \rangle + \sum_i K_{k,x_i} \left(C_{i,M+1}^\dagger \tilde{z} - x_{i,\text{ref}} \right) + \sum_j K_{k,x_j} (\hat{x}_j - x_{j,ref}), \quad (4.21)$$

where the sensor-to-actuator mapping patterns $\mathbf{F}_{u_k}$ are defined in (3.5) and presented in Fig. 4.18.

4.2.2.2 Stability and Robustness Analysis

The robust stability analysis of Section 4.2.1.2 is applied to the micro helicopter with full-sphere WFI. The observation equation describing the linearized information
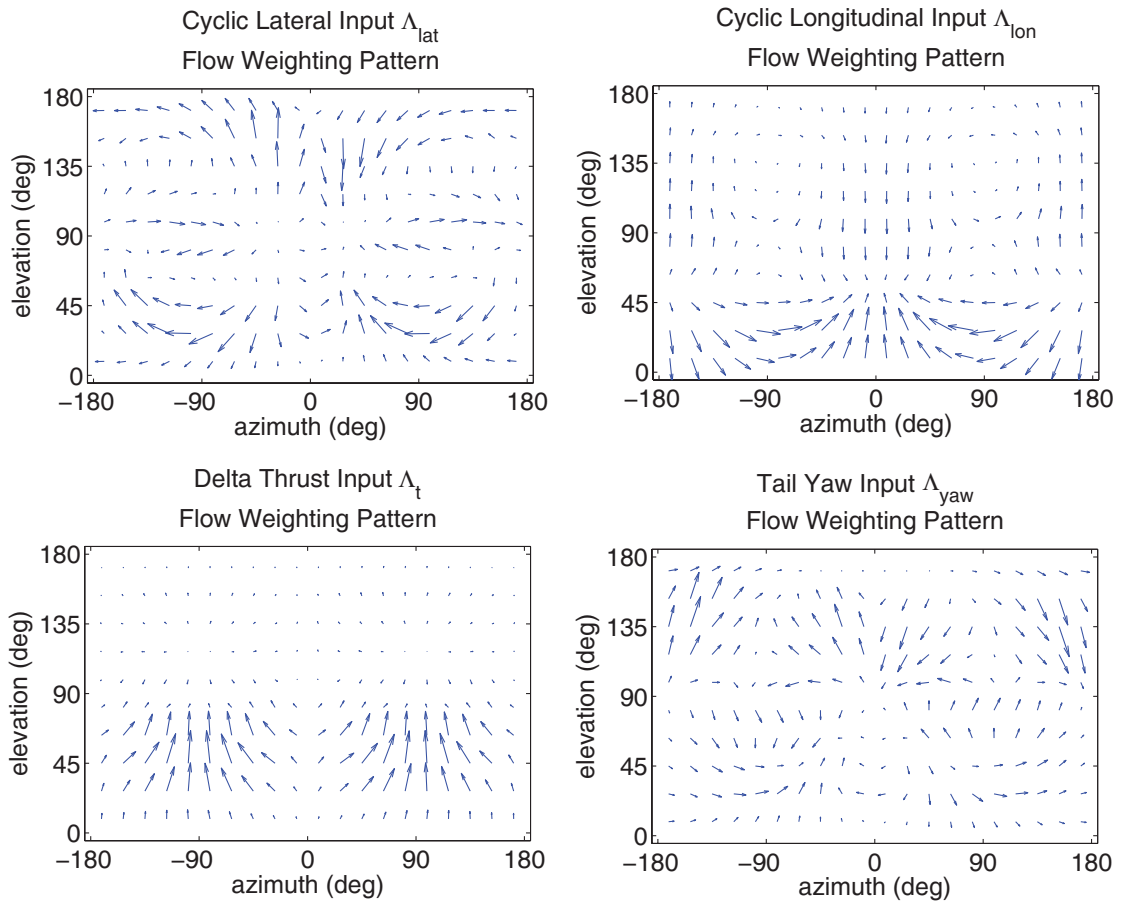
Figure 4.18: Optimum weighting patterns to extract stabilizing control commands from optic flow field.
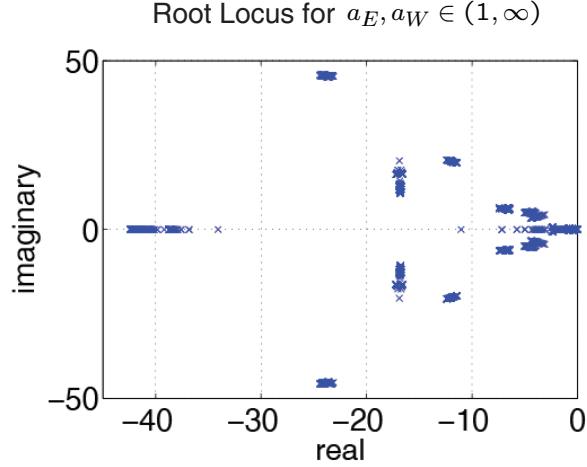
Figure 4.19: Root locus diagram for range of wall spacings. Closed-loop eigenvalues computed for a_W and a_E independently ranging from 1 m to 1000 m ($\sim \infty$) in steps of 1 m.

contained in the state estimates is

$$\hat{\mathbf{x}} = C_{\hat{\mathbf{x}}}\mathbf{x} \tag{4.22}$$

$$C_{\hat{\mathbf{x}}} = \text{diag}(1, 0, 1, 0, 1, 1, 1, 1, 1, 1, 1, 0, 0, 0)C^\dagger C$$

$$+\text{diag}(0, 1, 0, 1, 0, 0, 0, 0, 0, 0, 0, 1, 1, 1),$$

where $C_{\hat{\mathbf{x}}} \neq I$ if $C \neq C_0$. Closed-loop eigenvalue analysis shows that the inner loop is small-perturbation stable across the entire family of modeled outdoor environments (Fig. 4.19). By rigorously accounting for C uncertainty in the optimal approach to designing $C^\dagger$, the robust-stability region is enlarged compared with the manual-design approach of 4.2.1.1. The outer loop (dynamic reference trajectory) does not alter the system stability under the assumption of the flat terrain environment model; in which case $\hat{\theta} \simeq \tilde{\theta}$.

4.2.2.3 Simulation

Optic Flow Sensing and Computation

This section describes the methodology for simulating the micro helicopter in a cluttered urban environment (Fig. 4.20). Greater maneuvrability and a lower forward speed, compared with the fixed-wing UAV of Section 4.2.1, permit navigation of a more complex environment with more severe initial conditions. The same camera setup is employed (Fig. 4.21) but is run at 60 fps for optic flow computation at 800 image points. The points are distributed in a u-v spherical grid with constant angular spacing between nodes, and are mapped from a virtual sphere surface to the flat cameras via geometric projection (Appendix A.2). The optic flow measurements are mapped back to the sphere (Eq. (A.7)), then de-sampled from 800 to 200 by unweighted averaging of 'square' groups of four adjacent nodes, with outlier rejection to reduce noise. The simulation process is illustrated in Fig. 4.22.

To demonstrate robustness with respect to initial conditions, a monte carlo approach was employed. 20 initial headings and (x,y) locations were generated using a uniform distribution, excluding parts of the environment covered by buildings.

Results

Fig. 4.23 shows that from all initial conditions the helicopter is able to successfully avoid the obstacles while maintaining a target height of 1 m above the ground. This is achieved almost entirely with optic-flow-based measurements, with the exception of the independent pitch angle, altitude and actuator-related state measurements.
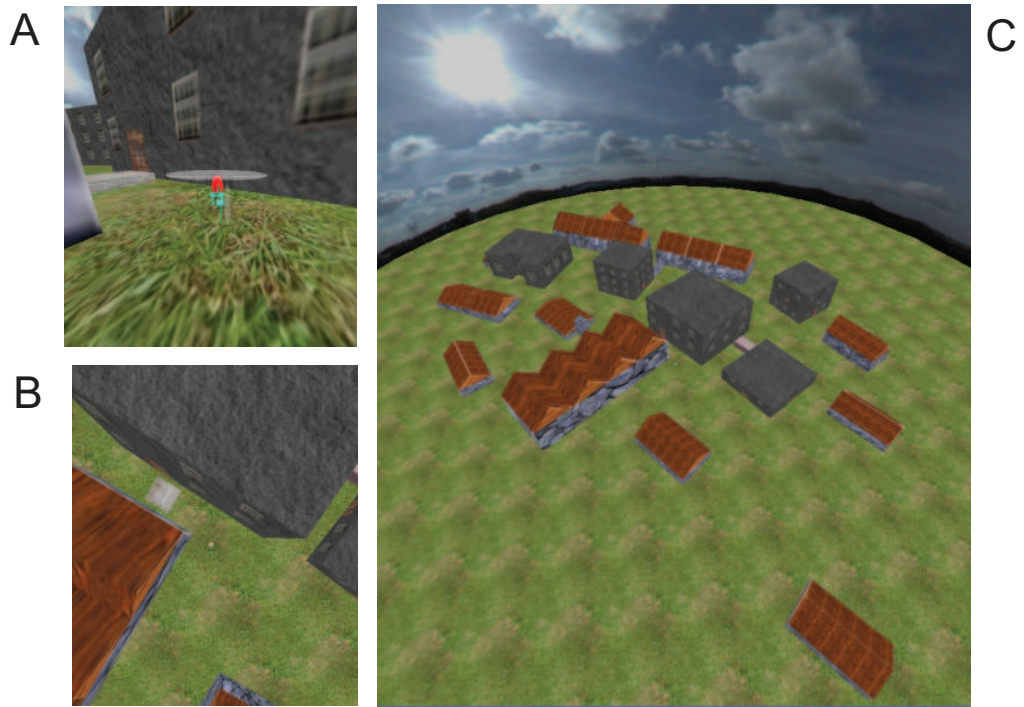
Figure 4.20: 3-D simulation environment.
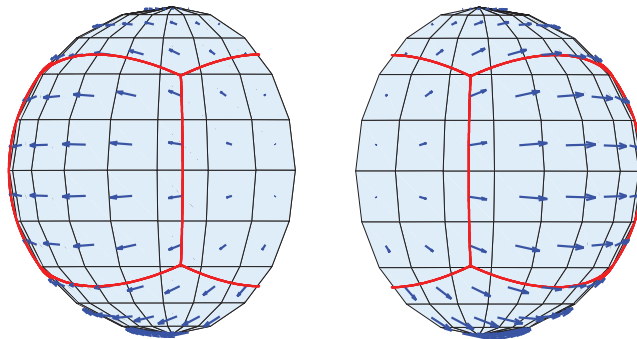
Figure 4.21: Sampling the optic flow field: projections of camera boundaries on to right and left hemispheres of the sphere.

Optic Flow Measurement

Grab Images from 6 Cameras → Gaussian Image Blur → Lucas-Kanade Optic Flow (at 800 pixel coordinates) → Spatial Block Averaging & Outlier Rejection (800→200)

Wide Field Integration & Control $\dot{Q}$

Visual Environment ← x UAV Kinematics & Dynamics ← u Compute Controls $-K(\hat{x} - x_{ref})$ ← Combine WFI and Sensor Measurements ← $\hat{x}$ Wide-Field Integration

x_{ref}

Compute Reference Trajectory

Figure 4.22: Spherical WFI simulation process diagram.

There are several instances where the helicopter heads back toward the buildings after clearing the obstacle course, but this is a reaction to the large sky-dome that surrounds the environment (Fig. 4.20C). Fig. 4.24E shows the helicopter climbing over a box completely obstructing its path, which is made possible by the adjustment of target altitude. The terrain pitch angle spikes as the helicopter approaches the box, which pushes the target altitude up, forcing the vehicle to temporarily track an altitude-above-ground greater than 1 m in order to more safely approach the upcoming terrain. Restricting the measurement grid to the lower hemisphere (Figs. 4.24C and D) resulted in roughly similar performance, but eventual deviation in trajectories due to differences in the y and ψ estimates. The full measurement grid covers the entire height of the buildings thus the vehicle has stronger and earlier warning of lateral obstacles compared with the reduced-FOV lower hemisphere grid.
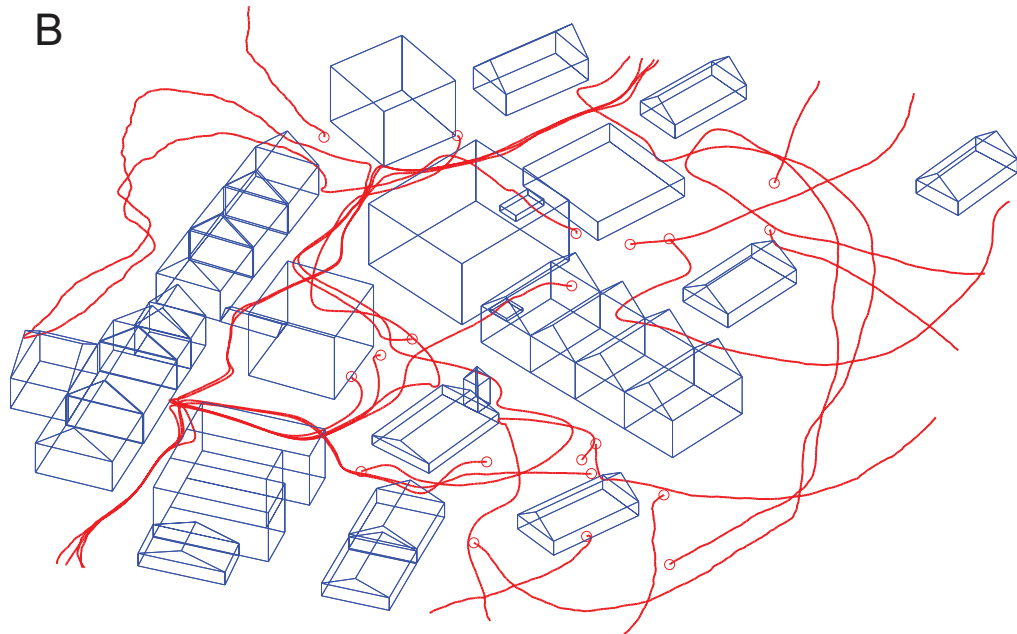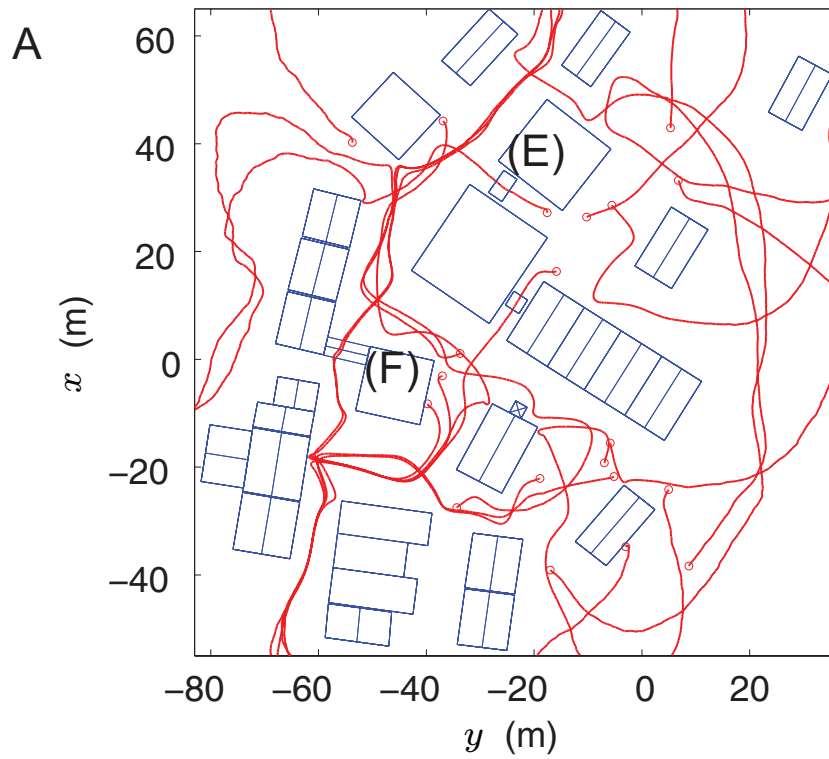
Figure 4.23: Simulation results - trajectories (Part 1). (A) Plan view of all trajectories using full spherical measurement grid, (B) alternate view of trajectories.
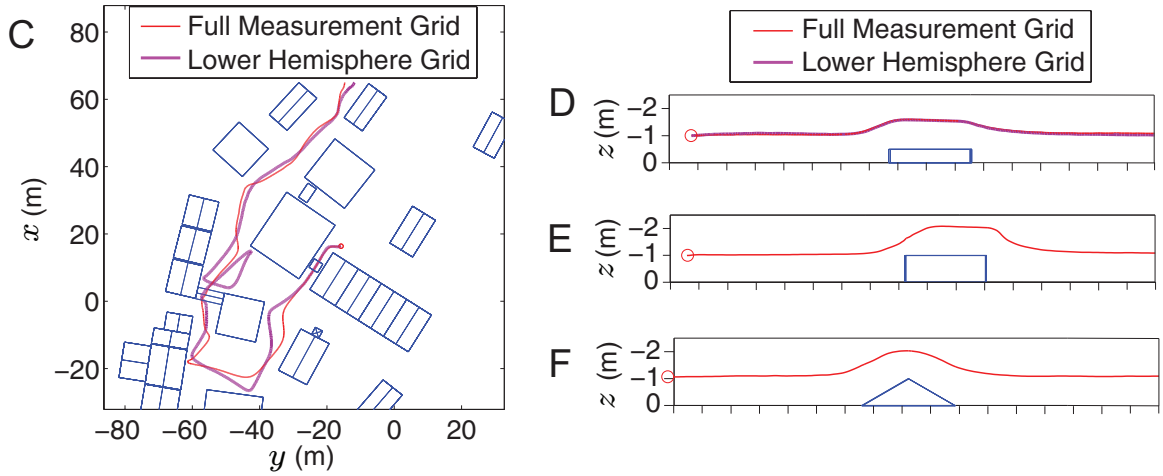
Figure 4.24: Simulation results - trajectories (Part 2). (C) Plan view comparison between spherical measurement grid and half-sphere grid for a single initial condition, (D) side view comparison during navigation over a 0.5 m box, (E) 1 m box, (F) 1 m ramp.
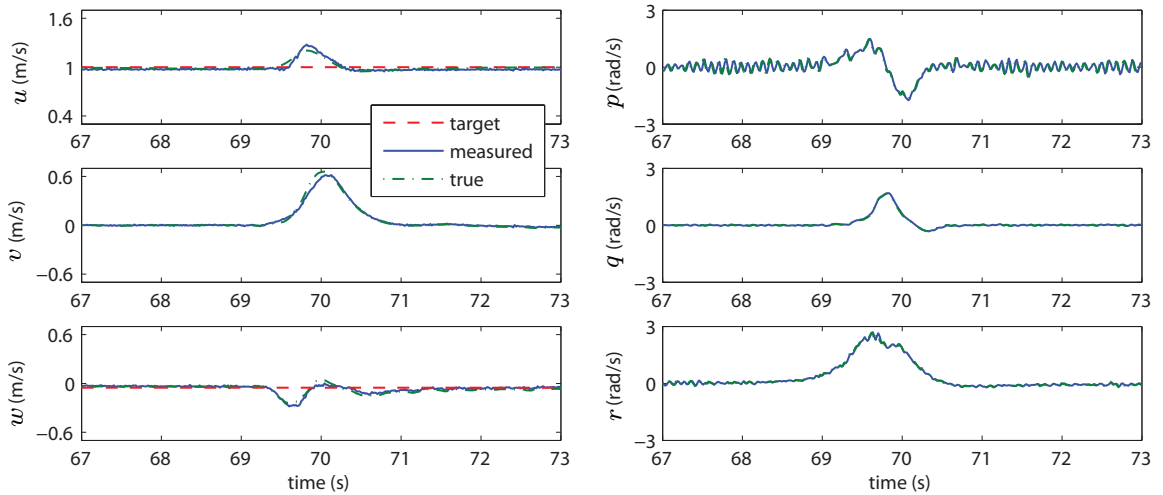
Figure 4.25: Speeds, rates and optic-flow-extracted measurements for the full spherical measurement grid case (Fig. 4.23C) during a 90° turn.
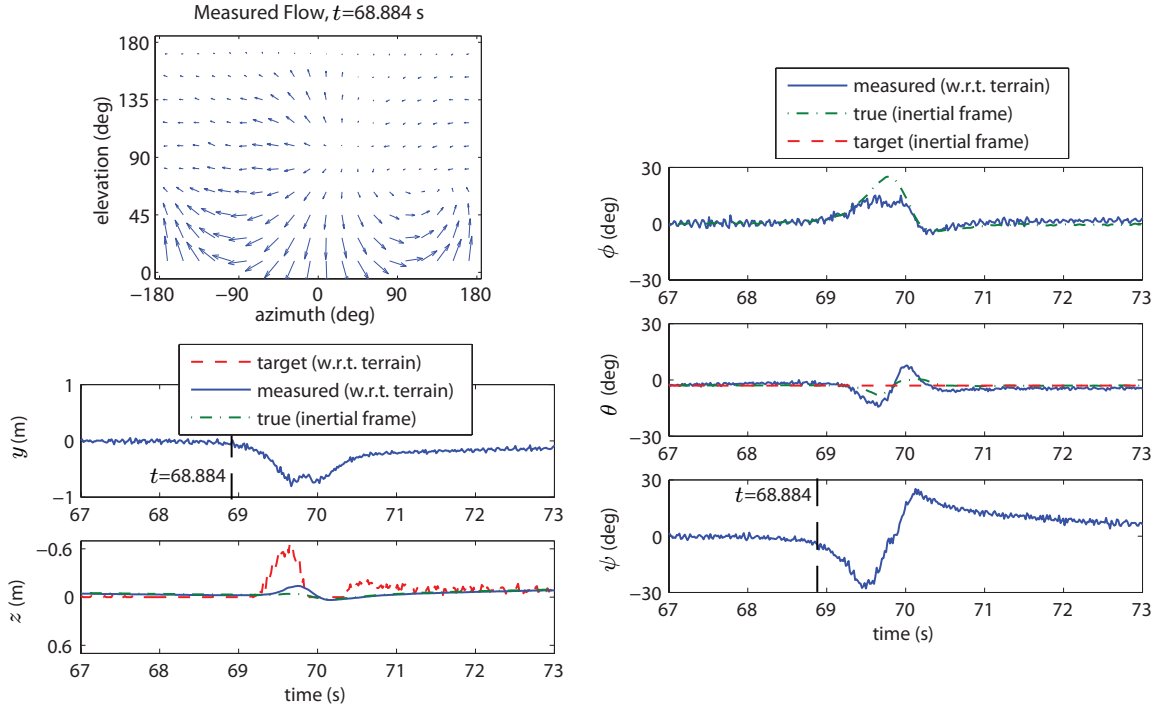
Figure 4.26: Vehicle pose, WFI outputs and measured optic flow for the full spherical measurement grid case (Fig. 4.23C during a 90° turn.

Figs. 4.25 and 4.26 show the states and measurements for part of the Fig. 4.24C trajectory (during the second major turn). The asymmetry in the optic flow pattern that prompts an avoidance maneuver is evident from Fig. 4.26. Despite the fact that the WFI delivers environment-sensitive state estimates, the measurements still satisfactorily track the true quantities. The low noise levels are attributable to the white-noise mitigation property of wide-field integration and the outlier rejection step in the spatial filtering of optic flow measurements. The environment-related scaling error in the ϕ estimate does not compromise roll stability, but the high gain on the ψ and y does lead to oscillations from the feedback of finite noise.

Chapter 5

Control Theoretic Interpretation of Tangential Cells

Whilst Chapters 3 and 4 are concerned with deriving the optimal WFI weighting patterns for controlling robotic platforms, this chapter examines the fixed directional templates ingrained into the tangential cells of insects. The analysis techniques are the same, but the weighting patterns are now fixed, rather than being freely designable. This chapter seeks to address (1) the estimation question: what do tangential cell outputs encode, and (2) the control question: how can they give rise to the navigational heuristics observed by behavioral biologists. These are questions to which biologists have long sought an answer [3], and the insight gained by addressing this research gap will further the understanding of how the insect architecture can be effectively leveraged for MAVs.

The properties of tangential cells are more complex than the simple linear-integrator analogue of Section 2.3, but the analogue still provides a useful theoretical framework for analyzing the patterns. Section 5.1 investigates the above mentioned research questions in a simplified planar context and Section 5.2 extends the analysis to 3-D, to examine the hypothesis proposed by biologists that tangential cells are tuned to sense the insect's fundamental dynamics modes [3]. Insect weighting patterns, or directional templates, were obtained from published data [1, 2, 3] for all available tangential cells of the blow fly *Calliphora* (Figs. 5.1 and 5.2).
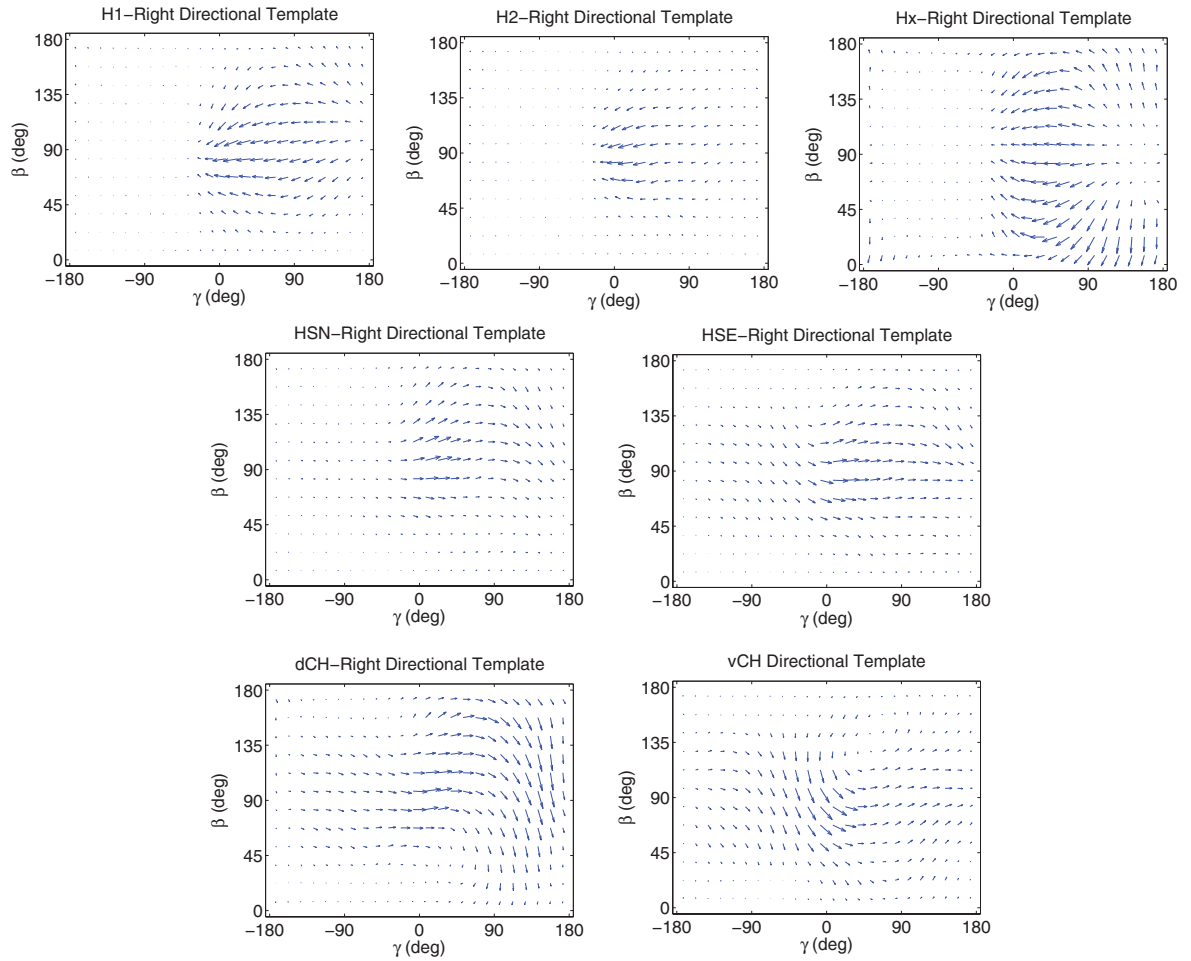
Figure 5.1: Directional templates of right brain hemisphere *Calliphora* tangential cells sensitive to primarily horizontal optic flow.
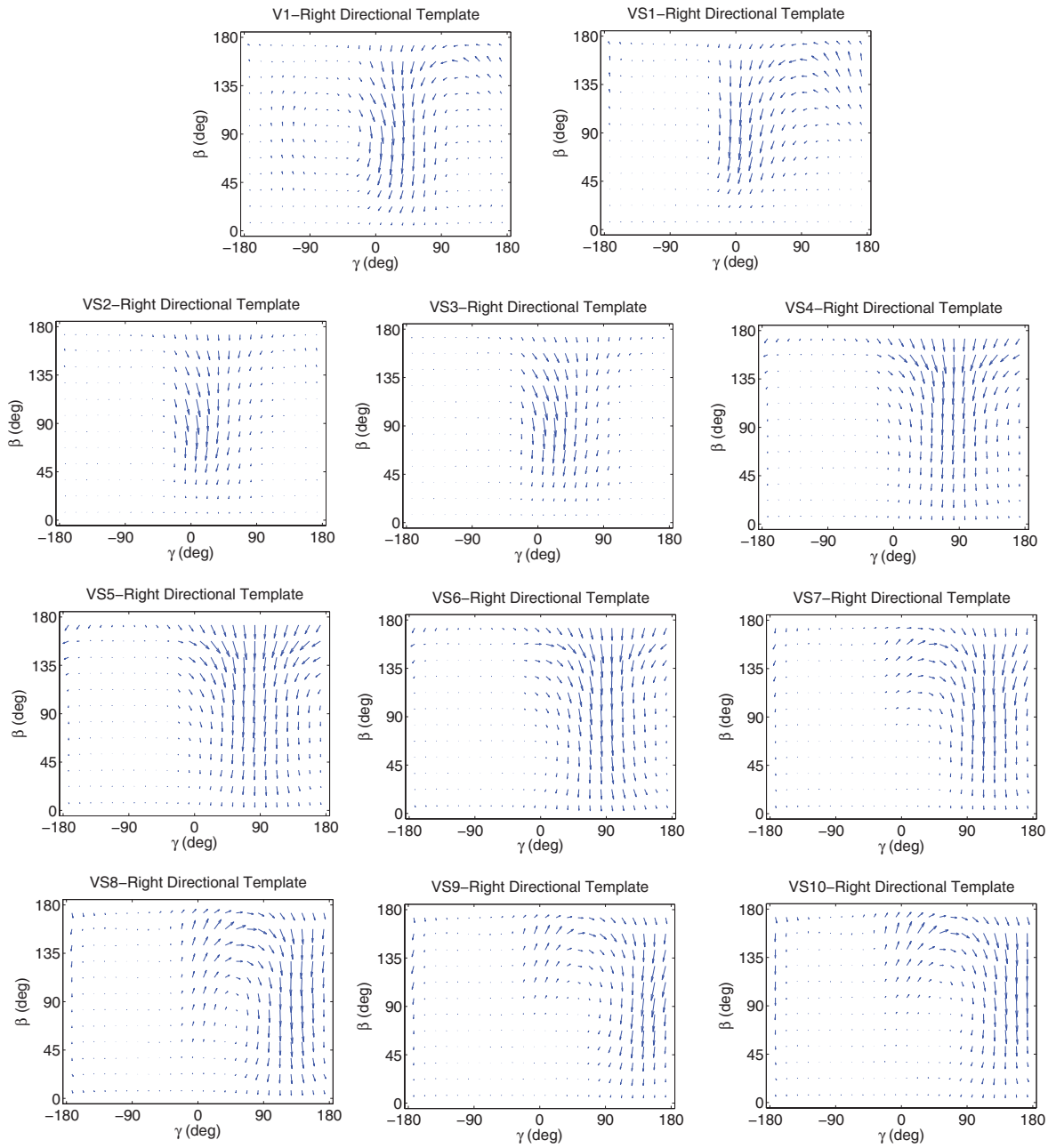
Figure 5.2: Directional templates of right brain hemisphere *Calliphora* tangential cells sensitive to primarily vertical optic flow.

5.1 1-D Tangential Cell Directional Templates

In this section the 1-D WFI operator (4.2) is used as a tangential cell (TC) analogue to characterize the information that is encoded by the azimuthal directional templates of tangential cells that compose the horizontal system (HS). The loop closure design techniques developed in Chapter 3 are applied to show how tangential cell analogue outputs could be used to stabilize and navigate.

5.1.1 Decoding TC Patterns

To provide initial insight into the interpretation of tangential cell patterns and their possible role in the visuomotor loop, we consider insect motion restricted to the horizontal plane. Therefore, the directional templates for the horizontal cells (H1, H2, Hx, HSN, HSE, HSS, dCH and vCH) for both the left (L) and right (R) hemispheres are included in the analysis. If one further restricts optic flow measurements to the equatorial plane, then only the azimuthal-equatorial components of the spherical weighting patterns are required. Representative data points for the tangential cell weighting patterns were obtained from published data for each cell, smoothed with a Gaussian filter and converted to a continuous function of γ by making a 12th order Fourier series approximation (e.g., Fig. 5.3). The resulting 16 weightings $\mathbf{F_y} = \{F_{y_i}, \ i = 1, \ldots, 16\}$ are then normalized so that a perfect match of the optic flow field with the weighting function will result in unity output.

To characterize the small signal content encoded by the azimuthal-equatorial cell directional templates, the set of outputs $\langle \dot{Q}, F_{y_i} \rangle$ are linearized about the nominal
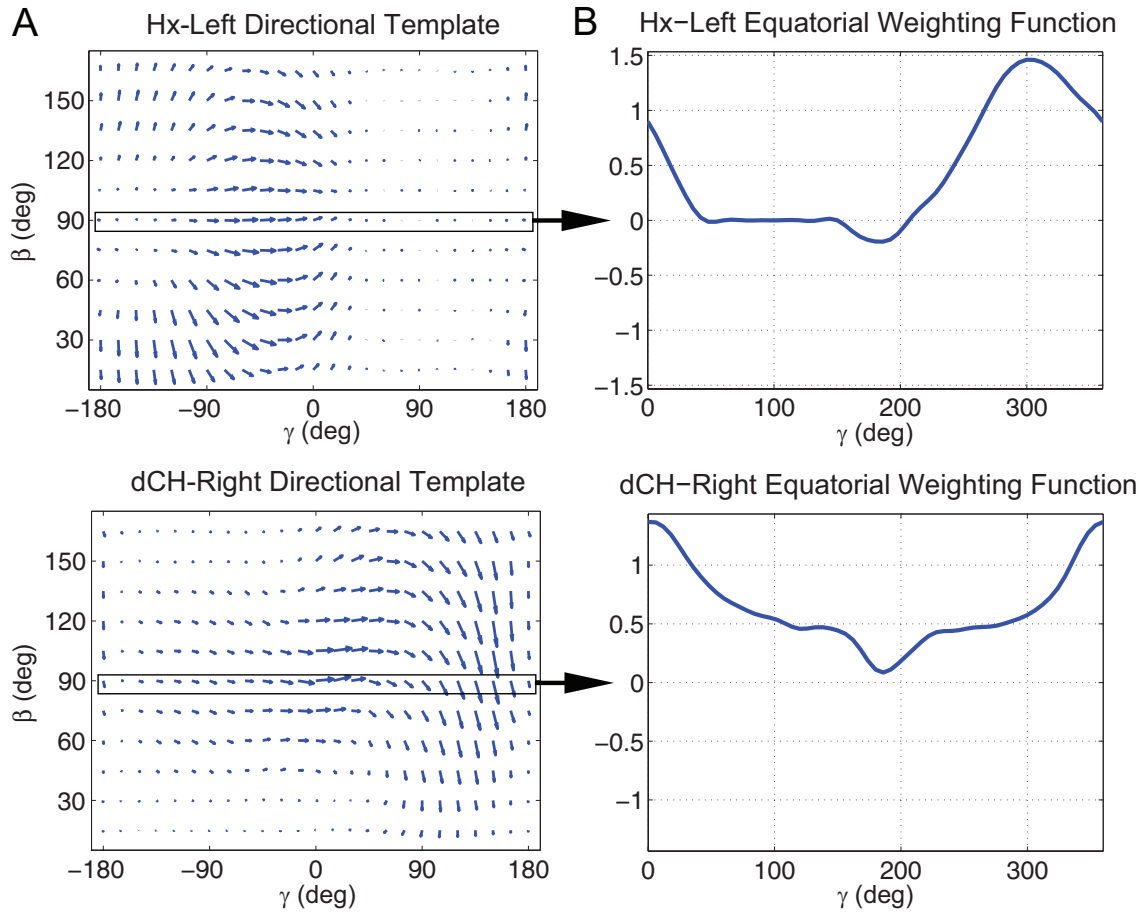
Figure 5.3: Extraction of equatorial-azimuthal flow sensitivity for a left and right hemisphere tangential cell; (A) 2-D directional templates (data extracted and re-plotted from [1, 2, 3]), (B) azimuthal flow component for equatorial ring.

pattern of optic flow induced on the retina for centered motion between two large obstacles (the yaw-plane infinite tunnel environment parameterized in Table 2.1, with $\theta = \phi = 0$). This optic flow pattern corresponds to an equilibrium state of $\mathbf{x}_0 = (y_0, \psi_0, u_0, v_0, \dot{\psi}_0) = (0, 0, u_{\mathrm{ref}}, 0, 0)$. The resulting observation equation $\mathbf{y} = C\mathbf{x}$ is given by

$$
\begin{pmatrix}
H1_R \\
H1_L \\
H2_R \\
H2_L \\
Hx_R \\
Hx_L \\
HSN_R \\
HSN_L \\
HSE_R \\
HSE_L \\
HSS_R \\
HSS_L \\
dCH_R \\
dCH_L \\
vCH_R \\
vCH_L
\end{pmatrix}
=
\begin{pmatrix}
-0.50 & -0.09 & -0.49 & 0.09 & 1.00 \\
0.50 & 0.09 & -0.49 & -0.09 & -1.00 \\
-0.31 & -0.17 & -0.30 & 0.17 & 0.87 \\
0.31 & 0.17 & -0.30 & -0.17 & -0.87 \\
-0.48 & -0.19 & -0.47 & 0.19 & 0.86 \\
0.48 & 0.19 & -0.47 & -0.19 & -0.86 \\
0.46 & 0.11 & 0.25 & -0.11 & -1.11 \\
-0.46 & -0.11 & 0.25 & 0.11 & 1.11 \\
0.56 & 0.11 & 0.24 & -0.11 & -1.21 \\
-0.56 & -0.11 & 0.24 & 0.11 & 1.21 \\
0.28 & 0.23 & 0.23 & -0.23 & -0.83 \\
-0.28 & -0.23 & 0.23 & 0.23 & 0.83 \\
0.56 & 0.14 & 0.05 & -0.14 & -1.25 \\
-0.56 & -0.14 & 0.05 & 0.14 & 1.25 \\
0.59 & 0.08 & 0.13 & -0.08 & -1.26 \\
-0.59 & -0.08 & 0.13 & 0.08 & 1.26
\end{pmatrix}
\mathbf{x}, \qquad (5.1)
$$

where $\mathbf{x} = (\frac{u_0}{a^2} y, \frac{u_0}{a} \psi, \frac{1}{a} u, \frac{1}{a} v, \dot{\psi})$ defines the state relative to the environment.

Inspection of (5.1) reveals that the cell output signals are functions of speed/depth quantities, due to the nature of optic flow. The generated outputs are highly coupled and no one cell weighting appears to provide direct measurement of any particular speed/depth quantity as they have been parameterized. However, it is clear that a relative forward speed estimate $\frac{1}{a} u$ can be obtained by summing the outputs of two same-type cells from opposite hemispheres due to their symmetric sensitivity.

5.1.2 Static TC Output Feedback

From (5.1) it is not obvious how one could wire amplified TC output signals to create stabilizing flight actuator commands. As shown in Chapter 3, the gain selection task for a given set of tangential cell weighting patterns can be cast in a rigorous framework in which traditional tools from control and information theory can be leveraged to achieve the desired closed loop visual-based behaviors. Section 5.1.3.1 applies this process to a planar vehicle.

5.1.3 Experimental Validation

In the following section the methodology for achieving reflexive navigation behavior based on tangential cell outputs is experimentally demonstrated on a wheeled vehicle (see 4.1.1.3 for details of the platform).

5.1.3.1 Feedback Synthesis

The angular velocity input u_r is intended to generate commands to reflexively maneuver the vehicle between objects in the surrounding environment. Following (3.6), the output feedback is implemented as $u = \tilde{K}\tilde{\mathbf{y}}$ where gains $\tilde{K} = KC^\dagger$ are applied to outputs

$$\tilde{y}_i(\mathbf{x}) = \Delta\gamma \sum_{j=1}^{\mathcal{K}} \dot{Q}(\gamma_j, \mathbf{x}) \, F_{y_i}(\gamma_j), \qquad (5.2)$$

which are computed from the $\mathcal{K}$ instantaneous measurements of optic flow $\dot{Q}$ and the fixed set $\mathbf{F_y} = \{F_{y_i}(\gamma_j), \ i = 1, \dots, M\}$ of tangential cell weightings.

To select the inversion $C^\dagger$, several sets of weightings are considered for comparison: (a) feedback based on 4 TC weighting patterns selected to maximize Fisher information in the absence of noise statistics (i.e., least squares (LS) estimates), (b)
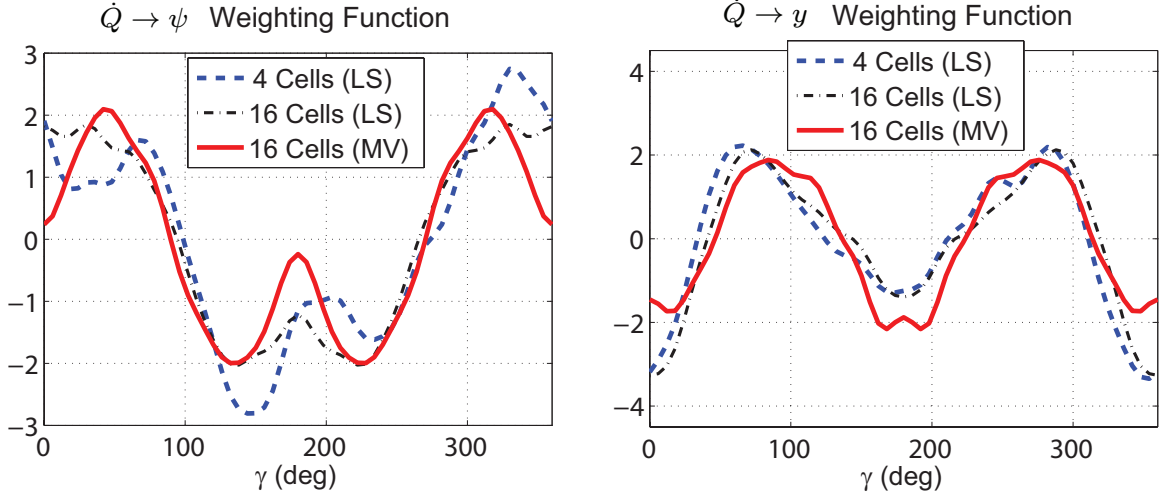
Figure 5.4: State extraction pattern $\mathbf{F_{\hat{x}}} = C^{\dagger}\mathbf{F}$ comparison for control-relevant states and three different tangential cell weighting function set selections.

feedback of all 16 TCs using the least squares estimates ($R_{\mathbf{w}} = I$), and (c) feedback of all 16 TCs using the minimum variance (MV) estimates ($R_{\mathbf{w},ij} = \Delta\gamma \, \sigma_{\eta}^2 \, \langle F_{y_i}, F_{y_j} \rangle$, simplified from the full sphere version (3.15)). The resulting state extraction patterns $\mathbf{F_{\hat{x}}} = C^{\dagger}\mathbf{F_y}$ are plotted in Fig. 5.4. The 4 cell case represents the minimum number of TCs required to guarantee C is full rank, and hence existence and uniqueness of a solution to (3.7). Note that the sideslip velocity $v = 0$ for a wheeled vehicle. If this were not the case then out-of-plane optic flow measurements and a pattern with out-of-plane sensitivity would be required to maintain full rank of the measurement model.

The chosen state feedback matrix is $K = [K_y, K_\psi, 0, 0]$, and the ratio of gains $K_y : K_\psi$ for the trials shown was selected to be $2.25 : 1$ to balance closed loop overshoot and rise time. This results in gains at the tangential cell level presented in Table 5.1. Equivalently, the same feedback could be implemented with a single weighting pattern $u = \langle \dot{Q}, F_u \rangle$ (Fig. 5.5) that represents a direct mapping between optic flow sensors and the angular velocity command.

$\dot{Q} \rightarrow u$ Weighting Function
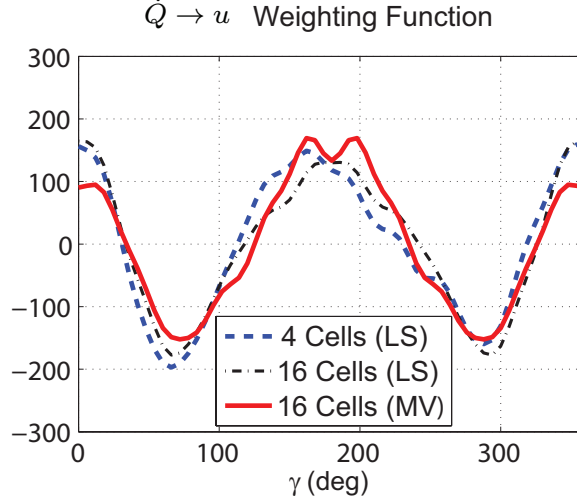
Figure 5.5: Direct optic flow to actuator pattern $\mathbf{F_u} = KC^{\dagger}\mathbf{F_y}$ comparison for three different tangential cell weighting function set selections.

5.1.3.2 Results

The closed loop implementation was tested in two environments; a bent corridor (Fig. 4.5A), and a cluttered field of large obstacles (Fig. 5.6). In the cluttered environment two different initial conditions are used to evaluate performance. Trials were repeated 10 times.

Fig. 5.7A-C shows that the vehicle successfully navigates the tunnel environment using all three inversions. The only clear trend is that 4-cell LS feedback avoids overshoot during the initial condition recovery and executes a sharper turn at the 90° bend. The reason is that the 4-cell feedback is fundamentally biased toward detecting off-nominal flow on the front-left and rear-right of the vehicle (see the ψ sensitivity function asymmetry in Fig. 5.4). During the initial recovery, the presence of the 90° bend downrange causes reduced optic flow on the vehicle's front-right. The robot does not respond to the optic flow perturbation, due to reduced sensitivity in this region, and reacts as if it were in a straight corridor. Implementation of the 16-cell feedback (symmetric state sensitivity functions) demonstrates that the optic flow perturbation leads to a reduced ψ-estimate which causes overshoot in the centering behavior.
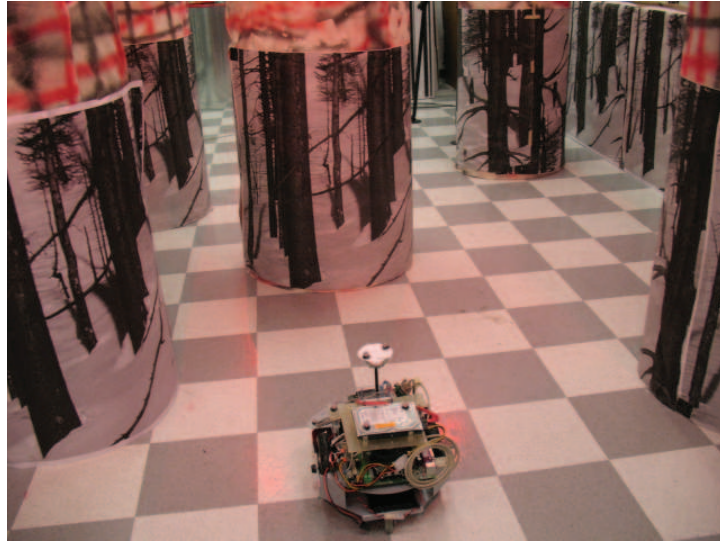
Figure 5.6: Cluttered obstacle field environment.
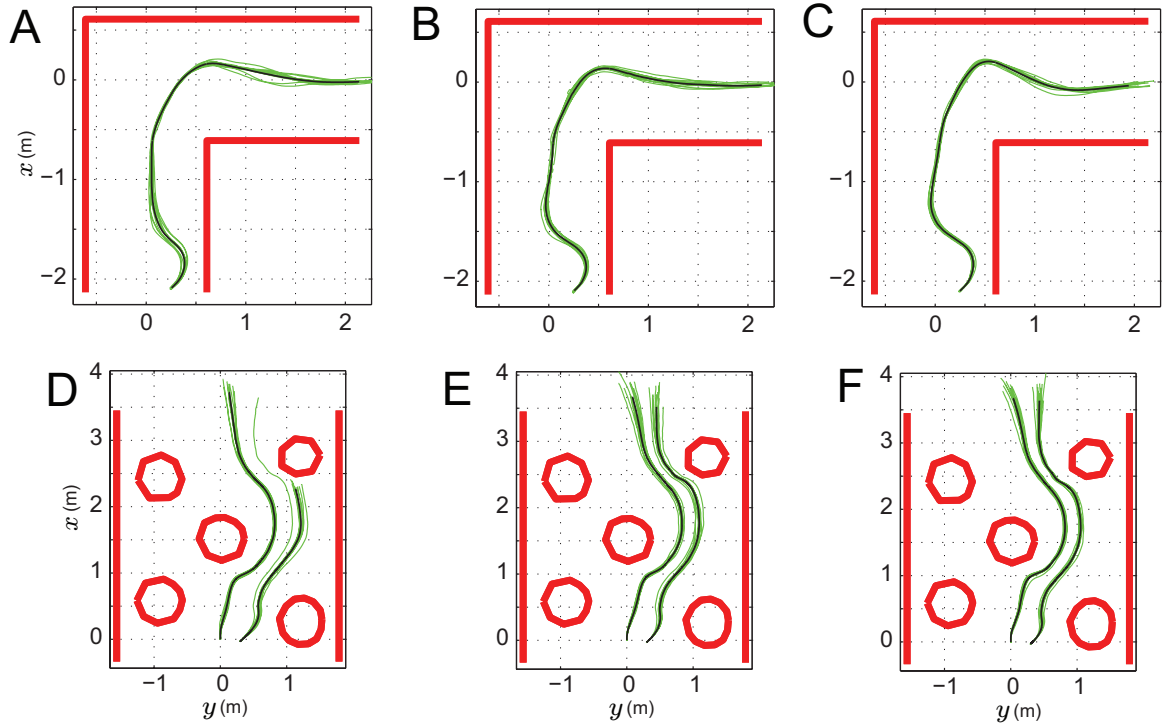
Figure 5.7: Vehicle trajectories (10 trials) and mean trajectory for tunnel with 90°
bend and a cluttered obstacle field (forward speed $u_0 = 0.4$ m/s); tangential cell
gains determined from (A,D) 4-cell LS, (B,E) 16-cell LS, (C,F) 16-cell MV

Table 5.1: Tangential cell feedback gains $\tilde{K}$ for rotation rate control, using Fig. 3.1B control loop architecture

Cell Pattern	4-Cell LS	16-Cell LS	16-Cell MV
H1$_R$		42	371
H1$_L$		-42	-371
H2$_R$		-66	-40
H2$_L$		66	40
Hx$_R$	-287	226	212
Hx$_L$	229	-226	-212
HSN$_R$		78	-22
HSN$_L$		-78	22
HSE$_R$		9	-167
HSE$_L$		-9	167
HSS$_R$		35	-84
HSS$_L$	-232	-35	84
DCH$_R$		11	729
DCH$_L$		-11	-729
VCH$_R$	199	32	-73
VCH$_L$		-32	73

Results for the cluttered object field environment are shown in Fig. 5.7D-F. The bias in the 4-cell feedback is evident in the initial condition starting at $y = 0.3$ m (Fig. 5.7D), but with adverse effects. Due to this bias the vehicle fails to avoid the final right-side cylinder in time, resulting in impact in 9 of the 10 trials. This underscores the importance of including symmetric pairs of weighting functions in the decomposition of optic flow patterns to realize a symmetric mapping between optic flow measurements and actuator response.

For all the cases demonstrated, the variance in trajectories is small, and comparable between weighting function sets. This is due to the similar noise reduction and throughput properties of the weighting functions as quantified by the Fisher information (3.2.2.3). Table 5.2 lists the computed value of $\|P\| = \|\mathsf{F}^{-1}\|$ for a given weighting function set relative to the value $\|P_{\mathrm{opt}}\|$ that would be obtained using a set of functions that fully span $L_2[0, 2\pi]$. Inclusion of the additional 12 tangen-

tial cell measurements in the feedback loop only reduces the noise throughput by a factor of 2/3. The span of the 16 cell measurement set is apparently sufficiently large to capture the range of perturbations in the optic flow pattern for the selected environments, and therefore the state estimate covariance is virtually identical to that achievable if one had access to an infinite set of linearly independent sensitivity patterns.

Table 5.2: Minimum estimate covariance (relative to the global optimum) as a function of WFI weighting pattern set

Weighting Set	$\bar{\sigma}(P)/\bar{\sigma}(P_{\mathrm{opt}})$
Infinite Span of $L_2[0, 2\pi]$	1.000
16 Tangential Cells	1.033
4 Tangential Cells	1.526

The Fisher information is also instructive for the analysis of performance in terms of the extent of the field of view. Table 5.3 plots the computed value of $\|P\|$ relative to the value $\|P_{360°}\|$ that would be obtained using a full 360° FOV. It is evident that the noise throughput is dramatically increased when the FOV is restricted. Hence, the reduction of noise throughput is a possible rationale for the coupling between adjacent vertical system (VS) cells [80] to increase a cell's effective FOV. The importance of a wide FOV for robust information extraction has been well studied [28].

Table 5.3: Minimum estimate covariance as a function of field of view

FOV°	$\bar{\sigma}(P)/\bar{\sigma}(P_{360°})$
360.0	1.0
180.0	9.2
90.0	2.0×10^2
45.0	6.1×10^3
22.5	1.9×10^5

5.1.4 Discussion

The mathematical tangential cell analogue demonstrates how stabilizing feedback gains can be synthesized for any set of M linearly independent tangential cell weighting patterns, providing that $M \geq n$ where n is the number of explicit states in the optic flow model. Furthermore, the patterns required to achieve specific visual-based navigation are not unique; similar behaviors can be achieved with quite different sets of weighting functions (Table 5.1). Hence, the only requirement on selection of weighting function sets is that they are sufficiently different (independent) from one another (a large collective span). This is closely related to recent results from the field of signal compression and reconstruction, where the most efficient method of signal encoding is to use random basis functions if one has no prior model for the signal [81].

The findings in Section 5.1.1 help explain results from similar studies involving use of tangential cells for estimation and control. State estimation was investigated in [36], who suggested using a summation of same-type horizontal cell outputs for forward speed estimation, and subtraction of same-type outputs for yaw rate or sideslip. These claims are supported by inspection of (5.1). However, in [36] the results were limited to unweighted two-cell signal combinations, which essentially constitutes inversion of a non-full rank measurement set. No method is proposed for decoupling yaw rate from sideslip, or from the proximity and orientation states that are also embedded in the subtraction-method output signal. The visuomotor analogue presented here provides a rigorous methodology for using tangential cell weighting properties in closed loop feedback.

Closed-loop control was investigated in [46], where obstacle avoidance was attempted in simulation using a comparison of the left and right HSE cell outputs. While this was useful for obstacle detection during periods of non-rotation, it was unsuccessful when applied as continuous feedback because the subtracted HSE signal

contains coupled measurements of multiple states. The actuator signal should indeed include these quantities (yaw rate, sideslip, proximity and orientation), but they need to be fused using appropriate stabilizing gains rather than in the inherent ratios of the HSE pattern. Although in [46] a hi-fidelity neuronal-based model for the wide-field integration was used, the primary information throughput remains the same.

5.2 2-D Tangential Cell Directional Templates

In this section the 2-D WFI operator (2.17) is used to analyze the full spherical tangential cell directional templates with respect to the information they provide about the dynamical system of the insect. The hypothesis that tangential cells encode the fundamental dynamics modes is investigated by correlating the cell directional templates with the optic flow induced by modal motion.

The response of a system to an arbitrary excitation can always be expressed as a summation of its fundamental modal responses. Since these modal motions will dominate the flight behavior of an insect, it has been hypothesized that insects align their sensors to sense the modes directly [3]. To examine this claim, a rigid body dynamics model of a hovering *Drosophila* (fruit fly) is employed, obtained in [82, 83] by system identification of a hi-fidelity non-linear flapping model. The identified model is linear for small perturbations about hover, contains embedded haltere feedback to augment stability, and assumes that lateral and longitudinal dynamics are decoupled. The natural modes of the state space system $\dot{\mathbf{x}} = A\mathbf{x} + B\mathbf{u}$ are found from the eigenvectors of A, and they determine the behavior of the unforced system ($\mathbf{u}$=0); The eigenvectors specify the direction in state space that the insect moves when a particular mode is excited, and the eigenvalue contains information about the stability of the mode. Also of interest is the state space direction in which

the system is forced by each actuator input, and these can be determined directly from the columns of B. The natural and input modes are summarized in Tables 5.4 and 5.5; note that proximity quantities are absent from the modes because such information is not encoded by optic flow in the hover case (due to low translational velocities).

Table 5.4: Longitudinal *Drosophila* dynamics modes (SI units) in hover condition

Mode Name	θ	u	w	q	Eigenvalue
NATURAL MODES					
Longitudinal Oscillatory	-0.0251	0.0541		0.9948	-3.51
	±0.0805i	±0.0205i			±11.26i
Fast Longitudinal Subsidence	-0.0259	-0.0097		0.9996	-38.56
Slow Heave			1.0000		-4.65
INPUT MODES					
Stroke Amplitude			-1.0000		
Stroke Plane Angle		0.0073		-1.0000	
Wing Oscillation Center		0.0021		1.0000	

Table 5.5: Lateral *Drosophila* Dynamics Modes (SI units) in hover condition

Mode Name	ϕ	v	p	r	Eigenvalue
NATURAL MODES					
Roll/Yaw Subsidence	0.0012	-0.0001	-0.2114	0.9774	-170.89
Roll/Yaw Oscillatory	0.0010	-0.0027	0.1430	0.9886	-3.74
	±0.0067i	±0.0012i	±0.0467i		±22.03i
Yaw Subsidence	-0.0002		0.0180	-0.9998	-79.31
INPUT MODES					
Stroke Amplitude Diff.		0.0007	-1.0000		
Stroke Plane Diff.				-1.0000	

The optic flow induced by a particular mode of motion can be determined by setting the state $\mathbf{x}$ to the applicable modal vector $\mathbf{v}$ from Table 5.4 or 5.5 and applying the algebraic model (2.3), assuming a form for the environment; 1 m sphere

assumed here (a simplification of (2.15)). Oscillatory modes contain complex components, but these are ignored in determining the mode-induced optic flow patterns, Fig. 5.8, as they do not affect the state space motion direction.

If tangential cell outputs are indeed tuned to provide direct static measurements of natural and/or input modes, there should be strong correlation between the TC directional templates $\mathbf{F}_{y_j}$ (Figs. 5.1 and 5.2) and the mode-induced optic flow patterns $\mathbf{F}_{v_i}$ (Fig. 5.8). This comparison can be quantified with the 2-D WFI operator, by performing a spatial inner product between the two patterns on $L^2(S^2, \mathbb{R}^2)$. The absolute value of the scalar output gives an indication of the correlation C_{ji} between the patterns;

$$\mathsf{C}_{ji} = |\langle \mathbf{F}_{v_i}, \mathbf{F}_{y_j} \rangle|. \tag{5.3}$$

Patterns $\mathbf{F}$ are pre-normalized such that their auto-correlation is unity, i.e., $\langle \mathbf{F}_k, \mathbf{F}_k \rangle = 1$. Due to linearity of the WFI operator, (5.3) is equivalent to a normalized vector dot product between row j of the observation matrix C (i.e., $\mathbf{c}_j^T$) and the modal vector v_i;

$$\mathsf{C}_{ji} = N_i |\mathbf{c}_j \cdot \mathsf{v}_i|, \tag{5.4}$$

where N_i is the factor used to normalize the $\mathbf{F}_{v_i}$ pattern and $\mathbf{c}_j$ comprises the linearized information embedded in tangential cell output y_j obtained via an inner product between the optic flow model and the TC directional template, $y_j = \langle \dot{\mathbf{Q}}, \mathbf{F}_{y_j} \rangle$. Eq. (5.4) is the standard method of checking if mode i is observable with measurement j. If $\mathsf{C}_{ji} = 0$ the mode is not observable from the particular tangential cell output. If $\mathsf{C}_{ji} = 1$, the tangential cell directional template is perfectly tuned to provide a direct measurement of the mode. Table 5.6 lists the computed
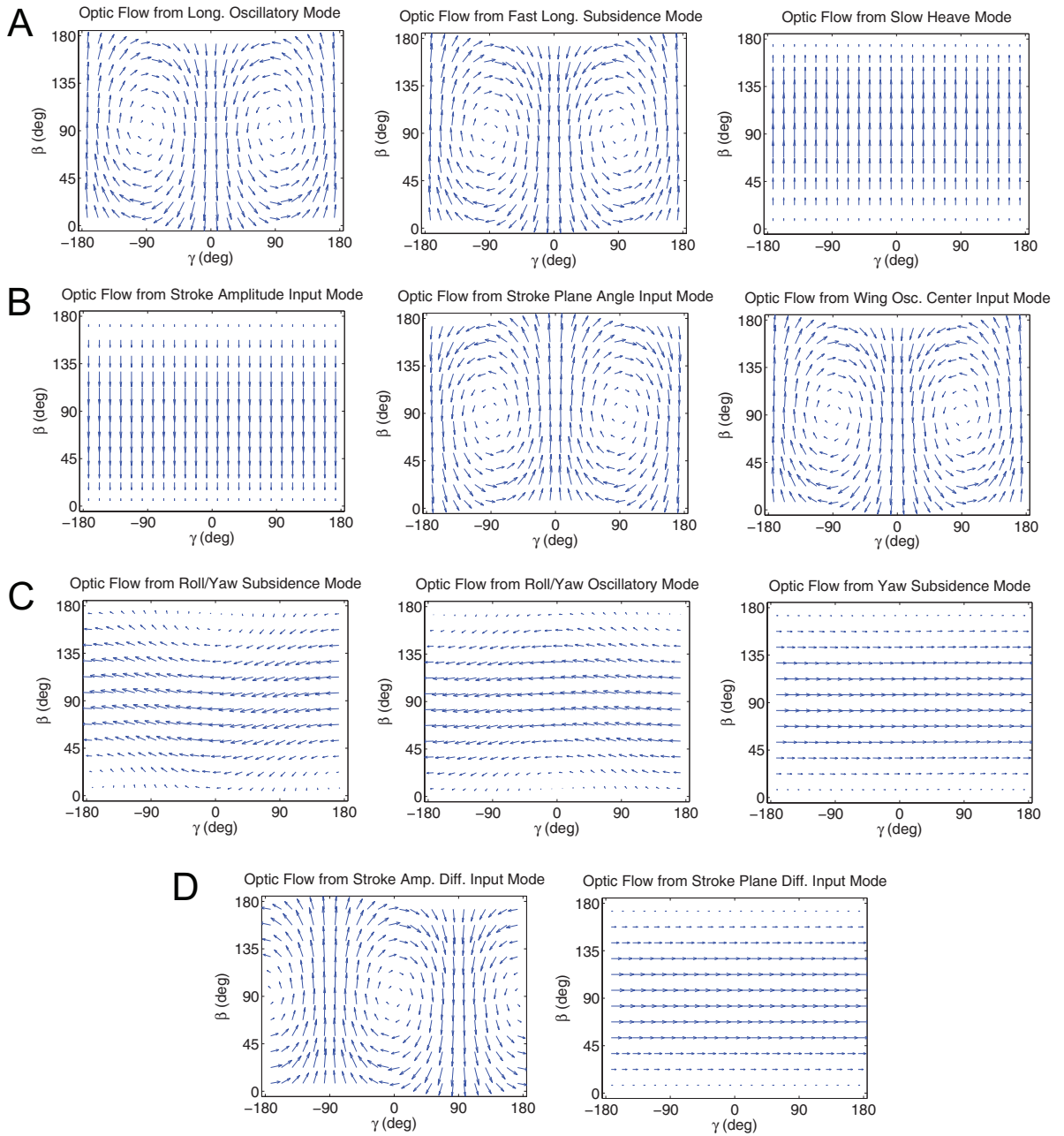
Figure 5.8: Optic flow patterns induced by natural mode motion and input excitation modes; dynamics model: *Drosophila* in hover condition; environment model: sphere, 1 m radius. (A) Longitudinal natural modes, (B) longitudinal input excitation modes, (C) lateral natural modes, (D) lateral input excitation modes.

correlations.

Table 5.6: Spatial inner product between tangential cell directional templates and optic flow pattern induced by natural mode motion and input excitation modes.

Legend:
- 0.75 – 1.00
- 0.50 – 0.75
- 0.25 – 0.50
- 0.00 – 0.25

	LONG. MODES			LONG. INPUTS			LAT. MODES			LAT. INPUTS	
	Long. Osc.	Fast Long. Sub.	Slow Heave	Stroke Amp.	Stroke Plane Angle	Wing Osc. Center	Roll / Yaw Sub.	Roll / Yaw Osc.	Yaw Sub.	Stroke Amp. Diff.	Stroke Plane Diff.
H1	0.02	0.05	0.09	0.09	0.05	0.05	0.68	0.66	0.68	0.09	0.68
H2	0.03	0.06	0.07	0.07	0.05	0.05	0.62	0.61	0.63	0.05	0.63
Hx	0.06	0.03	0.02	0.02	0.03	0.04	0.55	0.53	0.55	0.08	0.54
HSN	0.17	0.19	0.05	0.05	0.19	0.19	0.70	0.73	0.73	0.07	0.73
HSE	0.01	0.03	0.13	0.13	0.02	0.02	0.82	0.80	0.82	0.08	0.82
dCH	0.28	0.29	0.33	0.33	0.29	0.29	0.62	0.71	0.68	0.25	0.68
vCH	0.31	0.30	0.26	0.26	0.30	0.30	0.75	0.64	0.70	0.33	0.70
V1	0.57	0.58	0.42	0.42	0.58	0.58	0.17	0.02	0.09	0.42	0.08
VS1	0.57	0.59	0.40	0.40	0.59	0.59	0.30	0.25	0.27	0.15	0.27
VS2	0.49	0.50	0.52	0.52	0.50	0.50	0.08	0.02	0.02	0.27	0.02
VS3	0.44	0.45	0.54	0.54	0.45	0.45	0.07	0.05	0.00	0.35	0.00
VS4	0.10	0.10	0.62	0.62	0.10	0.10	0.15	0.08	0.03	0.64	0.01
VS5	0.09	0.09	0.62	0.62	0.09	0.09	0.13	0.09	0.01	0.65	0.00
VS6	0.03	0.03	0.59	0.59	0.03	0.03	0.05	0.19	0.08	0.66	0.10
VS7	0.33	0.33	0.52	0.52	0.33	0.33	0.03	0.18	0.09	0.57	0.10
VS8	0.51	0.52	0.39	0.39	0.52	0.52	0.04	0.20	0.13	0.46	0.14
VS9	0.53	0.54	0.44	0.44	0.54	0.54	0.08	0.06	0.00	0.39	0.01
VS10	0.56	0.58	0.41	0.41	0.58	0.57	0.05	0.18	0.12	0.35	0.13

It is clear from Table 5.6 that all the modes are indeed observable via the tangential cell output set. This also follows from the fact that C is full rank, therefore the current state can be determined instantaneously from a single measurement vector $\mathbf{y}$. Some cells do appear to be tuned well to sense particular modes, but there is also significant residual components from other modes. As discussed in Section 5.1.4, the directional template symmetry of contralateral same-type cells can be utilized to isolate translational from rotary motion or longitudinal from lateral motion. By positively combining same-type right and left hemisphere cell outputs, measurement correlation with longitudinal modes is improved and the lateral mode components are completely filtered out (Table 5.7). By negatively combining outputs, the reverse effect is acheived (Table 5.8).

Table 5.7: Spatial inner product between positively combined (right plus left hemisphere, normalized) tangential cell directional templates and optic flow pattern induced by natural mode motion and input excitation modes.

	0.75 − 1.00 0.50 − 0.75 0.25 − 0.50 0.00 − 0.25	LONG. MODES			LONG. INPUTS			LAT. MODES			LAT. INPUTS	
		Long. Osc.	Fast Long. Sub.	Slow Heave	Stroke Amp.	Stroke Plane Angle	Wing Osc. Center	Roll / Yaw Sub.	Roll / Yaw Osc.	Yaw Sub.	Stroke Amp. Diff.	Stroke Plane Diff.
H1 (R+L)		0.03	0.08	0.14	0.14	0.08	0.07	0.00	0.00	0.00	0.00	0.00
H2 (R+L)		0.05	0.10	0.13	0.13	0.09	0.09	0.00	0.00	0.00	0.00	0.00
Hx (R+L)		0.10	0.04	0.03	0.03	0.05	0.05	0.00	0.00	0.00	0.00	0.00
HSN (R+L)		0.37	0.42	0.12	0.12	0.42	0.41	0.00	0.00	0.00	0.00	0.00
HSE (R+L)		0.02	0.07	0.36	0.36	0.07	0.06	0.00	0.00	0.00	0.00	0.00
dCH (R+L)		0.57	0.59	0.68	0.68	0.59	0.59	0.00	0.00	0.00	0.00	0.00
vCH (R+L)		0.64	0.63	0.54	0.54	0.63	0.63	0.00	0.00	0.00	0.00	0.00
V1 (R+L)		0.71	0.72	0.53	0.53	0.72	0.72	0.00	0.00	0.00	0.00	0.00
VS1 (R+L)		0.64	0.66	0.44	0.44	0.66	0.66	0.00	0.00	0.00	0.00	0.00
VS2 (R+L)		0.55	0.56	0.58	0.58	0.56	0.56	0.00	0.00	0.00	0.00	0.00
VS3 (R+L)		0.53	0.54	0.65	0.65	0.54	0.54	0.00	0.00	0.00	0.00	0.00
VS4 (R+L)		0.14	0.14	0.87	0.87	0.14	0.14	0.00	0.00	0.00	0.00	0.00
VS5 (R+L)		0.12	0.13	0.89	0.89	0.13	0.13	0.00	0.00	0.00	0.00	0.00
VS6 (R+L)		0.04	0.04	0.84	0.84	0.04	0.04	0.00	0.00	0.00	0.00	0.00
VS7 (R+L)		0.46	0.47	0.74	0.74	0.47	0.47	0.00	0.00	0.00	0.00	0.00
VS8 (R+L)		0.69	0.70	0.53	0.53	0.70	0.70	0.00	0.00	0.00	0.00	0.00
VS9 (R+L)		0.70	0.71	0.58	0.58	0.71	0.71	0.00	0.00	0.00	0.00	0.00
VS10 (R+L)		0.73	0.74	0.52	0.52	0.74	0.74	0.00	0.00	0.00	0.00	0.00

From Table 5.7, $VS5_\mathsf{R} + VS5_\mathsf{L}$ encodes the slow heave mode best, whilst $VS10_\mathsf{R} + VS10_\mathsf{L}$ encodes the remainder of the longitudinal modes, which are dominated by pitch-axis rotation. These conclusions are intuitive from visual inspection of the cell directional templates (Fig. 5.2). Table 5.8 shows that $H1_\mathsf{R} - H1_\mathsf{L}$ best encodes the bulk of the lateral modes (dominated by yaw-axis rotation), whilst $VS6_\mathsf{R} - VS6_\mathsf{L}$ best encodes the stroke amplitude differential input mode (dominated by roll-axis rotation). The VS cells exhibit a clear trend in modal correlation, and this is because their directional templates are tuned to rotations about different axes - all close to the equatorial plane [3]; the azimuthal location of the axis varies approximately linearly with the cell number.

It is important to recognize that although the tangential cell patterns correlate well with the mode-induced patterns, the cell outputs do not appear to provide direct

Table 5.8: Spatial inner product between negatively combined (right minus left hemisphere, normalized) tangential cell directional templates and optic flow pattern induced by natural mode motion and input excitation modes.

Legend:
- 0.75 − 1.00
- 0.50 − 0.75
- 0.25 − 0.50
- 0.00 − 0.25

	LONG. MODES			LONG. INPUTS			LAT. MODES			LAT. INPUTS	
	Long. Osc.	Fast Long. Sub.	Slow Heave	Stroke Amp.	Stroke Plane Angle	Wing Osc. Center	Roll / Yaw Sub.	Roll / Yaw Osc.	Yaw Sub.	Stroke Amp. Diff.	Stroke Plane Diff.
H1 (R-L)	0.00	0.00	0.00	0.00	0.00	0.00	0.91	0.87	0.90	0.12	0.90
H2 (R-L)	0.00	0.00	0.00	0.00	0.00	0.00	0.77	0.75	0.77	0.07	0.77
Hx (R-L)	0.00	0.00	0.00	0.00	0.00	0.00	0.73	0.70	0.72	0.11	0.72
HSN (R-L)	0.00	0.00	0.00	0.00	0.00	0.00	0.78	0.82	0.81	0.07	0.82
HSE (R-L)	0.00	0.00	0.00	0.00	0.00	0.00	0.88	0.86	0.88	0.09	0.88
dCH (R-L)	0.00	0.00	0.00	0.00	0.00	0.00	0.71	0.82	0.78	0.29	0.79
vCH (R-L)	0.00	0.00	0.00	0.00	0.00	0.00	0.85	0.73	0.80	0.38	0.79
V1 (R-L)	0.00	0.00	0.00	0.00	0.00	0.00	0.28	0.04	0.15	0.70	0.14
VS1 (R-L)	0.00	0.00	0.00	0.00	0.00	0.00	0.65	0.54	0.60	0.32	0.59
VS2 (R-L)	0.00	0.00	0.00	0.00	0.00	0.00	0.17	0.04	0.05	0.59	0.04
VS3 (R-L)	0.00	0.00	0.00	0.00	0.00	0.00	0.12	0.10	0.00	0.63	0.01
VS4 (R-L)	0.00	0.00	0.00	0.00	0.00	0.00	0.21	0.11	0.04	0.91	0.02
VS5 (R-L)	0.00	0.00	0.00	0.00	0.00	0.00	0.19	0.13	0.01	0.91	0.00
VS6 (R-L)	0.00	0.00	0.00	0.00	0.00	0.00	0.06	0.26	0.12	0.92	0.13
VS7 (R-L)	0.00	0.00	0.00	0.00	0.00	0.00	0.04	0.25	0.12	0.81	0.14
VS8 (R-L)	0.00	0.00	0.00	0.00	0.00	0.00	0.06	0.30	0.20	0.68	0.21
VS9 (R-L)	0.00	0.00	0.00	0.00	0.00	0.00	0.12	0.09	0.00	0.60	0.01
VS10 (R-L)	0.00	0.00	0.00	0.00	0.00	0.00	0.08	0.28	0.19	0.56	0.20

isolated measurements of individual modes, partly due to the fact that some modes are highly coupled. The input excitation modes are also highly coupled to the natural modes, which is logical for control purposes but prevents them from being seperately observed. The analysis technique of Section 3.2.3 could be applied to derive weighting patterns that do output modal measurements, but Tables 5.6-5.8 do not suggest that tangential cells perform this functionality. A post-processing stage would be required to extract modal estimates from the TC outputs if mode-space feedback control is desired. However, as was shown in Section 5.1.3, direct static linear feedback of tangential cell outputs is sufficient to stabilize a vehicle.

The obvious limitation of this study is that we are attempting to correlate the *Drosophila* dynamics modes with *Calliphora* tangential cell data. This is due to the availability of published data, but the fundamental conclusions are unlikely

to change; i.e., system observability and the advantages of combining same-type cell outputs from opposite hemispheres. It should also be noted that the modes determined from the model are dominated by rotation motion. That is, a perturbed *Drosophila* will apparently respond with significant rotation motion but very small translations. The dynamics model has not been confirmed experimentally, thus it is possible that the true modes may induce more translational optic flow, which some tangential cells are better tuned to. If a dynamics model can be obtained for forward flight, then the system modes will also contain proximity and orientation quantities. It is of significant interest to examine how well the tangential cells encode these.

The above limitations prevent absolute conclusions as to the accuracy of the central hypothesis. However, the high correlation values (0.73 - 0.92) between left-right cell combinations and the dynamics modes provides the first mathematically-grounded evidence that tangential cells do deliver (coupled) measurements of fundamental modes. The most important lesson from this Chapter is that any set of WFI weighting patterns, with sufficiently large span, can be used to close the visuomotor loop.

Chapter 6

WFI Algorithm Summary

For archival convenience and clarity, this chapter summarizes the proposed sensor weighting pattern design technique and the real-time implementation of WFI-based control. The concepts developed in Chapters 3 are presented again in a step-by-step recipe format, without the theory, to simplify implementability on future platforms.

The utility of this instruction manual is broader than just a guideline for extracting behaviorally relevant information from spatially-distributed optic flow measurements. It can in fact be applied to any type of distributed sensing array by substituting the optic flow model with a model of the applicable sensor. Other possible applications are electrolocation (detection of objects by perturbation in the electric field) [92] and velocity-field sensing (using arrays of insect-like hair sensors) [93].

6.1 WFI-Based Controller Design

The offline procedure for static linear WFI-based compensator design is given below.

1. Define a set of measurement/grid points spatially distributed over the sphere (or a potentially disconnected subset of the sphere).

2. Define a set of weighting patterns $F_{\mathbf{y}}$ with a preferably large span.

3. Define a parameterized environment model (e.g. (2.10) or (2.15)) and specify the extremum values for the distance/structure parameters.

4. Define a nominal, equilibrium, trajectory $\mathbf{x}_0$.

5. For each extreme environment...

   (a) Use the algebraic optic flow model, with state $\mathbf{x}_0$, to compute the optic flow at each grid point $\dot{\mathbf{Q}}(\mathbf{x}_0, \gamma_k, \beta_k)$.

   (b) For each state x_i...

       i. Perturb the state by a small δ and re-compute optic flow at each grid point $\dot{\mathbf{Q}}(\mathbf{x}_0 + \delta\mathbf{x}_i, \gamma_k, \beta_k)$.

       ii. Element i of the optic flow Jacobian (linearized about x_0), at grid point (γ_k, β_k), is $\dot{\mathbf{Q}}_{\text{lin},x_i}(\gamma_k, \beta_k) = \frac{\dot{\mathbf{Q}}(\mathbf{x}_0 + \delta\mathbf{x}_i, \gamma_k, \beta_k) - \dot{\mathbf{Q}}(\mathbf{x}_0, \gamma_k, \beta_k)}{\delta}$.

       iii. For each weighting pattern $\mathbf{F}_{y_j}$, perform Wide-Field Integration of $\dot{\mathbf{Q}}_{\text{lin},x_i}$ over measurement grid to obtain observation matrix entry $C_{ji} = \langle \dot{\mathbf{Q}}_{\text{lin},x_i}, \mathbf{F}_{y_j} \rangle$. WFI operations should be performed using Eq. (A.9), (A.10), or (A.11) depending on the grid type.

6. Compute C_0 by averaging the C matrices for each extreme environment.

7. Compute the output noise covariance matrix $R_{\mathbf{w}}$ using (3.15) and the model uncertainty penalty matrix $R_{\delta C}$ using (3.17).

8. Compute the mapping of WFI outputs to states, $C^\dagger$, using (3.9).

9. If the task permits flexibility to design weighting patterns freely, the weighting patterns $F_{\hat{\mathbf{x}}}$ that map optic flow measurements to state estimates are obtained with (3.20).

10. Determine which states you wish to include in the feedback loop then use a linear control tool (i.e., output LQR) to design the state feedback gain matrix K.

11. If the task permits flexibility to design weighting patterns freely, the weighting patterns $F_{\mathbf{u}}$ that map optic flow measurements to actuator commands are obtained with (3.5). If not, actuator commands can be produced by control law (3.2) using the original weighting patterns, with output feedback gain matrix $\bar{K} = KC^{\dagger}$.

6.2 Real-time Algorithm Implementation

In real-time, control input formulation requires just $2\mathcal{K}$ multiplications and additions per actuator. If one considers each of the $\mathcal{K}$ optic flow measurement points as a sensor, then the computational requirements of the controller are identical to that of a linear output feedback operation (i.e., a $\mathcal{P} \times 2\mathcal{K}$ matrix multiplication, where $\mathcal{P}$ is the number of actuators). The recommended implementation is outlined below.

1. Pre-load the WFI weighting patterns $\mathbf{F}_j$ (either exact values or reconstructed via a spherical harmonic approximation)

2. Convert to camera-frame Cartesian weightings ${}^{\mathcal{C}}\mathbf{F} = \{F^{x_c}(\gamma, \beta), F^{y_c}(\gamma, \beta)\}$, including corrections for flat camera distortions and optic flow units:

$$\begin{pmatrix} F^{x_c}(\gamma_k, \beta_k) \\ F^{y_c}(\gamma_k, \beta_k) \\ F^{z_c}(\gamma_k, \beta_k) \end{pmatrix} = \frac{r \text{ IMAGEWIDTH}}{2\, x_{c,max} \text{ FPS}} \mathcal{R}_{\mathcal{CB}} \mathcal{R}_{\mathcal{LB}}^T \begin{pmatrix} 0 \\ F^{\beta}(\gamma_k, \beta_k)_j \\ F^{\gamma}(\gamma_k, \beta_k)_j \end{pmatrix}, \quad (6.1)$$

where relevant quantities are defined in Eq. (A.5), (A.1) and (A.8). Note that F^{z_c} can be disregarded.

3. For every frame...

113

(a) Use an analog sensor or digital camera imagery to measure 2-D optic flow at each grid node. If there is a means to identify poor optic flow estimates (i.e., via a cost function) then this can be used to reject outliers by deleting the grid node and computing WFI outputs by real-time least squares inversion (Eq. (A.11)) or by using a finer raw grid and then averaging adjacent blocks of estimates, whilst rejecting outliers, to obtain a coarser grid for the WFI step.

(b) Compute WFI outputs $\langle \dot{Q}, {}^{\mathcal{C}}\mathbf{F}_j \rangle$ using Eq. (A.9), (A.10), or (A.11) depending on the grid type. If (A.11) is used without real-time adjustments to the grid, relevant matrices can be stored prior to the main loop.

(c) Sample other non WFI-based sensors if applicable.

(d) Formulate actuator inputs using (3.1) or (3.2) depending on the type of weighting functions used.

(e) Low-pass filter the actuator commands to reduce sensor to actuator noise throughput.

Chapter 7

Summary and Conclusions

This chapter summarizes key results, compares them to similar studies, and examines the feasibility and limitations of the WFI method. Areas for future work are also identified.

7.1   Feasibility

With regards to hardware availability, existing MAVs are capable of obtaining attitude and angular rate estimates through use of gyros, accelerometers and magnetometers [84]. A pitch or roll sensor is therefore easily attainable, and light-weight sonar sensors are available for measurement of height [84, 75]. Fixed-wing UAVs can also measure forward speed using a Pitot tube. Therefore, the sensor-fusion in the proposed control loops presented in this thesis are hardware-feasible. However, rather than relying on optic flow for the majority of state measurements (as was done in Section 4.2), an improved configuration might employ an on-board inertial measurement unit (IMU) to provide attitude and rate measurements - due to its superior accuracy. The niche for optic-flow-based sensing on MAVs is not accurate state estimation but relative proximity and velocity estimation.

The camera configurations proposed in Section 4.2 are academic but a similar feasible realization is certainly possible (see Section 7.5). Since lower hemisphere measurements are generally sufficient, one could even use a single camera and panoramic mirror [85].

Regarding versatility of the WFI navigation concept, it is important to note that the proposed information-extraction method is not limited to the environment

models presented in this thesis. The simplified models are used only for designing weighting patterns, which are relatively insensitive to the environment assumption; the ellipsoid and infinite tunnel models lead to near-identical optimal weightings. By regulating unwanted asymmetries in the optic flow pattern (perturbations from the equilibrium pattern [68, 3]), the vehicle attempts to track an obstacle-symmetric (centered) path through its world. This is precisely the navigational heuristic observed in honeybees [26] and is a trait independent of environment structure or spacing.

7.2   Limitations

The attractive potential of WFI is its low computational burden and suitability for analog implementation [70]. The disadvantage is that the implementations described in this thesis do not perform well in environments with large areas of poor contrast - a limitation of the dynamic range of modern imaging devices. This could potentially be overcome through use of adaptive analog imaging and/or different optic flow algorithms (i.e., block matching). For this reason, most vision-based navigation studies utilize feature detection/tracking [86, 55], but the associated computational requirements are generally too large for implementation on MAV avionic hardware (i.e., small fixed point processor) at high bandwidth.

Another flaw is the possibility of a collision course into a symmetric obstacle. Fortunately, the chance is small because stability analysis and simulation results show that such trajectories are unstable. There are several close encounters in Fig. 4.13, for example, but when the helicopter becomes near enough, small asymmetries become stronger, enabling an avoidance maneuver prior to impact. Despite exclusion of a front-side wall from the environment model, the designed weighting patterns are still useful in these near-head-on approaches. However, the instances

during symmetric approaches to building walls or corners (which generate minimal optic flow) where proximity becomes unsafe suggest the need for an emergency turn or continuous control capability based on feedback of a WFI-based x (frontal proximity) estimate [87]. Insects avoid such collisions by detecting expansion patterns in the optic flow field and then executing a rapid turn, known as a saccade [25]. This estimate pattern could be derived using the enclosed room environment model (2.10). The inherent limitation is that small obstacles generate high frequency perturbations to the optic flow signal that are filtered out by WFI. For avoidance of such obstacles (i.e., poles and wires), one could implement detection of these high frequency anomalies or make use of a forward-pointing range finding sensor such as sonar [88]. The WFI technique presented in this thesis is suited to avoidance of large obstacles. For detection of small objects, insects make use of different small-field processing mechanisms [89].

One limitation of the analysis and simulations is the assumption that objects in the environment are static. Small moving objects will manifest as colored noise in the optic flow signal, but will be largely filtered out in the WFI process. However, large moving objects may significantly bias the WFI-extracted quantities. In [26] it was shown that Honeybees respond to an adjacent wall moving in the direction of flight by flying closer to it (as the optic flow induced by the wall is reduced). Whilst this did not result in any collisions for the Honeybees, the effect of non-static large objects (e.g. cars) on the navigational stability of the robotic analogues presented in this thesis needs to be studied.

7.3   Comparison with Literature

To compare results with similar studies, the ability to successfully navigate a cluttered field makes this study comparable with [90]. The centering behavior

demonstrated in Fig. 4.13 outperforms the optic-flow-controlled trajectories in [37] because only lateral offset is controlled in that study, instead of offset and orientation (see also the comparison made in Fig. 7.1). Similarly, the terrain-following performance improves on [52, 53] for the same reason, but in the vertical plane. An algorithm developed in [51] potentially offers more robust obstacle avoidance by detecting impingements on a spherical tunnel, but assumes independent knowledge of vehicle motion. [91] contains a highly successful experimental demonstration of the WFI concept on a fixed-wing UAV, mirroring our simulation results, but lacks a formal stability proof and a theoretical basis for weighting pattern selection.

Almost every experimental attempt to use optic flow for obstacle avoidance has employed a WFI approach [37, 38, 39, 42, 43, 44, 45, 48, 49, 50, 52, 53]. Whilst some are successful, none apply any mathematical grounding to the task of sensor to actuator weighting pattern design. A typical approach is to subtract averaged optic flow over a left-side camera from a right-side camera, which is equivalent to a constant magnitude weighting on symmetric subsets of the sphere. The resulting weighting pattern is intuitive, but the WFI output will embed yaw rotation rate, which overshadows any indication of obstacle proximity and can destabilize the vehicle. Even with the rotation component artificially removed, the benefits of utilizing the theoretically justified approach developed in this thesis is clear from Fig. 7.1. The left vs right patch weighting pattern is akin to a DC weighting, which does not encode lateral orientation and therefore creates a stable but undamped centering response. The feedback connection of tangential cell outputs in [46] also constitutes a form of WFI, with an ad hoc sensor to actuator weighting pattern design. However, their experiment also would have been more successful with application of the Section 5.1 methodology.

In terms of motion-estimation and terrain mapping, WFI does not provide explicit information about environment structure, as in [54, 60], but it does enable

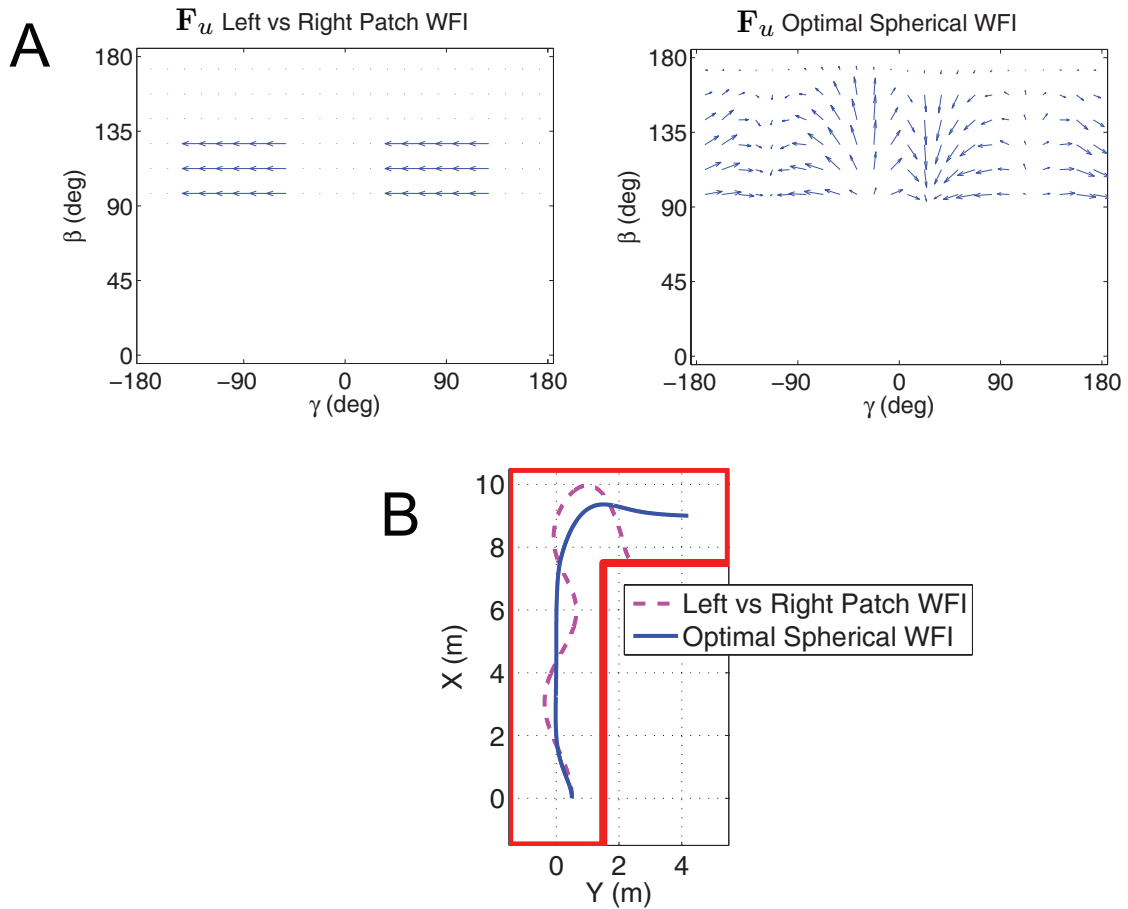Figure 7.1: AVLSim comparison of optimal WFI weighting pattern methodology to a typical left vs right patch comparison scheme (with removal of rotation-component from the optic flow). Measurements are restricted to the upper hemisphere to avoid sensing the floor. (A) Weighting patterns mapping optic flow measurements to rotation rate command, (B) wheeled robot trajectories through a corridor with 90° bend

motion-state extraction with noise-levels and accuracies similar to those reported in [60, 62] and superior to those reported in [54]. Even lower noise is achieved in [55], but high contrast feature tracking is employed, which is computationally expensive. WFI is not an attempt to design the best vision algoritm, but to capitalize on the benefits of vision-based servoing within the extreme computational/payload constraints of minature air vehilces.

7.4 Conclusions

This thesis provides an important link between an insect's neurophysiology and its behavioral heuristics. By application of information theory it is shown what tangential cells may be encoding, and through linear controller design it is shown how an analogue to tangential cells can be used to stabilize a vehicle. This is the first effort to mathematically link the properties of the insect visuomotor system to the impressive flight behaviors we see everyday. More importantly, it shows how the biological concept of converging massive noisy sensor arrays to a handful of flight commands can be transitioned to 6-DOF engineered platforms.

The outcome of this thesis is a mathematical analogue to tangential cells which can be directly applied to 6-DOF vehicles for robust obstacle avoidance and stability augmentation. The approach presented here is not an attempt to precisely model the feedback interconnections within insects; rather, it seeks to characterize the fundamental operational principle within a mathematical framework for transition to engineered systems. Specifically, it is shown that the resulting feedback synthesis task can be cast as a combined static state estimation and linear feedback control problem. Additionally, the framework described herein provides a theoretically justified methodology for analysis and design of direct mappings between optic flow measurements and actuator commands, which greatly simplifies implementation on

robotic platforms [70]. The techniques developed in this thesis can be directly utilized for compensator design with any distributed sensing array type.

A list of key results from the thesis is presented below:

Chapter 2

1. Using an algebraic approximation of simple 3-D worlds, one can predict what information is encoded in spatial patterns of optic flow. This allows us to apply mathematical techniques to design weighting patterns that decode relevent information from optic flow measurements.

Chapter 3

2. The task of designing WFI weighting patterns that linearly map a distributed sensor array to actuator commands can be cast as a combined static state estimation and linear feedback control problem. This allows incorporation of robustness to noise, model uncertainty and dynamic performance objectives into the static weighting patterns. Existence of solution is guaranteed if all applicable constraints of the state feedback gain technique are satisifed and if the initial trial set $F_{\mathbf{y}}$ contains $m \geq n$ linearly independent weighting patterns such that the matrix of inner products between the weighting patterns and the optic flow model Jacobian elements is full rank.

Chapter 4

3. A perturbation optic flow pattern, which is superimposed on the nominal pattern when a state deviates from the nominal trajectory, is not necessarily orthogonal to patterns induced by other states. This is also true when the dynamics are transcribed to modal form. The static state extraction step in the weighting pattern design process removes the effects of non-orthgonality, filtering out information from unwanted states. However, the final weighting pattern set is not necessarily orthogonal.

4. For an infinite planar tunnel, it was shown (for a wheeled robot) that the closed-loop WFI output feedback system is large-perturbation stable about a centered trajectory, with non-linear dynamics and outputs. The guaranteed stability region approaches that of the entire tunnel as the lateral offset feedback gain becomes small and the ratio of the two gains becomes large.

5. By parameterizing a simple 3-D environment, and computing the observation matrix $C_{\hat{\mathbf{x}}}$ for all reasonable combinations of environment dimensional parameters, it was shown (for a fixed-wing UAV and a micro helicopter) that the closed-loop WFI output feedback system is small-perturbation stable about a centered trajectory for the entire family of modeled environments.

6. Different navigational behaviors (e.g. hover, landing, wall hug, centering) can be acheived rapidly during flight by adjusting the target state. This mode switch may also need to be accompanied with gain adjustment.

7. Experiments on a ground robot showed that WFI-based obstacle avoidance was robust to initial conditions, optic flow measurement noise, and environment structure. Test failures, not shown here, only resulted during head-on approaches to small obstacles (see discussion of limitations, Section 7.2).

8. Experiments on a micro quadrotor with 1-D WFI demonstrated that undesirable performance constraints arise from side-slip motion when optic flow measurements are limited to the equatorial circle. This follows from small-perturbation stability analysis, and provides motivation for using 2-D WFI on an increased measurement domain.

9. Optic flow measurements from three orthogonal planes provide sufficient data to extract all proximity and motion states reliably via WFI. However, optic flow measurements over the full sphere maximize robustness with respect to

measurement noise.

10. Monte Carlo simulations of a micro helicopter in an urban-like environment verified closed-loop robustness to environment structure and spacing. From a variety of initial conditions, the vehicle successfully avoided obstacles and terrain anomalies whilst maintaining stable flight. Restriction of measurements to the lower hemisphere reduced obstacle clearance distances but did not compromise stability.

Chapter 5

11. Insect tangential cells do not appear to be tuned to provide isolated measurements of individual motion/proximity states or fundamental dynamics modes, but static output feedback design tools can be applied to generate the same centering and clutter reponses observed in insects.

12. Within the WFI framework, the most important property of the tangential cell directional templates is that their combined span is large, which reduces noise throughput in the visuomotor system.

13. WFI requires a large field of view to keep noise throughput at manageable levels. For lateral fields of view less than 180°, noise throughput increases dramatically.

14. Weighting patterns that map sensors to state estimates or sensors to actuators are not unique. However, there exists a unique optimum given quantifiable objectives such as noise minimization and dynamic performance. This result also applies to stabilizing sets of output feedback gains.

Chapter 6

15. Real-time implementation of WFI-based control requires just four weighted summations of 200 optic flow measurements per control update (for case study

4.2.2). Given the current lack of sensors with suitable mass and bandwidth for MAVs, WFI implementations could provide an attractive alternative for stability augmentation and collision avoidance in the field.

7.5   Future Work

Optic flow is a relative measure, thus the state estimates obtained in this study are generally scaled combinations of speed/depth. In this thesis it has been shown that these quantities are sufficient for regulating a safe optic flow pattern and hence a safe trajectory. One complication of this is that pure WFI-based control will cause the vehicle to regulate a lower altitude when obstacles are tightly spaced. From a safety viewpoint this is undesirable, which is why an independent measurement of $\tilde{z}$ was assumed available in the micro-helicopter study (4.2.2). In contrast, it may be beneficial to link forward speed with lateral obstacle spacing using a weighting-pattern such as that shown in Fig. 2.4A to measure u. This strategy, requiring a reduction in the uncertainty weighting ε, is of significant interest for future studies. Optimality of the weighting patterns is also contigent on the noise covariance matrix $R_{\mathbf{w}}$, and future efforts should apply the stochastic analysis performed in [72] to (3.13) to refine $R_{\mathbf{w}}$.

There are several areas of WFI-related research at the University of Maryland's Autonomous Vehicles Lab where progress has been made but the applicable mechanisms have not yet been formalized. Firstly, it has been shown experimentally that the frontal proximity x estimate can be used to scale the ψ feedback gain to enhance avoidance of obstacles directly in front. However, this non-linear controller has not yet received a formal design/analysis treatment. Secondly, vehicles that require high banking during maneuvres (fixed-wing UAVs) need active rotation of the weighting patterns (or cameras) to keep their visual servoing sensitivities level with

the horizon. Without such compensation, the lateral proximity indicator reacts to the ground during a turn and responds more weakly to actual obstacles. Compensation algorithms have been designed and tested in simulation, but lack any formal analysis. Insects use gaze stabilization, keeping their head level by rotating their necks, and the responsible neuronal mechanisms closely resemble the architecture of the tangential cells [94] analyzed in this thesis. A more rigorous investigation how this concept can be transitioned to MAVs is warranted.

Experimental validation of the 2-D WFI techniques developed in Section 4.2 will soon be possible using Centeye's Multiaperture Optical System (MAOS) (Fig. 7.2). This is a series of 2-D imaging arrays connected to analog VLSI / DSP hybrid chips that perform optic flow computations. These feed to a small micro-processor for the pooling of data and the WFI operations. Coverage of the entire sphere is possible, and this should deliver a large improvement over the yaw-ring WFI used on the quadrotor experiment (4.1.2). It will allow detection of out-of-plane obstacles, decoupling of sideslip motion from the lateral orientation estimate, more reliable estimation of body velocities (without the need for IMU fusion), and reduced noise throughput to the actuators due to a greater field of view.
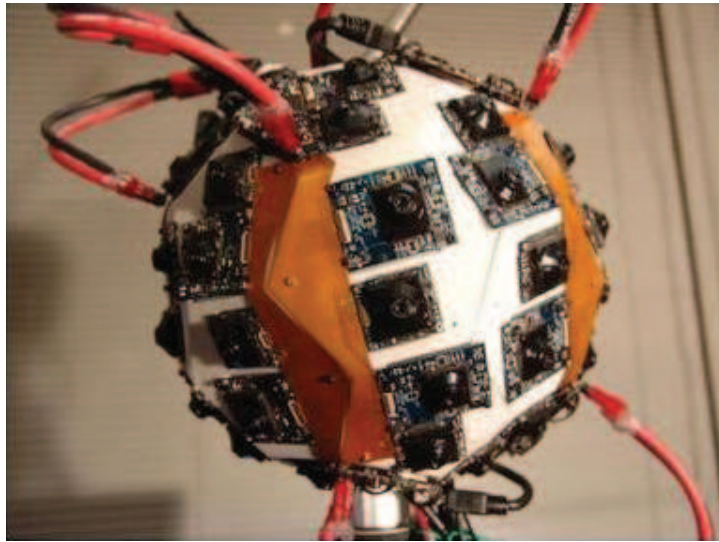
Figure 7.2: Centeye, Inc^{TM}MAOS; will deliver optic flow measurements over the entire sphere

Appendix A

Derivations

A.1 WFI Simplification using Linearized Optic Flow Model

Theorem

Let $f(\gamma, \beta)$ and $g(\gamma, \beta, \mathbf{x})$ be functions residing in $L^2(S^2, \mathbb{R}^2)$. Define the operation

$$y(\mathbf{x}) = \int_{a(\mathbf{x})}^{b(\mathbf{x})} \int_{c(\mathbf{x})}^{d(\mathbf{x})} g(\gamma, \beta, \mathbf{x}) \, f(\gamma, \beta) \sin \beta \; d\beta \; d\gamma$$

and the linearization of $y(\mathbf{x})$ about $\mathbf{x} = \mathbf{x}_0$ as $z(\mathbf{x}) = y(\mathbf{x}_0) + \sum_i \frac{\partial y}{\partial x_i}(\mathbf{x}_0) \, (x_i - x_{i0})$. Then $z(\mathbf{x})$ can be computed by

$$z(\mathbf{x}) = y(\mathbf{x}_0) + \sum_i (x_i - x_{i0}) \int_{a(\mathbf{x}_0)}^{b(\mathbf{x}_0)} \int_{c(\mathbf{x}_0)}^{d(\mathbf{x}_0)} \frac{\partial g(\gamma, \beta, \mathbf{x})}{\partial x_i}(\mathbf{x}_0) \, f(\gamma, \beta) \sin \beta \; d\beta \; d\gamma.$$

Proof

$$
\begin{aligned}
z(\mathbf{x}) &= y(\mathbf{x}_0) + \sum_i (x_i - x_{i0}) \frac{\partial \int_{a(\mathbf{x})}^{b(\mathbf{x})} \int_{c(\mathbf{x})}^{d(\mathbf{x})} g(\gamma, \beta, \mathbf{x})\, f(\gamma, \beta) \sin \beta\, d\beta\, d\gamma}{\partial x_i} \bigg|_{\mathbf{x} = \mathbf{x}_0} \\
&= y(\mathbf{x}_0) + \sum_i (x_i - x_{i0}) \int_{a(\mathbf{x})}^{b(\mathbf{x})} \int_{c(\mathbf{x})}^{d(\mathbf{x})} \left(\frac{\partial g(\gamma, \beta, \mathbf{x})}{\partial x_i}\, f(\gamma, \beta) \right. \\
&\quad \left. + g(\gamma, \beta, \mathbf{x}) \frac{\partial f(\gamma, \beta)}{\partial x_i} \right) \sin \beta\, d\beta\, d\gamma \bigg|_{\mathbf{x} = \mathbf{x}_0} \\
&= y(\mathbf{x}_0) + \sum_i (x_i - x_{i0}) \int_{a(\mathbf{x}_0)}^{b(\mathbf{x}_0)} \int_{c(\mathbf{x}_0)}^{d(\mathbf{x}_0)} \frac{\partial g(\gamma, \beta, \mathbf{x})}{\partial x_i}(\mathbf{x}_0)\, f(\gamma, \beta) \sin \beta\, d\beta\, d\gamma.
\end{aligned}
$$

A.2 Flat-Camera to Sphere Mapping

The spherical grid points are mapped to individual camera pixels by the following method; note that a pin-hole camera model has been assumed.

1. For each camera, compute the direction cosine matrix $\mathcal{R}_{\mathcal{CB}}$ that brings body-frame vectors into the local camera frame. We define the camera frame with the x-axis pointing image-right and y pointing image-up, which leads to

$$
\mathcal{R}_{\mathcal{CB}} = \mathcal{R}^1\left(-\frac{\pi}{2}\right) \mathcal{R}^3\left(\frac{\pi}{2}\right) \mathcal{R}^1(\phi_c)\mathcal{R}^2(\theta_c)\mathcal{R}^3(\psi_c). \tag{A.1}
$$

$\mathcal{R}^i$ refers to a Euler rotation matrix about axis i, and the camera yaw (ψ_c), pitch (θ_c) and roll (ϕ_c) are the 3-2-1 Euler rotations relative to a zero-roll camera pointing along the body x_b-axis.

2. Define a measurement grid of spherical coordinates that covers the desired swath to be used in the WFI. For each grid point, define its projection point

on the unit sphere in terms of Cartesian coordinates;

$$[\hat{\mathbf{e}}_r]_{\mathcal{B}} = \begin{pmatrix} x_b \\ y_b \\ z_b \end{pmatrix} = \begin{pmatrix} \cos\gamma\sin\beta \\ \sin\gamma\sin\beta \\ \cos\beta \end{pmatrix}. \tag{A.2}$$

3. For each camera, compute the camera-frame x_c, y_c coordinate limits of the viewable region boundaries - defined by the horizontal and vertical field of views (α_H and α_V respectively). The camera is modeled as a flat rectangular surface situated such that its center-point touches the unit sphere (Fig. A.1).

$$x_{c,max} = \tan^{-1}(\alpha_H/2) \tag{A.3}$$
$$y_{c,max} = \tan^{-1}(\alpha_V/2).$$

4. For each camera, cycle through all grid points and compute the corresponding camera frame coordinates by shifting the body-frame vector into the camera frame. The body-frame vector length r must be recomputed for every possible camera and grid point combination as it is the distance along the relevent spherical coordinate vector to the geometric projection point on the applicable camera surface.

$$[\mathbf{r}]_{\mathcal{C}} = \mathcal{R}_{\mathcal{CB}}\,[\hat{\mathbf{e}}_r]_{\mathcal{B}}\,r. \tag{A.4}$$

Since the camera surface is assumed to be touching the unit sphere only at its center, the z_c coordinate (axis orthogonal to the camera plane) of a point on the camera surface will always be -1. We can use this to solve the z_c expression
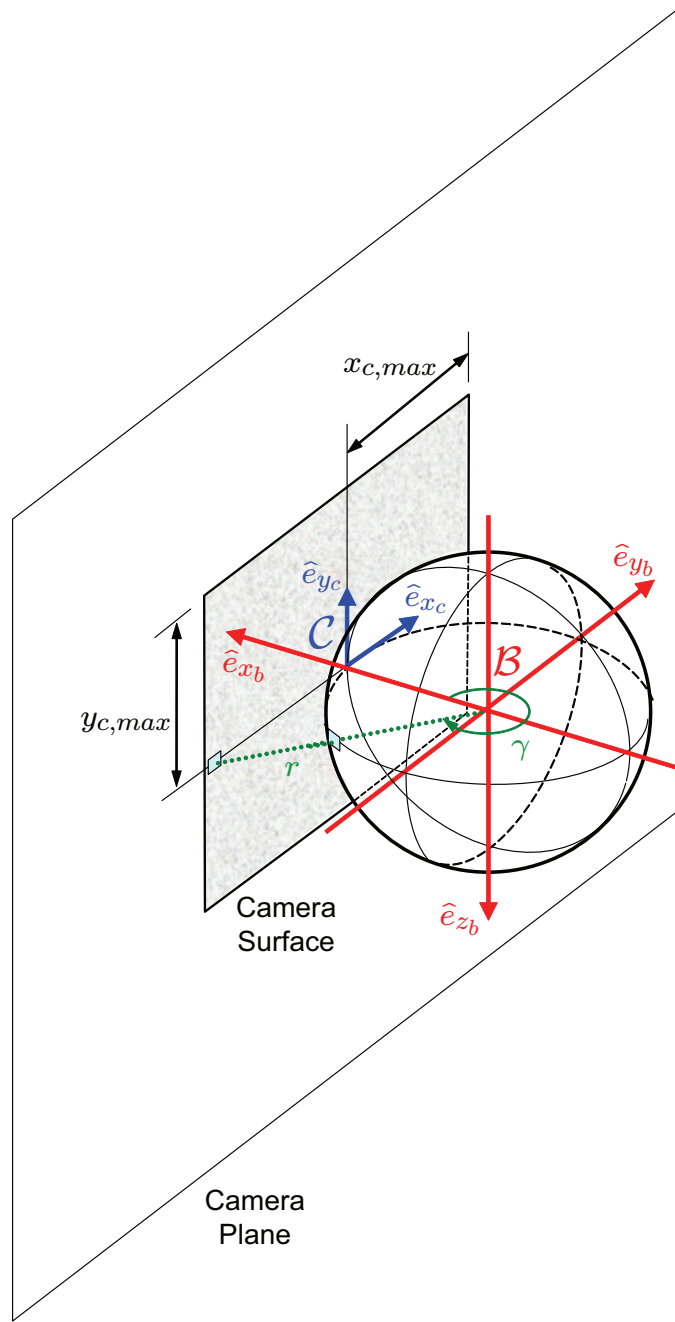
Figure A.1: Projection of spherical coordinate grid on to flat imaging surface. Shown is an equatorial measurement node projected from the unit sphere to the camera surface along vector **r**. The surface boundaries are defined by the horizontal and vertical field of views.

from (A.4) for r, in order to make the general (A.4) equation deterministic.

$$r = \frac{1}{\cos\theta_c \sin\beta \cos(\psi_c - \gamma) - \sin\theta_c \cos\beta}. \qquad (A.5)$$

5. If the camera-frame coordinates for the grid point fall within the viewable region of the camera (i.e. $|x_c| < x_{c,max}$, $|y_c| < y_{c,max}$, $r > 0$), then compute the specific pixel coordinates and assign the grid point to be measured using that camera:

$$\text{PIXELCOLUMN} = \left(\frac{x_c}{x_{c,max}} + 1\right)\frac{\text{IMAGEWIDTH}}{2} \qquad (A.6)$$
$$\text{PIXELROW} = \left(\frac{y_c}{y_{c,max}} + 1\right)\frac{\text{IMAGEHEIGHT}}{2}.$$

The camera-frame Cartesian optic flow estimates are mapped to the local spherical frame $\mathcal{L} = \{\hat{\mathbf{e}}_r, \hat{\mathbf{e}}_\beta, \hat{\mathbf{e}}_\gamma\}$ by the following method:

$$\begin{pmatrix} \dot{Q}^r \\ \dot{Q}^\beta \\ \dot{Q}^\gamma \end{pmatrix} = \mathcal{R}_{\mathcal{L}\mathcal{B}}\mathcal{R}_{\mathcal{C}\mathcal{B}}^T \begin{pmatrix} \Delta x_c \\ \Delta y_c \\ 0 \end{pmatrix} \frac{x_{c,max}}{r} \frac{2 \text{ FPS}}{\text{IMAGEWIDTH}} \qquad (A.7)$$

$$\mathcal{R}_{\mathcal{L}\mathcal{B}} = \begin{pmatrix} s\beta c\gamma & s\beta s\gamma & c\beta \\ c\beta c\gamma & c\beta s\gamma & -s\beta \\ -s\gamma & c\gamma & 0 \end{pmatrix}. \qquad (A.8)$$

assuming small shifts $(\Delta x_c, \Delta y_c)$ between frames. The $1/r$ quantity converts linear shift to angular units and compensates for the fact that the same rotation motion will cause greater image shifts near the camera edges than at the center. Note that radial flow $\dot{Q}_r$ is ignored as it is merely a numerical artifact from the use of a flat imaging device.

A.3 WFI Computation for Different Measurement Grids

To ensure accurate discretization of the continuous integral over the measurement domain, the chosen grid node spacing must be accompanied with appropriate weightings of nodes in the summation.

- If grid points have equal angular spacing ($\Delta\gamma = \Delta\beta$) then

$$y_j = \Delta\gamma\Delta\beta \sum_{k=1}^{\mathcal{K}} \left(\dot{Q}^\gamma(\gamma_k, \beta_k) \, F_{y_j}^\gamma(\gamma_k, \beta_k) + \dot{Q}^\beta(\gamma_k, \beta_k) \, F_{y_j}^\beta(\gamma_k, \beta_k) \right) \sin\beta. \quad \text{(A.9)}$$

- If grid points cover (approximately) equal solid angles ($\Delta\Omega \approx$ constant), as in the case of sub-divided icosahedral grid, then

$$y_j = \Delta\Omega \sum_{k=1}^{\mathcal{K}} \left(\dot{Q}^\gamma(\gamma_k, \beta_k) \, F_{y_j}^\gamma(\gamma_k, \beta_k) + \dot{Q}^\beta(\gamma_k, \beta_k) \, F_{y_j}^\beta(\gamma_k, \beta_k) \right). \quad \text{(A.10)}$$

- If grid points not consistently spaced, then select an orthonormal basis for $L^2(S^2, \mathbb{R})$ and define matrix G whose entries $G_{kf} = F_f(\gamma_k, \beta_k)$ correspond to element f from the basis (e.g. spherical harmonic f). Considering the azimuthal direction, define vector $\mathcal{V}^\gamma$ with entries $\mathcal{V}_k^\gamma = F_{y_j}(\gamma_k, \beta_k)$ and $\mathcal{X}^\gamma$ with entries $\mathcal{X}_k^\gamma = \dot{Q}^\gamma(\gamma_k, \beta_k)$. Since both the weighting pattern and optic flow can be approximated as a summation of elements from the orthonormal basis ($\mathcal{V}_k^\gamma = G\mathcal{Y}^\gamma$ and $\mathcal{X}_k^\gamma = G\mathcal{Z}^\gamma$), the WFI inner product can be constructed as the summation of the inner products between basis elements. To achieve a good approximations, include spherical harmonics up to $\sim$10th order. Least squares inversion is used to solve for the basis coefficients $\mathcal{Y}^\gamma$ and $\mathcal{Z}^\gamma$, and the

inner product is extended to include both dimensions:

$$
\begin{aligned}
y_j &= (\mathcal{Y}^\gamma)^T \mathcal{Z}^\gamma + (\mathcal{Y}^\beta)^T \mathcal{Z}^\beta \tag{A.11}\\
&= (\mathcal{V}^\gamma)^T G (G^T G)^{-T} (G^T G)^{-1} G^T \mathcal{X}^\gamma + (\mathcal{V}^\beta)^T G (G^T G)^{-T} (G^T G)^{-1} G^T \mathcal{X}^\beta.
\end{aligned}
$$

Bibliography

[1] H. G. Krapp, R. Hengstenberg, and M. Egelhaaf. Binocular contributions to optic flow processing in the fly visual system. *Journal of Neurophysiology*, 85:724–734, 2001.

[2] H. G. Krapp, B. Hengstenberg, and R. Hengstenberg. Dendritic structure and receptive-field organization of optic flow processing interneurons in the fly. *Journal of Neurophysiology*, 79(4):1902–1917, 1998.

[3] G.K. Taylor and H.G. Krapp. Sensory systems and flight stability: What do insects measure and why? *Advanced Insect Physiology*, 34:231–316, 2008.

[4] R. J. Wood, E. Steltz, and R. S. Fearing. Nonlinear performance limits for high energy density piezoelectric bending actuators. In *International Conference on Robotics and Automation*. Barcelona, Spain, 2005.

[5] A. M. Hoover and R. S. Fearing. Fast scale prototyping for folded millirobots. In *Robotics and Automation, 2008. ICRA 2008. IEEE International Conference on*, pages 886–892, May 2008.

[6] R. J. Wood, S. Avadhanula, R. Sahai, E. Steltz, and R. S. Fearing. Microrobot design using fiber reinforced composites. *ASME Journal of Mechanical Design*, 130(5), 2008.

[7] R. J. Wood, S. Avadhanula, R. Sahai, E. Steltz, and R. S. Fearing. First takeoff of a biologially-inspired at-scale robotic insect. *IEEE Trans. on Robotics*, 24(2):341–347, 2008.

[8] Aerius data sheet. *[online]*, http://www.procerusuav.com/Downloads/DataSheets/ AeriusMiniatureLaserRangefinder.pdf, Accessed 7/20/09.

[9] O. Amidi, Y. Mesaki, and T. Kanade. A visual odometer for autonomous helicopter flight. *Robotics & Autonomous Systems*, August 1999.

[10] P. Gurfil and H. Rotstein. Partial aircraft state estimation from visual motion using the subspace constraints approach. *Journal of Guidance, Control, and Dynamics*, 24(5):1016–1028, 2001.

[11] S. Hrabar and G. S. Sukhatme. Omnidirectional vision for an autonomous helicopter. In *In IEEE International Conference on Robotics and Automation*, pages 558–563, 2003.

[12] M. Garratt and J. Chahl. Visual control of an autonomous helicopter. In *Proceedings of the 41st Aerospace Sciences Meeting and Exhibit*. AIAA 2003-460, Reno, NV, 2003.

[13] P. J. Garcia-Pardo, G. S. Sukhatme, and J. F. Montgomery. Towards vision-based safe landing for an autonomous helicopter. *Robotics and Autonomous Systems*, 38(1):19 – 29, 2002.

[14] J. Li and R. Chellappa. A factorization method for structure from planar motion. *IEEE Workshop on Motion and Video Computing*, 2:154–159, January 2005.

[15] B. K. P. Horn. *Robot Vision*. MIT Press and McGraw-Hill, Cambridge, MA, 1986.

[16] E. R. Davies. *Machine Vision: Theory, Algorithms, Practicalities*. Morgan Kaufmann, San Francisco, CA, 2005.

[17] F. Kendoula, I. Fantoni, and K. Nonamib. Optic flow-based vision system for autonomous 3d localization and control of small aerial vehicles. *Robotics and Autonomous Systems (in press)*, 2010.

[18] R. Beard, D. Kingston, M. Quigley, D. Snyder, R. Christainsen, W. Johnson, T. McLain, and MA Goodrich. Autonomous vehicle technologies for small fixed-wing uavs. *Journal of Aerospace Computing, Information, and Communication*, 2:92–108, 2005.

[19] J. M. Grasmeyer and M. T. Keennon. Development of the black widow micro air vehicle. In *Proceedings of the 39th AIAA Aerospace Sciences Meeting and Exhibit*. 2001.

[20] M. A. Frye and M. H. Dickinson. Fly flight: A model for the neural control of complex behavior. *Neuron*, 32(3):385–388, 2001.

[21] M. Egelhaaf, R. Kern, H. Krapp, J. Kretzberg, R. Kurtz, and A. Warzecha. Neural encoding of behaviourally relevant visual-motion information in the fly. *Trends in Neurosciences*, 25(2):96–102, 2002.

[22] A. Borst and J. Haag. Neural networks in the cockpit of the fly. *Journal of Comparative Physiology A*, 188(6):419–437, 2002.

[23] J. J. Gibson. *The perception of the visual world*. Houghton Mifflin, Boston, 1950.

[24] C. T. David. Compensation for height in the control of groundspeed by *Drosophila* in a new, barber's pole wind tunnel. *Journal of Comparative Physiology*, 147(4):485–493, 1982.

[25] L. F. Tammero and M. H. Dickinson. The influence of visual landscape on the free flight behavior of the fruit fly *Drosophila Melanogaster*. *Journal of Experimental Biology*, 205:327–343, 2002.

[26] M. V. Srinivasan, S. W. Zhang, M. Lehrer, and T. S. Collett. Honeybee navigation *en route* to the goal: Visual flight control and odometry. *Journal of Experimental Biology*, 199(1):237–244, 1996.

[27] M. V. Srinivasan and S. W. Zhang. Visual motor computations in insects. *Annual Review if Neuroscience*, 27:679–696, 2004.

[28] J. J. Koenderink and A. J. van Doorn. Facts on optic flow. *Biol. Cybern.*, 56(4):247–254, 1987.

[29] N. Franceschini, A. Riehle, and A. Le Nestour. Directionally selective motion detection by insect neurons. In DG Stavenga and RC Hardie, editors, *Facets of Vision*, pages 360–390. Springer-Verlag, Berlin, 1989.

[30] M. Egelhaaf and A. Borst. Motion computation and visual orientation in flies. *Journal of Comparative Biochemistry Phisiology*, 104(4):659–673, 1993.

[31] K. Hausen. Motion sensitive interneurons in the optomotor system of the fly, part i. the horizontal cells: Structure and signals. *Biological Cybernetics*, 45:143–156, 1982.

[32] K. Hausen. Motion sensitive interneurons in the optomotor system of the fly, part ii. the horizontal cells: Receptive field organization and response characteristics. *Biological Cybernetics*, 46(1):67–79, 1982.

[33] R. Hengstenberg, K. Hausen, and B. Hengstenberg. The number and structure of giant vertical cells (vs) in the lobula plate of the blowfly *Calliphora Erythrocephala*. *Journal of Comparative Physiology*, 149(2):163–177, 1982.

[34] H. G. Krapp and R. Hengstenberg. Estimation of self-motion by optic flow processing in single visual interneurons. *Letters to Nature*, 384:463–466, 1996.

[35] M. O. Franz and H. G. Krapp. Wide-field, motion-sensitive neurons and matched filters for optic flow fields. *Biological Cybernetics*, 83:185–197, 2000.

[36] K. Karmeier, J. H. van Hateren, R. Kern, and M. Egelhaaf. Encoding of naturalistic optic flow by a population of blowfly motion-sensitive neurons. *Journal of Neurophysiology*, 96:1602–1614, 2006.

[37] S. Hrabar, G. S. Sukhatme, P. Corke, K. Usher, and J. Roberts. Combined optic-flow and stereo-based navigation of urban canyons for a uav. In *Proceedings of the IEEE International Conference on Intelligent Robots and Systems*. Edmonton, Canada, 2005.

[38] A. Beyeler, J.-C. Zufferey, and D. Floreano. 3d vision-based navigation for indoor microflyers. In *Proceedings of the IEEE International Conference on Robotics and Automation*. Roma, 2007.

[39] S. Griffiths, J. Saunders, A. Curtis, T. McLain, and R. Beard. *Obstacle and Terrain Avoidance for Miniature Aerial Vehicles (in Book: Advances in Unmanned Aerial Vehicles)*, volume 33. Springer Netherlands, 2007.

[40] M. O. Franz and H. A. Mallot. Biomimetic robot navigation. *Robotics and Autonomous Systems*, 30:133–153, 2000.

[41] J. Santos-Victor and G. Sandini. Embedded visual behaviors for navigation. *Robotics and Autonomous Systems*, 19:299–313, 1997.

[42] D. Coombs, M. Herman, T. H. Hong, and M. Nashman. Real-time obstacle avoidance using central flow divergence, and peripheral flow. *IEEE Transactions on Robotics and Automation*, 14:49–59, 1998.

[43] N. Franceschini, J. M. Pichon, and C. Blanes. From insect vision to robot vision. *Phil. Trans. R. Soc. Lond. B*, 337:283–294, 1992.

[44] L. Muratet, S. Doncieux, Y. Briere, and J. Meyer. A contribution to vision-based autonomous helicopter flight in urban environments. *Robotics and Autonomous Systems*, 50(4):195–209, 2005.

[45] J. Serres, D. Dray, F. Ruffier, and N. Franceschini. A vision-based autopilot for a miniature air vehicle: joint speed control and lateral obstacle avoidance. *Autonomous Robots*, 25:103–122, 2008.

[46] J. P. Lindemann, H. Weiss, R. Moeller, and M. Egelhaaf. Saccadic flight strategy facilitates collision avoidance: closed-loop performance of a cyberfly. *Biological Cybernetics*, 98:213–227, 2008.

[47] J. Santos-Victor, G. Sandini, F. Curroto, and S. Garibaldi. Divergent stereo in autonomous navigation - from bees to robots. *International Journal of Computer Vision*, 14:159–177, 1995.

[48] K. Weber, S. Venkatesh, and M. V. Srinivasan. Robot navigation inspired by principles of insect vision. *Robotics and Autonomous Systems*, 26:203–216, 1999.

[49] A. Argyros, D. Tsakiris, and C. Groyer. Biomimetic centering behavior for mobile robots with panoramic sensors. *IEEE Robotics and Automation Magazine*, pages 21–30, December 2004.

[50] J. Serres, F. Ruffier, and N. Franceschini. Two optic flow regulators for speed control and obstacle avoidance. In *Proceedings of the IEEE International Conference on Medical Robotics and Biomechatronics*. Pisa, Italy, February, 2005.

[51] J. S. Chahl and M. V. Srinivasan. A complete panoramic vision system, incorporating imaging, ranging, and three dimensional navigation. In *Proceedings of the IEEE Workshop on Omnidirectional Vision*, pages 104–111. IEEE, Hilton Head, SC, 2000.

[52] N. Franceschini, F. Ruffier, and J. Serres. A bio-inspired flying robot sheds light on insect piloting abilities. *Current Biology*, 17(4):329–335, 2007.

[53] A. Beyeler, J.-C. Zufferey, and D. Floreano. *Optic-Flow to Steer and Avoid Collisions in 3D (in Book: Flying Insects and Robotics)*. Springer-Verlag, Berlin, 2009.

[54] A. X. Miao, G. L. Zacharias, and R. Warren. Passive navigation from image sequences - a practitioner's approach. In *Proceedings of the AIAA Flight Simulation Technologies Conference*. AIAA-1996-3556, San Diego, CA, 1996.

[55] J. J. Kehoe, A. S. Watkins, R. S. Causey, and R. Lind. State estimation using optical flow from parallax-weighted feature tracking. In *Proceedings of the AIAA Guidance, Navigation, and Control Conference and Exhibit*. AIAA-2006-6721, Keystone, CO, 2006.

[56] A. R. Bruss and K. P. Horn. Passive navigation. *Computer Vision, Graphics, and Image Processing*, 21(1):3–20, 1983.

[57] M. O. Franz, J. S. Chahl, and H. G. Krapp. Insect-inspired estimation of egomotion. *Neural Computation*, 16(11):2245–2260, 2004.

[58] S. Srinivasan. Extracting structure from optical flow using the fast error search technique. *International Journal of Computer Vision*, 37(3):203–230, 2000.

[59] C. Braillon, C. Pradalier, J. L. Crowley, and C. Laugier. Real-time moving obstacle detection using optical flow models. In *Proceedings of the Intelligent Vehicles Symposium*. Tokyo, Japan, 2006.

[60] O. Toupet, J. D. Paduano, R. Panish, R. Sedwick, and E. Frazzoli. Augmenting state estimates with multiple camera visual measurements. In *Proceedings of the AIAA Infotech@Aerospace Conference and Exhibit*. AIAA-2007-2983, Rohnert Park, CA, 2007.

[61] B. Call, R. Beard, and C. Taylor. Obstacle avoidance for unmanned vehicles using image feature tracking. In *Proceedings of the AIAA Guidance, Navigation, and Control Conference*. AIAA-2006-6541, Keystone, CO, 2006.

[62] T. P. Webb, R. J. Prazenica, A. J. Kurdila, and R. Lind. Vision-based state estimation for autonomous micro air vehicles. *Journal of Guidance, Control, and Dynamics*, 30(3):816–826, 2007.

[63] A. J. Grunwald. Stability and control of a remotely controlled indoors micro hovering vehicle. In *Proceedings of the AIAA Guidance, Navigation, and Control Conference and Exhibit*. AIAA-2005-6283, San Francisco, CA, 2005.

[64] G. Qian, R. Chellappa, and Q. Zheng. Robust structure from motion estimation using inertial data. *Journal of the Optical Society of America A*, 18(12):2982–2997, 2001.

[65] J. S. Humbert, R. M. Murray, and M. H. Dickinson. Sensorimotor convergence in visual navigation and flight control systems. In *Proceedings of the 16th IFAC World Congress*, volume 16. Praha, Czech Republic, 2005.

[66] J. S. Humbert, R. M. Murray, and M. H. Dickinson. Pitch-altitude control and terrain following based on bio-inspired visuomotor convergence. In *Proceedings of the AIAA Guidance, Navigation and Control Conference*. AIAA-2005-6280, San Francisco, CA, 2005.

[67] J. S. Humbert, R. M. Murray, and M. H. Dickinson. A control-oriented analysis of bio-inspired visuomotor convergence. In *Proceedings of the 44th IEEE Conference on Decision and Control*. Seville, Spain, 2005.

[68] J. S. Humbert and A. M. Hyslop. Bio-inspired visuomotor convergence. *IEEE Transactions on Robotics (in press)*, 2010.

[69] M. V. Srinivasan, S. Zhang, and J. S. Chahl. Landing strategies in honeybees, and possible applications to autonomous airborne vehicles. *Biological Bulletin*, 200:216–221, 2001.

[70] P. Xu, J. S. Humbert, and P. Abshire. Implementation and demonstration of wide-field integration in analog vlsi. *Submitted to Biological Cybernetics*, 2009.

[71] B. L. Stevens and F. L. Lewis. *Aircraft Control and Simulation*. John Wiley & Sons, Hoboken, NJ, 2003.

[72] S. Owen. *Stochastic properties of wide field integrated optic flow measurements*. Masters Thesis, University of Maryland, College Park, MD 20742, 2009.

[73] A. K. Roy-Chowdhury and R. Chellappa. Statistical bias in 3-d reconstruction from a monocular video. *IEEE Transactions on Image Processing*, 14(8):1057–1062, 2005.

[74] H. Kwakernaak and R. Sivan. *Linear Optimal Control Systems, First Edition*. Wiley-Interscience, New York, 1972.

[75] J. K. Conroy, G. Gremillion, B. Ranganathan, and J. S. Humbert. Implementation of wide-field integration methods for autonomous micro helicopter navigation. *Autonomous Robots*, 27(3):189–198, 2009.

[76] J. S. Humbert, A. Hyslop, and M. Chinn. Experimental validation of wide-field integration methods for autonomous navigation. In *Proceedings of IEEE/RSJ International Conference on Intelligent Robots and Systems*. San Diego, CA, 2007.

[77] J. Y. Bouguet. Pyramidal implementation of the lucas kanade feature tracker. In *URL: http://www.intel.com/research/mrl/research/opencv/*. Intel Corporation, Microprocessor Research Labs, 1981.

[78] M. Drela. Crrcsim - model-airplane flight simulation program. URL: http://crrcsim.sourceforge.net/wiki, 2007.

[79] J. K. Conroy, J. S. Humbert, and D. Pines. System identification of a rotary-wing micro air vehicle. *Journal of the American Helicopter Society (in press)*, 2010.

[80] H. Cuntz, J. Haag, F. Forstner, I. Segev, and A. Borst. Robust coding of flow-field parameters by axo-axonal gap junctions between fly visual interneurons. *Proceedings of the National Academy of Sciences of the USA*, 104:1022910233, 2007.

[81] R. Baraniuk. A lecture on compressive sensing. *IEEE Signal Processing Magazine*, 2007.

[82] I. Faruque and J. S. Humbert. Dipteran insect flight dynamics: Part 1: Longitudinal motions about hover. *Journal of Theoretical Biology (in press)*, 2010.

[83] I. Faruque and J. S. Humbert. Dipteran insect flight dynamics: Part 1: Lateral-directional motion about hover. *Journal of Theoretical Biology (under review)*, 2010.

[84] H. Chao, Y. Cao, and Y.Q. Chen. Autopilots for small fixed-wing unmanned air vehicles: A survey. In *Proceedings of the IEEE International Conference on Mechatronics and Automation*. Harbin, China, 2007.

[85] S. Hrabar and G. S. Sukhatme. A comparison of two camera configurations for optic-flow based navigation of a uav through urban canyons. In *Proceedings of the IEEE International Conference on Intelligent Robots and Systems*. Sendai, Japan, 2004.

[86] G. N. DeSouza and A. C. Kak. Vision for mobile robot navigation: A survey. *IEEE Transactions on Pattern Analysis and Machine Intelligence*, 24(2):237–266, 2002.

[87] J. C. Zufferey and D. Floreano. Fly-inspired visual steering of an ultralight indoor aircraft. *IEEE Transactions on Robotics*, 22(1):137–146, 2006.

[88] R. Z. Shi and T. K. Horiuchi. A neuromorphic vlsi model of bat interaural level difference processing for azimuthal echolocation. *IEEE Transactions on Circuits and Systems I*, 54(1):74–88, 2007.

[89] M. Egelhaaf. On the neuronal basis of figure-ground discrimination by relative motion in the visual system of the fly. ii. figure detection cells, a new class of visual interneurones. *Biological Cybernetics*, 52:195–209, 1985.

[90] L. Muratet, S. Doncieux, and J.-A. Meyer. A biomimetic reactive navigation system using the optical flow for a rotary-wing uav in urban environment. In *Proceedings of the 35th International Symposium of Robotics*. Paris, 2004.

[91] A. Beyeler, J.-C. Zufferey, and D. Floreano. Wide vision-based control of near-obstacle flight. *Autonomous Robots*, 27(3), 2009.

[92] B. Rasnow. The effects of simple objects on the electric field of apteronotus. *Journal of Comparative Physiology A*, 178(3):397–411, 1996.

[93] J.M. Camhi. Locust wind receptors i. transducer mechanics and sensory response. *Journal of Experimental Biology*, 50:335–348, 1969.

[94] S. J. Huston and H. G. Krapp. Visuomotor transformation in the fly gaze stabilization system. *PLoS Biology*, 6(7):1468–1478, 1985.